ANNALS OF THE UNIVERSITY OF CRAIOVA
ANNALES DE L’UNIVERSITÉ DE CRAIOVA

ANALELE UNIVERSITĂȚII DIN CRAIOVA

SERIA: INGINERIE ELECTRICĂ
SERIE: ELECTRICAL ENGINEERING
SÉRIE: INGÉNIERIE ÉLECTRIQUE

Anul/Year/Année 49
No. 49, Vol. 49, Issue 1, 2025

December 2025

ISSN 1842-4805 (print)
ISSN 2971-9852 (online)
ISSN-L 1842-4805

EDITURA UNIVERSITARIA

ANNALS OF THE UNIVERSITY OF CRAIOVA

13, A.I. Cuza Str., CRAIOVA 200585
ROMANIA

We exchange publications
with similar institutions of country and from abroad

ANNALES DE L'UNIVERSITÉ DE CRAIOVA

Rue A.I. Cuza, No. 13, CRAIOVA 200585
ROUMANIE

On fait des échanges des publications
avec les institutions similaires du pays et de l'étranger

This journal is published by the Faculty of Electrical Engineering from the University of Craiova.
The authors are fully responsible for the originality of their papers and for accuracy of their notes.

Editorial board

Conf.dr.ing. Mircea DRIGHICIU – editor in chief, University of Craiova, Romania
Ș.l.dr.ing. Ioana Gabriela SÎRBU – editor in chief, University of Craiova, Romania
Prof.dr.ing. Ioan POPA, University of Craiova, Romania
Prof.dr.ing. Dan MIHAI, University of Craiova, Romania
Prof.dr.ing. Marian CIONTU, University of Craiova, Romania
Prof.dr.ing. Lucian MANDACHE, University of Craiova, Romania
Prof.dr.sc. Ivan YATCHEV, Technical University of Sofia, Bulgaria
Prof.dr.ing. Leszek CZARNECKI, Life Fellow IEEE, Louisiana State University, USA
Prof.dr.ing. Slavoljub ALEKSIC, University of Niš, Serbia
Prof.dr.ing. Mihai IORDACHE, University “Politehnica” of Bucharest, Romania
Prof.dr.ing. Victor ŞONTEA, Technical University of Moldova, Moldova
Prof.dr.ing. Iuliu DELEŞEGA, University “Politehnica” of Timişoara, Romania
Prof.dr.ing. Dumitru-Marcel ISTRATE, "Gh. Asachi" Technical University of Iaşi, Romania
Prof.dr.ing. Miroslav PRSA, University of Novi Sad, Serbia
Prof.dr.ing. Maria BROJBOIU, University of Craiova, Romania
Prof.dr.ing. Mihai GAVRILAŞ, "Gh. Asachi" Technical University of Iaşi, Romania
Prof.dr.ing. Daniela DANCIU, University of Craiova, Romania
Prof.dr.ing. Nicolae MUNTEAN, University “Politehnica” of Timişoara, Romania
Prof.dr.ing. Călin MUNTEANU, Technical University of Cluj-Napoca, Romania
Prof.dr.ing. Leonardo-Geo MĂNESCU, University of Craiova, Romania
Prof.dr.ing. Camelia PETRESCU, "Gh. Asachi" Technical University of Iaşi, Romania
Conf.dr.ing. Cristian Daniel CISMARU, University of Craiova, Romania
Ș.l.dr.ing. Alin Iulian DOLAN, University of Craiova, Romania

REVIEWERS COMMITTEE

Lia-Elena ACIU – *Transilvania University of Braşov,* Romania
Maricel ADAM – *"Gh. Asachi" Technical University of Iaşi,* Romania
Mihaela ALBU – *University “Politehnica” of Bucharest,* Romania
Slavoljub ALEKSIC – *University of Niš,* Serbia
Horia BĂLAN – *Technical University of Cluj-Napoca,* Romania
Alexandru BITOLEANU – *University of Craiova, Romania*
Maria BROJBOIU – *University of Craiova,* Romania
Emil CAZACU – *University “Politehnica” of Bucharest,* Romania
Aurel CÂMPEANU – *University of Craiova,* Romania
Mihai CERNAT – *Transilvania University of Braşov,* Romania
Marian CIONTU – *University of Craiova,* Romania
Daniel Cristian CISMARU – *University of Craiova,* Romania
Grigore CIVIDJIAN – *University of Craiova,* Romania
Zlata CVETCOVIC – *University of Niš,* Serbia
Leszek CZARNECKI – *Louisiana State University*, USA
Cristinel Radu DACHE – *"Dunărea de Jos" University of Galați,* Romania
Daniela DANCIU – *University of Craiova,* Romania
Sonia DEGERATU – *University of Craiova,* Romania
Iuliu DELEŞEGA – *University “Politehnica” of Timişoara,* Romania
Silvia-Maria DIGĂ – *University of Craiova,* Romania
Peter DINEFF – *Technical University of Sofia,* Bulgaria
Radu DOBRESCU – *University “Politehnica” of Bucharest,* Romania
Alin Iulian DOLAN – *University of Craiova,* Romania
Mircea-Adrian DRIGHICIU – *University of Craiova,* Romania
Laurentiu Marius DUMITRAN – *University “Politehnica” of Bucharest,* Romania
Sorin ENACHE – *University of Craiova,* Romania
Virgiliu FIRETEANU – *University “Politehnica” of Bucharest,* Romania
Dan FLORICĂU – *University “Politehnica” of Bucharest,* Romania
Cristian FOŞALĂU – *"Gh. Asachi" Technical University of Iaşi*, Romania
Teodor Lucian GRIGORIE – *Military Technical Academy "Ferdinand I",* Romania
Stefan HĂRĂGUŞ – *University “Politehnica” of Timişoara,* Romania
Elena HELEREA – *Transilvania University of Braşov,* Romania
Eugen HNATIUC – *"Gh. Asachi" Technical University of Iaşi,* Romania
Kemal HOT – *Polytechnic of Zagreb,* Croatia
Eugen IANCU – *University of Craiova,* Romania
Nathan IDA – *University of Akron,* USA
Maria IOANNIDES – *National Technical University of Athens,* Greece
Valentin IONIŢĂ – *University “Politehnica” of Bucharest,* Romania
Mihai IORDACHE – *University “Politehnica” of Bucharest,* Romania
Marcel ISTRATE – *"Gh. Asachi" Technical University of Iaşi*, Romania
Wilhelm KAPPEL – *National Research and Development Institute for Electrical Engineering (ICPE – CA) Bucharest,* Romania
Liviu KREINDLER – *University “Politehnica” of Bucharest,* Romania
Gheorghe LIVINŢ – *"Gh. Asachi" Technical University of Iaşi*, Romania
Dumitru Dorin LUCACHE – *"Gh. Asachi" Technical University of Iaşi*, Romania
Lucian MANDACHE – *University of Craiova,* Romania
Gheorghe MANOLEA – *University of Craiova,* Romania
Andrei MARINESCU – *Romanian Academy of Technical Science, Craiova Branch,* Romania
Iliana MARINOVA – *Technical University of Sofia,* Bulgaria

Claudia MARTIŞ – *Technical University of Cluj-Napoca,* Romania
Ernest MATAGNE – *Université Catholique de Louvain,* Belgium
Leonardo-Geo MĂNESCU – *University of Craiova,* Romania
Dan MIHAI – *University of Craiova,* Romania
Alexandru MOREGA – *University “Politehnica” of Bucharest,* Romania
Mihaela MOREGA – *University “Politehnica” of Bucharest,* Romania
Nazih MOUBAYED – *Lebanese University,* Lebanon
Călin MUNTEANU – *Technical University of Cluj-Napoca,* Romania
Florin MUNTEANU – *"Gh. Asachi" Technical University of Iaşi,* Romania
Valentin NĂVRĂPESCU – *University “Politehnica” of Bucharest,* Romania
Mitică Iustinian NEACĂ – *University of Craiova,* Romania
Petre-Marian NICOLAE – *University of Craiova,* Romania
Dragoş NICULAE – *University “Politehnica” of Bucharest,* Romania
Petru NOTINGHER – *University “Politehnica” of Bucharest,* Romania
Teodor PANĂ – *Technical University of Cluj-Napoca,* Romania
Camelia PETRESCU – *"Gh. Asachi" Technical University of Iaşi*, Romania
Ioan POPA – *University of Craiova,* Romania
Dan POPESCU – *University of Craiova,* Romania
Daniela POPESCU – *University of Craiova,* Romania
Mihaela POPESCU – *University of Craiova,* Romania
Miroslav PRSA – *University of Novi Sad,* Serbia
Mircea M. RĂDULESCU – *Technical University of Cluj Napoca,* Romania
Victoriţa RĂDULESCU – *University “Politehnica” of Bucharest,* Romania
Benoit ROBYNS – *École des Hautes Études d’Ingénieur de Lille,* France
Constantin ROTARU – *Military Technical Academy "Ferdinand I",* Romania
Alexandru SĂLCEANU – *"Gh. Asachi" Technical University of Iaşi*, Romania
Cristina Gabriela SĂRĂCIN – *University “Politehnica” of Bucharest,* Romania
Constantin SĂRMAŞANU-CHIHAI – *"Gh. Asachi" Technical University of Iaşi,* Romania
Florina SCARLATACHE – *"Gh. Asachi" Technical University of Iaşi,* Romania
Dan SELIŞTEANU – *University of Craiova,* Romania
Ioana Gabriela SÎRBU – *University of Craiova,* Romania
Victor ŞONTEA – *Technical University of Moldova,* Moldova
Alexandru STANCU – *"A.I. Cuza" University of Iaşi,* Romania
Ryszard STRZELECKI – *University of Technology Gdansk,* Poland
Flavius-Dan ŞURIANU – *University “Politehnica” of Timişoara,* Romania
Radu-Adrian TÎRNOVAN – *Technical University of Cluj-Napoca,* Romania
Tiberiu TUDORACHE – *University “Politehnica” of Bucharest,* Romania
Raina TZENEVA – *Technical University of Sofia*, Bulgaria
Ioan VADAN – *Technical University of Cluj-Napoca*, Romania
Viorel VARVARA – *"Gh. Asachi" Technical University of Iaşi*, Romania
Ion VLAD – *University of Craiova*, Romania
Ion VONCILĂ – *"Dunărea de Jos" University of Galați,* Romania
Ivan YATCHEV – *Technical University of Sofia*, Bulgaria

CONTENTS

Annals of the University of Craiova, Electrical Engineering series, No. 49, Issue 1, 2025; ISSN 1842-4805 eISSN 2971-9852

DOI: 10.52846/AUCEE.2025.01

Case Studies on the Application of the Exhaustive Optimization Method Based on Screening and Zoom Techniques

Alin-Iulian Dolan[*]

[*] University of Craiova/Electrical Engineering Faculty, Craiova, Romania, adolan@elth.ucv.ro,
ORCID: 0009-0004-2028-4431

Abstract - **The present paper presents an exhaustive optimization method based on screening and zoom techniques and its application in two case studies involving electromagnetic devices. The method is based on the design of experiments technique, combining optimization algorithms with numerical simulations. The solution of the optimization problem is performed in two stages: global modeling (coarse optimization) and actual optimization (fine optimization). In the first stage, a partitioning of the entire feasible domain is performed, especially in the areas where there are extrema of the objective function. Their location is signaled by the sign variations of the local effects of the design variables calculated by a screening technique. In the second stage, the actual optimization takes place using the zoom technique, initiated around the point found in the first stage. The paper concludes with two case studies in which the application of the method on 2-D models of electromagnetic devices is exemplified. The optimization problems are to maximize the developed forces while maintaining the overall dimensions and the cross-sections of the coils, depending on two geometric parameters. The method was applied up to zoom level 5, obtaining a considerable improvement in the performances of the electromagnetic devices. The great advantage of the exhaustive method is the determination of the global extremum of the objective function, which becomes all the more expensive the greater the number of design variables and the finer the partitioning.**

Cuvinte cheie: *optimizare globală, tehnică de screening, proiectarea experimentelor, metoda elementului finit bidimensională.*

Keywords: *global optimization, technique of screening, design of experiments, bi-dimensional finite element method.*

I. INTRODUCTION

Modern optimization techniques are directly linked to numerical simulations through the Design of Experiments (DOE) method [1]-[2], in which real experiments are replaced by numerical ones, much cheaper in terms of time and resources. Many recent works prove the success of these tools [3]-[11].

The utility of DOE was demonstrated in [3] for "scanning" a double-cage induction motor to identify the most influential parameters on efficiency and starting torque.

The same technique was applied in [4] to increase the efficiency of a boiler by reducing the gas-steam ratio and in [5] to adjust design variables to optimize a permanent magnet machine.

The multi-objective optimal design of the geometry of a linear switched reluctance motor with segmented motor with segmental mover was obtained in [6] using a combination of DOE and Kriging model.

In [7], a three-parameter multi-objective optimization of graded metal foam under impulsive load was performed, correlating the finite element method (FEM) and DOE.

The paper [8] proposed a robust design for brushless DC motors by using DOE in the driving cycles, overcoming the problems related to manufacturing tolerances.

In [9], DOE was applied to select certain parameters by the Taguchi method in order to optimize a switched reluctance motor for ceiling fan design.

DOE together with genetic algorithms led in [10] to an optimized design of a novel line-start permanent magnet synchronous with double-squirrel-cage structure and fractional slot concentrated winding and the application of FEM was a validation of the obtained solution.

To investigate the effect of bump structures and loading conditions on the electromigration properties of solder bumps in Wafer-level chip-scale packaging, in [11] Ansys, Noesis Optimus, DOE and response surface methodology (RSM) were used. In this way, the effect of passivation opening, thickness of solder surface metallurgy and loading conditions on the electromigration performance of the solder surface was optimized.

Relatively recent concerns in the field of electromagnetic device optimization and screening technique can be found in [12]-[15].

MATLAB software was the tool used in [12] for the geometric optimization of a guide coil to obtain a maximum levitation force, based on very accurate semi-analytical equations, allowing a fast calculation compared to 3D-FEM analysis.

The paper [13] highlights the optimized shape of an electromagnetic actuator of a bionic robot fish, using an adaptive genetic algorithm. Thus, the noise of the electromagnetic drive was reduced and its endurance was extended.

The efficiency of the screening technique is evident from [14] where it was applied to a novel spherical actuator to detect the influence of the main structural parameters on the output torque and on the waveform distortion rate of the system. Their improvement was obtained through a multi-objective optimization using the genetic algorithm.

A preliminary screening study was required in [15] for the optimization of a micro-electro-mechanical system electro-thermal actuator using a multi-objective particle swarm optimization algorithm that takes into account multi-source uncertainties. The effect was to reduce the problem size and obtain a solution with good robustness.

Recent works [16]-[18] illustrate the application of optimization methods based on DOE technique which aim at maximizing the force developed by DC electromagnets.

Complex versions of the methods by zooms and by slidings of designs are applied in [16] to improve the performance of an electromagnetic device with a sufficiently good convergence rate by iteratively using second-order polynomial models.

Among the optimization methods based on DOE, exhaustive methods are distinguished that allow finding the global extremum, in addition to other possible local extrema. They analyze the entire feasible domain, iteratively focusing on the areas that locate the sought extrema. The ways in which these areas are selected make the difference between the methods.

Paper [17] presents, for a similar electromagnetic device, the solution of an optimization problem by the applying of an exhaustive method in which the refinement of the global extremum search uses the analysis of variance (ANOVA) technique.

In [18], another exhaustive optimization method based on screening and zoom techniques is presented, exemplified on the case study in [16].

This paper extends the scope of the method in [18] to the case study in [17].

II. EXHAUSTIVE OPTIMIZATION METHOD BASED ON SCREENING AND ZOOM TECHNIQUES

Exhaustive (global) optimization methods have the great advantage of determining all the extrema of an objective function (local and global), at the cost of a particularly complex calculation.

In cases where its analytical expression and implicitly its derivatives are not available, but only the values of the objective function at the points of the feasible domain, one can resort to optimization methods based on the design of experiments (DOE) technique [2], which are divided into three categories:

- The method based on 1st order factorial designs;
- The method based on 2nd order factorial designs and response surface methodology (RSM);
- The method based on 1st order factorial designs and screening and zoom techniques.

All methods have in common the global modeling of the feasible domain and are also suitable for constrained domains.

The first method uses a predefined distribution of experimental points, independent of the objective function variations. The accuracy of the result depends on the degree of partitioning of the feasible domain.

The second method starts as the first and additionally calculates for each subdomain a second-order polynomial model of the objective function. Depending on the quality of these models, evaluated by RSM adjustment coefficients, it is decided to refine the partitioning in the subdomains with poor quality models and the evaluation process is resumed. The method is the best for identifying the objective function variations, but very expensive for more than 4 parameters.

The last of the methods starts with global modeling and a screening analysis performed at the level of each subdomain. Where changes in the sign of the objective function slopes are observed, the partitioning is refined and the analysis is resumed, until an acceptable optimum point is found.

The algorithm continues with the actual optimization using the zoom technique, which allows for a very precise estimation of the optimum point. The interest of the method increases in the case of a number of parameters greater than 3, when fractional factorial designs become effective.

The third method will be described in detail in the following and will subsequently be exemplified by its application in two case studies involving electromagnetic devices.

A. Global Modeling

In stage I, the global modeling of the feasible domain takes place, which consists of partitioning it into several subdomains in which full factorial designs are created [2]. If N_i is the number of divisions imposed for dimension i ($i = 1 \div k$), the total number of subdomains N_s is:

$$N_\text{s} = \prod_{i=1}^{k} N_i \tag{1}$$

These are called basic subdomains and have the associated zoom level $\zeta = 1$.

The partitioning operation defines at the same time a regular discretization network that counts

$$N_\text{p} = \prod_{i=1}^{k} \left(N_i + 1\right) \tag{2}$$

points. If full factorial designs are performed in each of the N_s subdomains, the total number of experiments quickly becomes very large, especially for large values of k, which leads to an increase in the cost of the experiments. Therefore, it is recommended to use less expensive variants such as fractional factorial designs, Taguchi designs or Placket-Burman designs.

B. Technique of Screening

Technically, screening a system is equivalent to ranking the effects of input factors on its response [1]-[2]. This involves creating a full factorial design, modifying each factor with maximum amplitude. The number of experiments required increases rapidly when the number of factors k becomes large.

The matrix of experiments is a square matrix X of order 2^k. For $k = 2$ we have:

$$X = \begin{pmatrix} +1 & -1 & -1 & +1 \\ +1 & +1 & -1 & -1 \\ +1 & -1 & +1 & -1 \\ +1 & +1 & +1 & +1 \end{pmatrix} \tag{3}$$

If we denote by $N_{\text{n}k}$ the number of levels taken by the factor k, we have $N_\text{n1} = N_\text{n2} = 2$ (the values +1 and -1 in the experiment matrix). The number of experiments of the full factorial design will be $N = 2^2 = 4$.

The set of corresponding responses is described by a column vector Y with $2^k = 2^2 = 4$ elements:

$$Y = \begin{pmatrix} Y_1 \\ Y_2 \\ Y_3 \\ Y_4 \end{pmatrix} \tag{4}$$

The effect of factor i on response Y is calculated:

$$E_i = \frac{1}{N} \cdot \sum_{j=1}^{N} \left(X_{j,i+1} \cdot Y_j \right) \tag{5}$$

In stage I of the optimization method, the screening technique is applied for each of the N_s basic subdomains. Adjacent subdomains between which there are sign variations of the effects are searched for and if there are, these will be partitioned into 2^k subdomains and the screening analysis will be resumed for the new subdomains with $\zeta = 2$.

The process can continue until a zoom level imposed by the experimenter is reached, when the optimal experimental point is chosen from the set of obtained points. Stage I represents the coarse optimization stage.

C. Technique of Zoom

In the second stage, the actual optimization takes place through the zoom technique initiated from the point found in the first stage [2].

The simplest version of the zoom methods involves creating a full factorial design around the initial point, delimited by 4 neighboring diagonal points and comparing the values of the objective function in the 5 points, followed by choosing the point with the best value and repeating the action around it.

If the central point offers the best value, the next factorial design will have a zoom level ζ higher by one unit. If not, the same zoom level is maintained.

Stage II represents the fine optimization stage which leads to a very precise estimate of the global maximum of the optimization problem.

III. APPLICATION OF THE OPTIMIZATION METHOD ON ELECTROMAGNETIC DEVICES

In the following, the application of the exhaustive optimization method based on the screening and zoom techniques on DC electromagnetic devices will be exemplified.

A. Case Study I (CS I)

As follows from the design methodology from [19], the initial geometry shape and the values of the main geometric parameters of the device 1 can be followed in Fig. 1 and Table I.

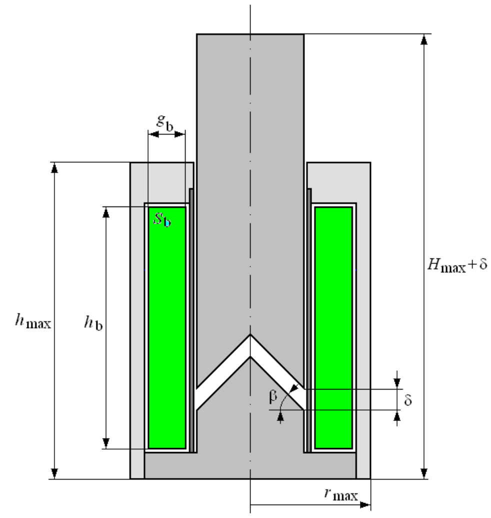

Fig. 1. Initial geometry shape of electromagnetic device 1 (CS I) [16].

TABLE I.
MAIN GEOMETRICAL PARAMETERS OF DC PLUNGER-TYPE ELECTROMAGNET 1 (CS I) [16]

r_1 (mm)	29.80	**g_b (mm)**	19.83	**δ_g (mm)**	2.00
r_2 (mm)	0.00	**h_b (mm)**	138.90	**$S_b=g_b \cdot h_b$ (mm^2)**	2752.27
r_3 (mm)	29.80	**s (mm)**	2.00	**r_{max}**	65.70
β_{in} (°)	45.00	**v (mm)**	24.29	**h_{max}**	172.60
a_0 (mm)	9.07	**h_p (mm)**	192.00	**H_{max}**	231.19
a_1 (mm)	14.90	**b (mm)**	10.00		
a_2 (mm)	14.90	**δ_p (mm)**	1.00		

The air gap for which the study was made is $\delta = 41$ mm. The coil has $w = 1269$ turns and the supply voltage is $U_r = 110$ V DC.

The optimization problem has as objective function the actuation force F to be maximized and as design variables the support angle ratio, k_β, and the coil aspect ratio, k_b:

$$k_\beta = \frac{\beta}{\beta_{in}} \in [0.43 \div 1.56] \tag{6}$$

$$k_b = \frac{h_b}{g_b} \in [6 \div 8] \tag{7}$$

The optimization is subject to four equality constraints that ensure the conservation of the overall dimensions of the device (the external radius r_{max}, the height of carcass h_{max}, the height of plunger + support H_{max}) and the coil cross-section ($S_b = g_b \cdot h_b$). The standard form of the optimization problem (OP$_1$) is written:

$$\mathrm{OP}_1 : \begin{cases} \max F_a(k_\beta, k_b) \\ k_{\beta\min} \le k_\beta \le k_{\beta\max} \\ k_{b\min} \le k_b \le k_{b\max} \\ g_r(k_b) = 0 \\ g_h(k_b) = 0 \\ g_H(k_b) = 0 \\ g_{Sb}(k_b) = 0 \end{cases} \tag{8}$$

At each iteration n, the gain g_n is calculated compared to the initial value ($n = 0$):

$$g_n = \frac{F_n - F_0}{F_0} \cdot 100\,[\%] \tag{9}$$

The results obtained are presented iteratively in Table II, which also mentions the variation of some

TABLE II.
VARIATION OF PARAMETERS ALONG THE OPTIMIZATION ALGORITHM (CS I) [18]

It.	**ζ**	**N_{tot}**	**N_{rec}**	**k_β**	**k_b**	**F (N)**	**g_n (%)**	**β (°)**	**g_b (mm)**	**h_b (mm)**
0	-	1	-	1.000	7.000	656.52	-	45.00	19.83	138.80
1	1	64	40	1.566	6.500	775.32	18.09	70.50	20.58	133.75
2	**2**	**128**	**98**	**1.425**	**6.500**	**810.99**	**23.53**	**63.13**	**20.58**	**133.75**
3	2	5	1	1.425	6.500	810.99	23.53	63.13	20.58	133.75
4	3	5	1	1.460	6.438	812.28	23.73	65.72	20.68	133.11
5	3	5	3	1.460	6.438	812.28	23.73	65.72	20.68	133.11
6	4	5	1	1.460	6.438	812.28	23.73	65.72	20.68	133.11
7	**5**	**5**	**1**	**1.452**	**6.422**	**812.47**	**23.75**	**65.32**	**20.70**	**132.95**
Total		218	145							

geometric parameters.

Stage I starts with the initial point P_0 with coordinates $k_\beta = 1$, $k_b = 7$, with the value $F_0 = 656.52$ N and provides the best point P_1 with coordinates $k_\beta = 1.425$, $k_b = 6.5$ and value $F_2 = 810.99$ N, with a gain of 23.53%, at the zoom level $\zeta = 2$.

Figure 2 illustrates the distribution of the basic subdomains ($\zeta = 1$) and Figs. 3 and 4 show the 2-D, respectively 3-D, experimental points and the optimal point for this zoom level. Figure 5 illustrates the distribution of the subdomains with the zoom level $\zeta = 2$ and Figs. 6 and 7 show the experimental points and the optimal point P_1.

Stage II continues with 5 iterations up to point P_2 with coordinates $k_\beta = 1.452$, $k_b = 6.422$ and the value $F_7 = 812.47$ N, with a gain of 23.75%, at zoom level $\zeta = 5$. Figure 8 illustrates the optimization algorithm using the zoom technique, initiated from point P_1. In Figs. 9-10 the entire optimization algorithm is presented, in 2-D and 3-D visualization.

As the optimization results show, none of the design variables reach their range limits. The total number of numerical experiments required was 218, of which 145 were recovered through iterations, leaving 73 experiments actually performed using the FEMM program [20] and the LUA programming language [21]. The force F was determined using the Maxwell Stress Tensor approach.

In Fig. 11 are presented initial and optimal geometry shape and magnetic flux density distribution computed in FEMM software on an axial-symmetric model.

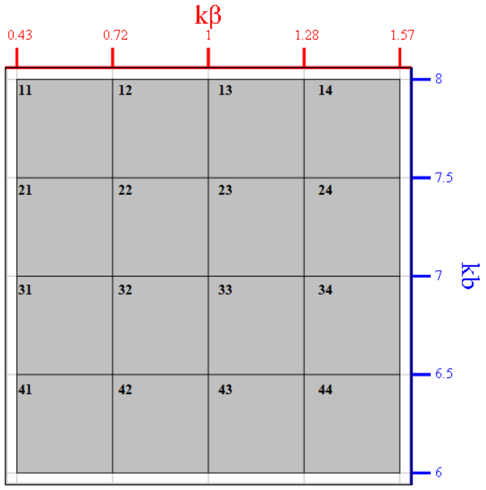

Fig. 2. Distribution of basic subdomains ($\zeta = 1$, CS I) [18].

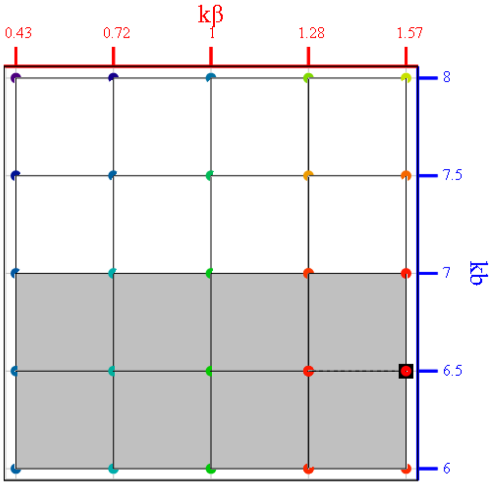

Fig. 3. Experimental points of the basic subdomains ($\zeta = 1$) and the optimal point (in black) for this level (stage I, 2-D view, CS I) [18].

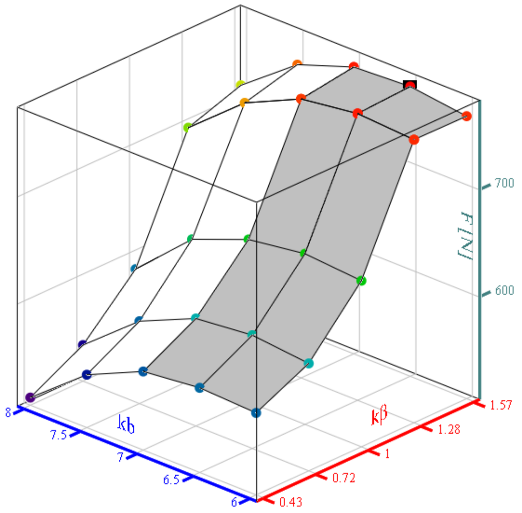

Fig. 4. Experimental points of the basic subdomains ($\zeta = 1$) and the optimal point (in black) for this level (stage I, 3-D view, CS I) [18].

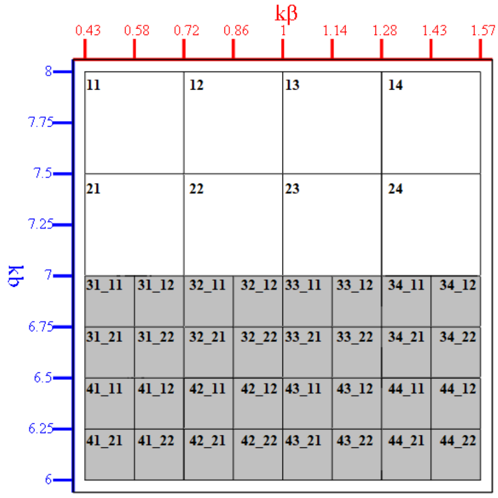

Fig. 5. Distribution of subdomains with zoom level $\zeta = 2$ (CS I) [18].

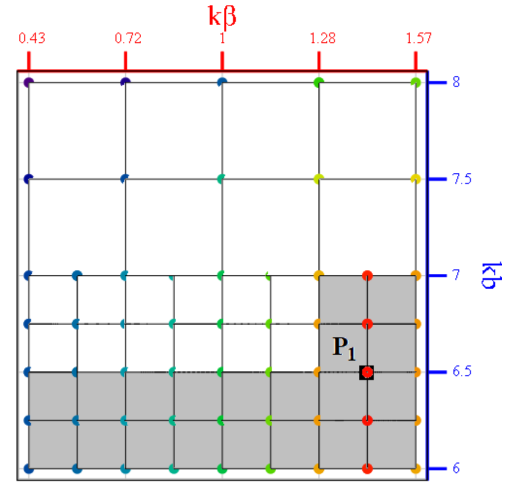

Fig. 6. Experimental points of the subdomains with $\zeta = 2$ and the optimal point P_1 for this level (stage I, 2-D view, CS I) [18].

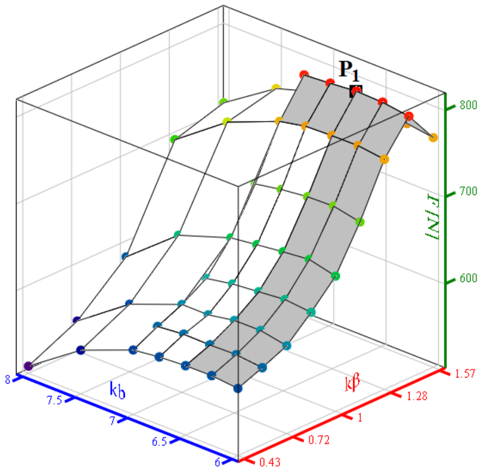

Fig. 7. Experimental points of the subdomains with $\zeta = 2$ and the optimal point P_1 for this level (stage I, 3-D view, CS I) [18].

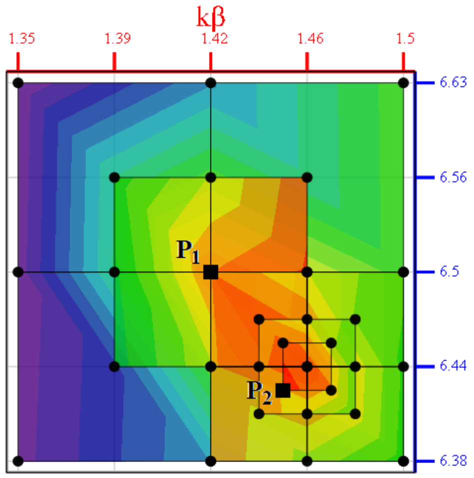

Fig. 8. Experimental points of the subdomains with $\zeta = 2 \div 5$ and the optimal point P_2 for level 5 (stage II, 2-D view, CS I) [18].

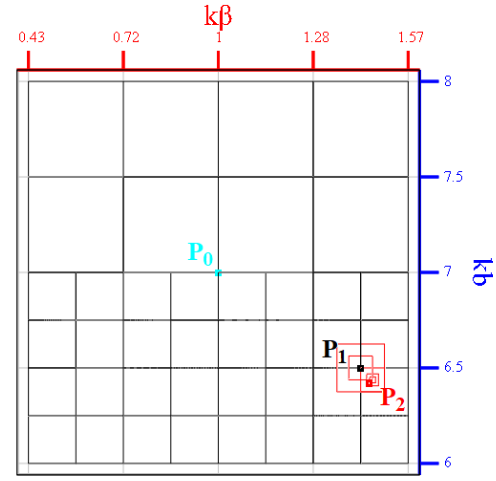

Fig. 9. Optimization algorithm for $\zeta = 1 \div 5$, initial point P_0 and optimal points P_1 (stage I) and P_2 (stage II) (2-D view, CS I) [18].

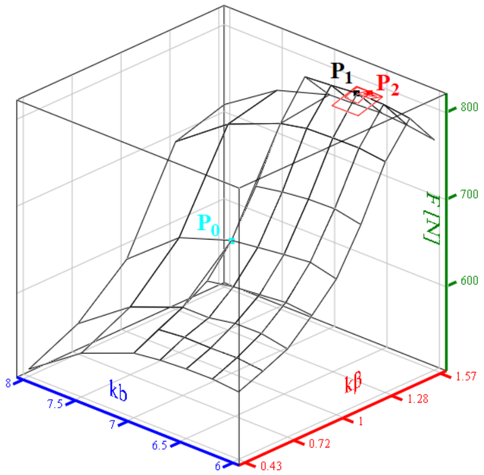

Fig. 10. Optimization algorithm for $\zeta = 1 \div 5$, initial point P_0 and optimal points P_1 (stage I) and P_2 (stage II) (3-D view, CS I) [18].

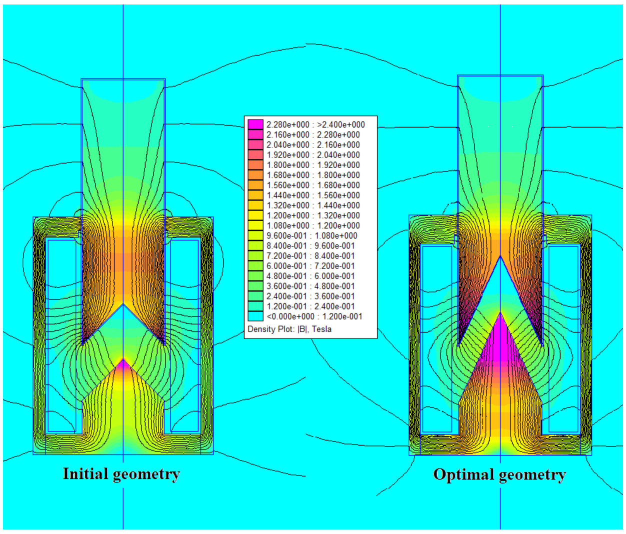

Fig. 11. Initial and optimal geometry shape and magnetic flux density distribution (axial-symmetric solution, FEMM, CS I) [18].

B. *Case Study II (CS II)*

The initial geometry shape and the values of the main geometric parameters of the device 2 can be followed in Fig. 12 and Table III. The air gap for which the study was made is $\delta = 1$ mm. The coil has $w = 11500$ turns and the supply voltage is $U_r = 115$ V DC.

The optimization problem has as objective function the actuation force F to be maximized and as design variables the ratio between the height and thickness of the coil, k_b, and the ratio between the thicknesses of the core yokes, k_{my}:

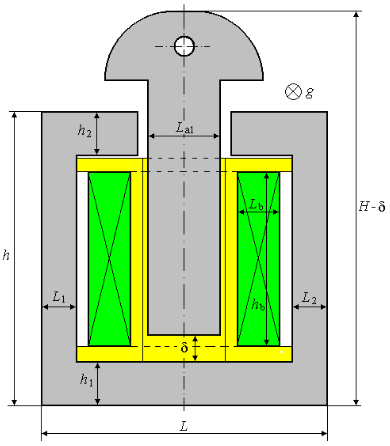

Fig. 12. Initial geometry of electromagnetic device 2 (CS II) [16].

TABLE III.
MAIN GEOMETRICAL PARAMETERS OF DC PLUNGER-TYPE ELECTROMAGNET 2 (CS II) [16]

h (mm)	52.50	**L_{a1in} (mm)**	13.00
H (mm)	65.70	**L_{1in} (mm)**	7.35
L (mm)	50.90	**L_{2in} (mm)**	7.35
$S_b = L_b \cdot h_b$ (mm^2)	234.00	**L_{bin} (mm)**	7.50
h_{1in} (mm)	7.90	**h_{bin} (mm)**	31.20
h_{2in} (mm)	7.90	**g (mm)**	19.80

$$k_b = \frac{h_b}{L_b} \in [2 \div 6] \tag{10}$$

$$k_{my} = \frac{h_2}{h_1} \in [0.5 \div 2] \tag{11}$$

The optimization is subject to four equality constraints that ensure the conservation of the overall dimensions of the device (core width L, core height h, total device height H) and the coil cross-section ($S_b = g_b \cdot h_b$). The standard form of the optimization problem (OP$_2$) is written:

$$\mathrm{OP}_2: \begin{cases} \max F(k_b, k_{my}) \\ k_{b\min} \le k_b \le k_{b\max} \\ k_{my_{\min}} \le k_{my} \le k_{my_{\max}} \\ g_h(k_b, k_{my}) - h = 0 \\ g_L(k_b) - L = 0 \\ g_H(k_b, k_{my}) - H = 0 \\ g_{Sb}(k_b) - S_b = 0 \end{cases} \tag{12}$$

The results obtained are presented iteratively in Table IV, which also mentions the variation of some geometric parameters.

Stage I starts with the initial point P$_0$ with coordinates $k_b = 4$, $k_{my} = 1.25$, with the value $F_0 = 22.939$ N and provides the best point P$_1$ with coordinates $k_b = 2.5$, $k_{my} = 2$ and value $F_2 = 24.924$ N, with a gain of 8.66%, at the zoom level $\zeta = 2$.

Figure 13 illustrates the distribution of the basic subdomains ($\zeta = 1$) and Figs. 14 and 15 show the 2-D, respectively 3-D, experimental points and the optimal point for this zoom level. Figure 16 illustrates the distribution of the subdomains with the zoom level $\zeta = 2$ and Figs. 17 and 18 show the experimental points and the optimal point P$_1$.

TABLE IV.
VARIATION OF PARAMETERS ALONG THE OPTIMIZATION ALGORITHM (CS II)

It.	**ζ**	**N_{tot}**	**N_{rec}**	**k_b**	**k_{my}**	**F (N)**	**g_n (%)**	**L_b (mm)**	**h_b (mm)**	**h_1 (mm)**	**h_2 (mm)**
0	-	1	-	4.00	1.25	22.939	-	7.65	30.59	7.29	9.11
1	1	64	40	3.00	2.00	24.818	8.19	8.83	26.50	6.84	13.67
2	**2**	**128**	**98**	**2.50**	**2.00**	**24.924**	**8.66**	**9.67**	**24.19**	**7.60**	**15.21**
3	2	5	1	2.50	2.00	24.924	8.66	9.67	24.19	7.60	15.21
4	3	5	1	2.63	2.00	24.918	8.63	9.44	24.78	7.41	14.81
5	3	5	3	2.50	2.00	24.924	8.66	9.67	24.19	7.60	15.21
6	4	5	3	2.63	2.00	24.918	8.63	9.44	24.78	7.41	14.81
7	**5**	**5**	**3**	**2.50**	**2.00**	**24.924**	8.66	**9.67**	**24.19**	**7.60**	**15.21**
Total		218	149								

Stage II continues with 5 iterations up to point P$_2$ with coordinates $k_b = 2.5$, $k_{my} = 2$ and value $F_7 = 24.924$ N, with a gain of 8.66%, at zoom level $\zeta = 5$. Figure 19 illustrates the optimization algorithm using the zoom technique, initiated from point P$_1$. In Figs. 20-21 the entire optimization algorithm is presented, in 2-D and 3-D visualization.

As the optimization results show, one of the design variables reaches its range limit. The total number of numerical experiments required was 218, of which 149 were recovered through iterations, leaving 69 experiments actually performed using the FEMM program [20] and the LUA programming language [21]. The force F was determined using the Maxwell Stress Tensor approach.

In Fig. 22 are presented initial and optimal geometry shape and magnetic flux density distribution computed in FEMM software on a planar model.

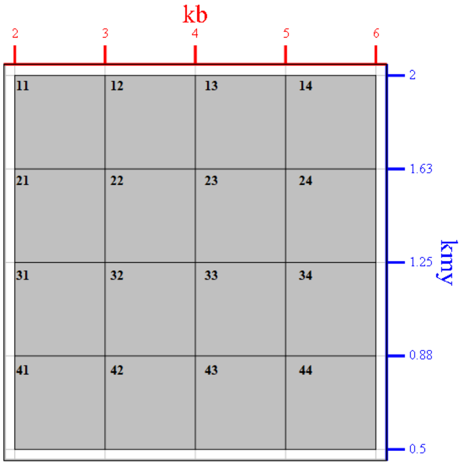

Fig. 13. Layout of basic subdomains ($\zeta = 1$, CS II).

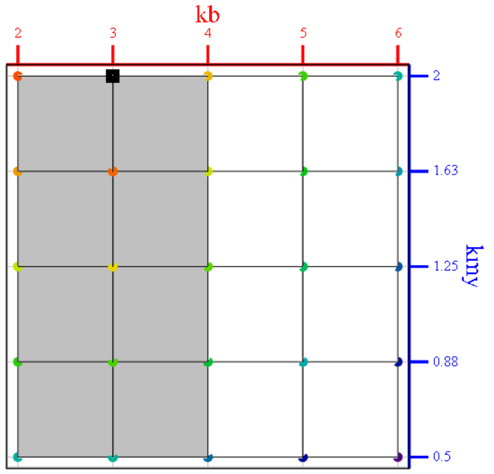

Fig. 14. Experimental of the basic subdomains (ζ = 1) and the optimal point (in black) for this level (stage I, 2-D view, CS II).

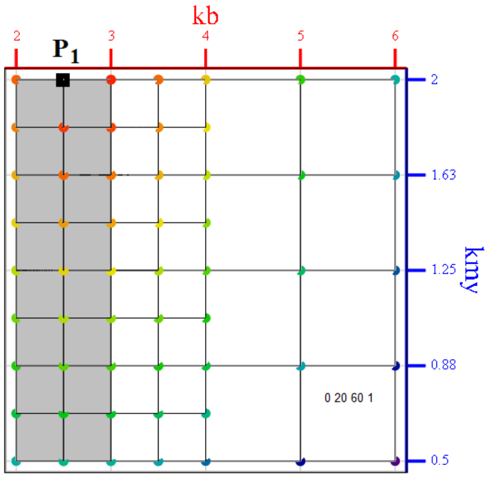

Fig. 17. Experimental points of the subdomains with ζ = 2 and the optimal point P_1 for this level (stage I, 2-D view, CS II).

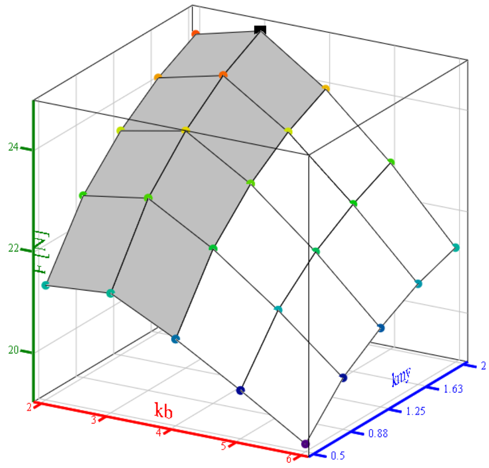

Fig. 15. Experimental points of the basic subdomains (ζ = 1) and the optimal point (in black) for this level (stage I, 3-D view, CS II).

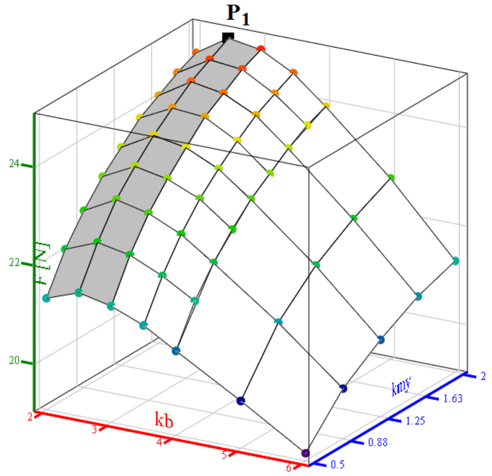

Fig. 18. Experimental points of the subdomains with ζ = 2 and the optimal point P_1 for this level (stage I, 3-D view, CS II).

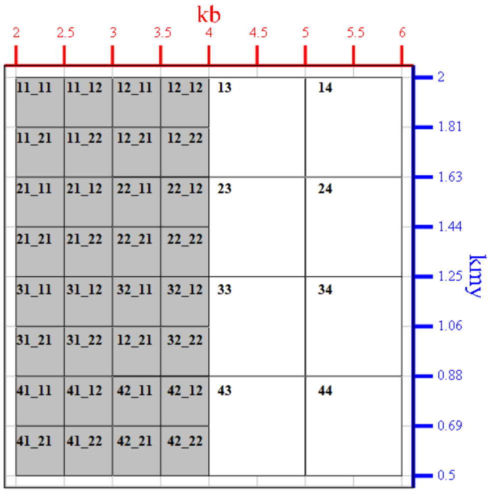

11_11	11_12	12_11	12_12	13	14
11_21	11_22	12_21	12_22		
21_11	21_12	22_11	22_12	23	24
21_21	21_22	22_21	22_22		
31_11	31_12	32_11	32_12	33	34
31_21	31_22	12_21	32_22		
41_11	41_12	42_11	42_12	43	44
41_21	41_22	42_21	42_22		

Fig. 16. Distribution of subdomains with zoom level ζ = 2 (CS II).

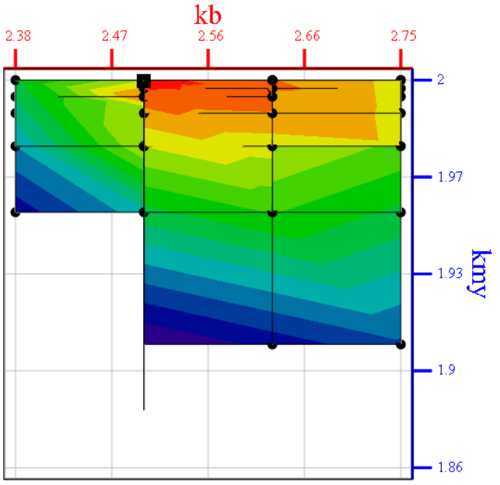

Fig. 19. Experimental points of the subdomains with ζ = 2÷5 and the optimal point P_2 for level 5 (stage II, 2-D view, CS II).

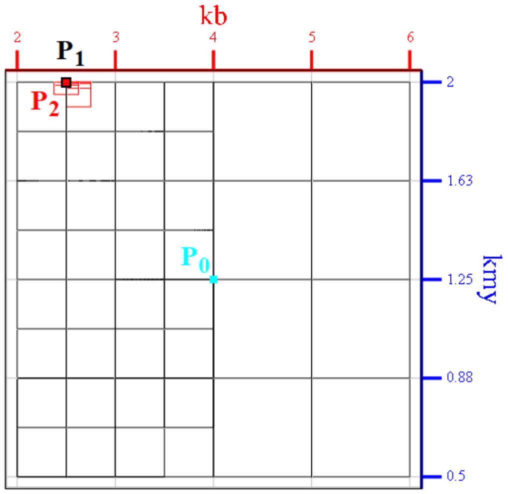

Fig. 20. Optimization algorithm for $\zeta = 1 \div 5$, initial point P_0 and optimal points P_1 (stage I) and P_2 (stage II) (2-D view, CS II).

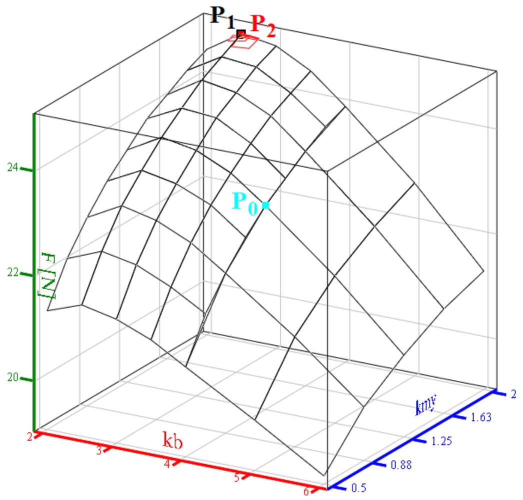

Fig. 21. Optimization algorithm for $\zeta = 1 \div 5$, initial point P_0 and optimal points P_1 (stage I) and P_2 (stage II) (3-D view, CS II).

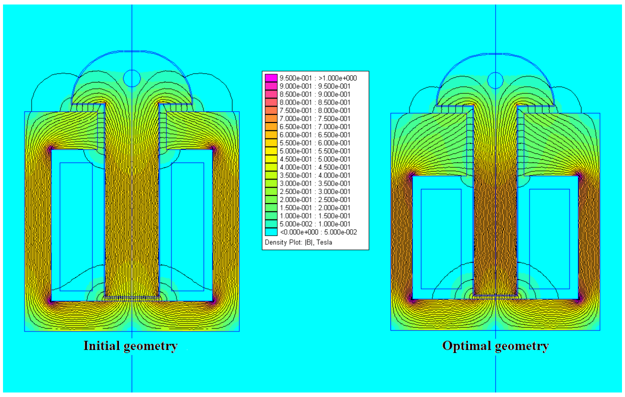

Fig. 22. Initial and optimal geometry shape with magnetic flux density distribution (planar solution, FEMM, CS II).

IV. CONCLUSIONS

In this paper, an exhaustive optimization method based on screening and zoom techniques from the field of experimental design was presented. The method is structured in two stages. The first represents a global modeling of the feasible domain, with a higher degree of refinement in the subdomains where changes in the slope of the objective function are found, through screening analyses. The second stage is the actual optimization using the zoom technique to improve the result of the first stage.

The application of the method was exemplified in two case studies of electromagnetic devices for which 2-D numerical models were obtained using the FEMM program. In the first case study, in the global modeling stage, 23.53% was gained and in the actual optimization stage, the percentage increased to 23.75% of the initial value. In the second case study, the gain was obtained only in the global modeling stage, of 8.66%, but it did not improve in the second stage.

Thanks to the second stage of actual optimization through the zoom technique, the presented method proves to be very accurate compared to other exhaustive methods.

From the point of view of the magnetic circuit, the solution obtained for the first case leads to a pronounced saturation of the plunger and its support, which indicates the need to take into account the saturation level as an additional design variable. The geometric asymmetry of the solution for the second case may have some consequences from the point of view of mechanical stability, which would require reducing the upper limit of the design variable k_{my}.

ACKNOWLEDGMENT

Source of research funding in this article: Research program of the Electrical Engineering Department financed by the University of Craiova.

Contribution of authors:
First author – 100%

Received on September 25, 2025
Editorial Approval on December 2, 2025

REFERENCES

[1] D. Montgomery, *Design and Analysis of Experiment*, 5-th Edition, Arizona State University, 2000.

[2] S. Vivier, *Optimization Strategies Using the Design of Experiments Method and Applications to Electrotechnical Devices Modeled by Finite Elements* (In French), Ph-D Thesis, Lille, 2002.

[3] A.-I. Constantin, and V. Fireteanu, “HyperSudy optimization of induction motors finite element assisted design,” International Aegean Conference on Electrical Machines and Power Electronics (ACEMP) & 2021 International Conference on Optimization of Electrical and Electronic Equipment (OPTIM), pp. 191-197, 2021, doi: 10.1109/OPTIM-ACEMP50812.2021.9590030.

[4] L. Liu, K. Xu, X. He, and X. Cao, “Energy-saving optimization of the gas-fired boiler by DOE method,” Proceedings of the X-th International Forum on Electrical Engineering and Automation (IFEEA), Nanjing, China, pp. 8-12, 2023, doi: 10.1109/IFEEA60725.2023.10429450.

[5] N. Taran, V. Rallabandi, D.-M. Ionel, G. Heins, D. Patterson, and P. Zhou, “Design optimization of electric machines with 3-D FEA and a new hybrid DOE-DE numerical algorithm,” Proceedings of IEEE International Electric Machines & Drives Conference

(IEMDC), May 12-15, San Diego, CA, USA, pp. 603-608, 2019, doi: 10.1109/IEMDC.2019.8785088.

[6] X. Yi, C. Zhu, C. Huang, D. Wang, and X. Wang, "Design optimization of linear switched reluctance motor with segmental mover," XIII-th Int. Symposium on Linear Drives for Industry Applications (LDIA), July 01-03, Wuhan, China, pp. 1-6, 2021, doi: 10.1109/LDIA49489.2021.9505921.

[7] A. Bassiri Nia, M.Y. Yahya, and A. Faraokhi Nejad, "Optimization of graded metallic foam subjected to impulsive loading through DOE approach," IX-th International Conference on Mechanical and Aerospace Engineering, July 10-13, Budapest, Hungary, pp. 295-299, 2018, doi: 10.1109/ICMAE.2018.8467559.

[8] F. Mahmouditabar, A. Vahedi, and N. Takorabet, "Robust design of BLDC motor considering driving cicle," *IEEE Transaction on Transp. Electrification*, Vol. 10, No. 1, pp. 1414-1424, March, 2024, doi: 10.1109/TTE.2023.3285650.

[9] V.K. Singh, and B. Singh, "Design and development of efficient energy outer rotor switched reluctance motor for ceiling fan," IEEE International Electric Machines & Drive Conference (IEDMC), May 15-18, San Francisco, USA, pp. 1-7, 2023, doi: 10.1109/IEMDC55163.2023.10238847.

[10] X. Li, J. Gong, X. Wang, N. Bracikowski, and F. Gillon, "Proposal of a novel line-start permanent magnet synchronous machine using fractional slot concentrated winding," XXVI-th International Conference on Electrical Machines and Systems (ICEMS), Nov. 05-08, Zhuhai, China, pp. 3027-3032, 2023, doi: 10.1109/ICEMS59686.2023.10344658.

[11] L. Du, S. Deng, Z. Cui, R. Poelma, C. Beelen-Hendrikx, and K. Zhang, "Multi-parameters optimization for electromigration in WLCSP solder bumps," XXV-th International Conference on Thermal, Mechanical and Multi-Physics Simulation and Experiments in Microelectronics and Microsystems (EuroSimE), April 07-10, Catania, Italy, pp. 1-4, 2024, doi: 10.1109/EuroSimE60745.2024.10491411.

[12] M. Lahdo, T. Ströhla, and S. Kovalev, "Magnetically levitated planar positioning systems based on Lorentz forces," 11th International Symposium on Linear Drives for Industry Applications (LDIA), September, 06-08, Osaka, Japan, pp. 1-6, 2017, doi: 10.23919/LDIA.2017.8097232.

[13] H. Zhu, Z. Zhang, R. Zhang, Y. Gao, M. Yang, Y. Li, X. Ni, T. Zhou, S. Zhang, and C. Zhu, "Optimization design of electromagnetic actuator for bionic robotic fish based on genetic algorithm," International Conference on Machine Learning, Control, and Robotics (MLCR), October, 29-31, Suzhou, China, pp. 148-152, 2022, doi: 10.1109/MLCR57210.2022.00035.

[14] L. Zhang, L.Yan, and Z. Dong, „Optimization of a novel spherical actuator with 3-D DOF motion," 18th Conference on Industrial Electronics and Applications (ICIEA), September, 11, Ningbo, China, pp. 1-6, 2023, doi: 10.1109/ICIEA58696.2023.10241512.

[15] H. Zhu, Y. Cao, X. Kong, S. Lei, H. Lu, W. Nie, and Z. Xi, „Selecting robust multi-objective optimization of a MEMS electrothermal actuator considering multi-source uncertainties," *IEEE Transaction on Electron Devices*, Vol. 70, No. 7, pp. 3820-3827, 2023, doi: 10.1109/TED.2023.3278621.

[16] A.-I. Dolan, "Polynomial models used in optimization by design of numerical experiments", *Annals of the University of Craiova, Series: Electrical Engineering*, No. 48, Issue 1, Universitaria Publishing House, pp. 46-54, 2024, doi: 10.52846/AUCEE.2024.07.

[17] A.-I. Dolan, "Exhaustive optimization method applied on electromagnetic device," *Annals of the University of Craiova, Series: Electrical Engineering*, No. 46, Issue 1, Universitaria Publishing House, pp. 34-41, 2022, doi: 10.52846/AUCEE.2022.06.

[18] A.-I. Dolan, "Exhaustive optimization method based on screening and zoom techniques applied to an electromagnetic device", Proceedings of the XV-th International Conference on Electromechanical and Power Systems (SIELMEN 2025), October 15-17, Iasi-Chisinau, pp. 531-536, 2025, doi: 10.1109/SIELMEN67352.2025.11260691.

[19] G. Hortopan, *Electrical Apparatus of Low Voltage* (in Romanian), Bucharest: Tehnica Publishing House, 1969.

[20] https://www.femm.info/wiki/HomePage

[21] https://www.lua.org/

DOI: 10.52846/AUCEE.2025.02

Considerations on Switching Capability of Circuit Breakers under Earth Fault in Electrical Grid

Cristian-Eugeniu Sălceanu[*], Daniela Iovan[*], Daniel-Constantin Ocoleanu[*],
Marius Boncea[*] and Stefan-Marius Seitan[*]
[*] National Institute for Research Development and Testing in Electrical Engineering ICMET Craiova,
Craiova, Romania, csalceanu@icmet.ro, ORCID: 0009-0000-5486-9818, pdaniela@icmet.ro,
ORCID: 0009-0001-6142-3125, pramlmp@icmet.ro, ORCID: 0000-0003-2633-751X, bonceamarius@icmet.ro,
ORCID: 0009-0002-1009-4592, seitan_stefan@yahoo.com, ORCID: 0009-0003-6528-2395

***Abstract* - Circuit-breakers are essential for the safety and reliability of electrical power systems by interrupting fault currents under various conditions. Circuit-breakers must be capable of breaking single-phase short-circuit currents which can occur in two distinct scenarios. The first scenario involves effectively earthed neutral systems, where single-phase faults can generate high fault currents that the circuit-breaker must safely interrupt to prevent equipment damage and ensure personnel safety. The second scenario occurs in non-effectively earthed neutral systems, where double earth faults can appear on two separate phases, with one fault occurring on one side of the circuit-breaker and the other on the opposite side. Such conditions pose significant challenges for circuit-breaker design and operation, requiring careful consideration of their dynamic response and fault current interruption capacity. This paper presents the expected behavior of the circuit breakers and the real-life situations encountered during high-power testing of this type of equipment. Real-life testing reveals critical insights into performance limitations, transient phenomena, and operational reliability, providing valuable information for both equipment manufacturers and system designers. The study highlights the importance of accurate modeling, thorough testing, and adherence to standards to ensure that circuit-breakers perform reliably under all anticipated fault conditions. The most severe condition is identified as a double earth fault occurring under phase opposition. Although additional tests are planned to confirm this, preliminary assessment suggests that under normal operating conditions (0° < φ < 30°), the current at the final breaking pole should not exceed the generator's short-circuit current.**

Cuvinte cheie: *întreruptoare, defect de punere la pământ, mare putere, teste.*

Keywords: *circuit-breaker, earth fault, high power, tests.*

I. INTRODUCTION

The switchgear operates correctly when it eliminates the short circuit in an optimal time without any consequences that endanger the system, defined by the type and class of the switchgear [1], [6]. The switching process is characterized by a number of physical phenomena that are determined by the type of switching device and its operating parameters. The switching characteristics of electrical devices are defined by the following parameters:

- Breaking capacity - defined as the highest value of the real or assumed current, measured as the effective value at the moment of contact separation, which can be interrupted by the switchgear without damage, with explicit specification of the main parameters of the reference transient recovery voltage (characterized by the parameters of the power line) [2], [3];

- Rated Peak Withstand Current - defined as the highest value of current, measured as a peak value, that the switchgear can break at a given voltage without damage;

- The operating frequency recovery voltage (RV), in the event of a short circuit across the terminals, is the voltage value that appears between the contacts after the arc is extinguished [1], [7];

- Transient recovery voltage (TRV) consists of high frequency voltage oscillations. In the case of high power tests, in three-phase mode, the recovery voltage has the value $kU_n/\sqrt{3}$ in the case of the first phase that interrupts the current and $U_n/\sqrt{3}$ in the case of the other two phases that interrupt the arc, where k is the factor of the first pole and has the value 1.3 or 1.5, depending on how the neutral of the network is earthed (by resistance or inductance) or insulated. In the case of tests, the value of the recovery voltage is allowed to drop to 95% of the specified value during the test and must be maintained for a minimum of 300 ms in the case of circuit breakers. The transient recovery voltage wave has an aperiodic shape.

- The voltage applied to the circuit breaker terminals is the rated voltage of the system. The average applied voltage for each phase must be at least equal to the rated voltage $U_n/\sqrt{3}$ and must not exceed this value by more than 10%. For single-phase testing of a three-pole circuit breaker, the applied voltage shall be at least equal to the value of the phase voltage multiplied by 1.3 or 1.5, and for single-pole circuit breakers, the applied voltage shall be at least equal to the rated value.

- The power factor of the test circuit is standardized for circuit breakers $cos\varphi \leq 0.15$ and can be determined from the time constant of the circuit or from the aperiodic component of the short-circuit current [6], [7].

II. SINGLE AND DOUBLE EARTH FAULT TESTS

A. *Use Cases*

In the laboratory, the single earth fault case consists of a single-phase test of one side pole of the circuit-breaker to interrupt the short-circuit current at rated value I_{sc} under the action of voltage $U_n/\sqrt{3}$.

The double earth fault situation occurs when the neutral of the system is isolated or not firmly earthed by the simultaneous earthing of two different phases, one upstream and one downstream of the circuit-breaker, in the case of the earthing of two phases, one on the load side and one on the supply side, considered as a double earth fault.

Depending on the type of connection of the neutral of the system in which the circuit-breaker is used, its operating mechanism and the short-circuit test scheme (single-phase or three-phase) in the T100$_S$ sequence of the circuit-breaker, additional single-phase short-circuit tests must be carried out on the terminals according to Table 1.

The purpose of these tests is:

- to verify that the circuit-breaker is able to interrupt the fault current on a single pole with the parameters set;

- to verify that the opening action of the operating mechanism common to all poles is not affected by the high forces generated by the single-phase short-circuit current at that pole [4], [5].

TABLE I.
TEST PARAMETERS

Single-pole or three-pole circuit breaker with common mechanism for operating the poles		
Grounded neutral network K_{pp}=1.0 or 1.3		Resonant neutral grounding or isolated neutral network $K_{pp}=1.5$
Single earth fault test		Double earth fault test
The T100 test is single-phase	The T100 test is three-phase	Further tests are performed: $I = 0.87\ I_{sc}$ $U = U_n$
No further testing	Further tests are performed: $I = I_{sc}$ nom $U = U_n/\sqrt{3}$	

B. *The Test Sequence*

The test sequence consists of a single opening operation. The test should be carried out on the outer pole, which results in maximum stress on the actuating mechanism. The arcing time for this sequence must not be shorter than the value given by the relation: $t_a \geq t_{a\ 100s} + 0{,}7\ T/2$, where $t_{a\ 100s}$ is:

- The minimum arcing time for the breaking pole after three opening operations in sequence T100s (if T100s is carried out in three-phase scheme);
- Minimum arcing time after a T100s sequence (if T100s is carried out in single-phase schemes);
- *T* - duration of the current.

Single earth fault tests shall be carried out on one of the side poles where the operating mechanism is subjected to maximum stress, and double earth fault tests may be carried out on either pole.

In the case of two tests in a single-phase scheme on a three-pole circuit-breaker with a common operating mechanism, they must be carried out on two different poles in order to avoid stressing a single pole.

C. *The Test Voltage*

The test voltage must be equal to the rated voltage of the circuit-breaker for the double earth fault test and $U_n/\sqrt{3}$ for the single earth fault test. The following TRV values shall be used:

a) for single earth fault:

- 2-parameter TRV:

$$u_{c,sp} = 1{,}4\frac{U_n\sqrt{2}}{\sqrt{3}}\ (kV);\ t_{3,sp} = \frac{u_{c,sp}}{\frac{u_c}{t_3}}\ (\mu s); \qquad (1)$$

- 4-parameter TRV:

$$u_{1,sp} = 1{,}4\frac{U_n\sqrt{2}}{\sqrt{3}}\ (kV);\ t_{1,sp} = \frac{u_{c,sp}}{\frac{u_c}{t_1}}\ (\mu s); \qquad (2)$$

$$u_{c,sp} = 1{,}4\ u_{1,sp}\ (kV);\ t_{2,sp} = 3t_{1,sp}\ (\mu s); \qquad (3)$$

b) for double earth fault:

- 2-parameter TRV:

$$u_{c,sp} = 1{,}4U_n\sqrt{2}\ (kV);\ t_{3,sp} = \frac{u_{c,sp}}{\frac{u_c}{t_3}}\ (\mu s); \qquad (4)$$

- 4-parameter TRV:

$$u_{1,sp} = 1{,}4U_n\sqrt{2}\ (kV);\ t_{1,sp} = \frac{u_{c,sp}}{\frac{u_c}{t_1}}\ (\mu s); \qquad (5)$$

$$u_{c,sp} = 1{,}4u_{1,sp}\ (kV);\ t_{2,sp} = 3t_{1,sp}\ (\mu s); \qquad (6)$$

D. *The Test Current (I_{sc})*

The test current (I_{sc}) for the single-phase double earth fault test according to IEC 62271-100 is 87% of the rated short-circuit breaking capacity at the terminals. The DC component of the interrupted current must not exceed 20% of the AC component [7], [8].

The test current for the single earth fault test is equal to the rated breaking capacity of the circuit-breaker.

III. SINGLE AND DOUBLE EARTH FAULTS IN POWER PLANTS

In power plant substations where the connection between the generator and the associated step-up transformer is made via generator busbars (IPB), three-phase faults occur very rarely. The most probable faults are single-phase phase-to-earth faults and phase opposition. Single earthing faults in a system with a firmly earthed neutral sometimes result in a secondary fault on another phase due to the high transient voltages that occur with this type of fault.

A generator together with its step-up transformer forms such a system: the neutral of the generator is normally earthed by a high ohmic resistor or preferably by a Petersen coil, or generally by a high impedance (including an insulated neutral), and the low voltage (LV) part of the step-up transformer is normally connected in delta [5], [11].

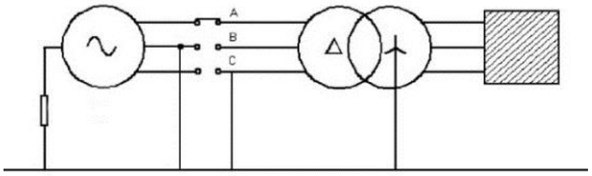

Fig. 1. Synchronous generator - circuit breaker - step-up transformer - high voltage circuit, double earthing on phases B and C.

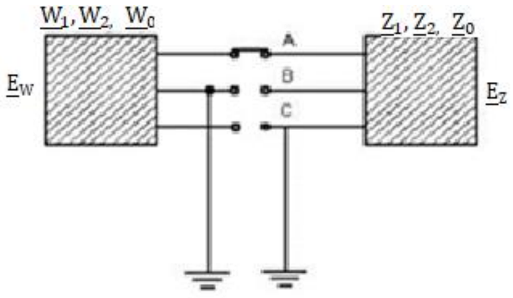

Fig. 2. Two systems connected by a circuit-breaker, double earth fault on phases B and C, current on the last pole interrupting the current.

If both faults are located on the same side of the circuit-breaker, we have a classic double earth fault with respect to the circuit-breaker. Fault currents, the current flowing through the circuit-breaker and the transient recovery voltage are defined in technical standards.

However, the load on the circuit-breaker is different if the earth faults are located on different parts of the circuit-breaker. Assuming that the pole of the circuit-breaker on the valid phase breaks last, it must interrupt a fault current under the influence of a transient recovery voltage composed of the voltage on the generator side plus the voltage on the transformer side.

Theoretically, we have two three-phase voltage sources (synchronous generator and high-voltage system) with their own impedances connected to one phase and through the earth fault to the other two (the streamlined diagram is shown in Fig.1).

Current Through The Last Interrupting Pole

The analysed situation is shown in Fig. 2. It should be noted that when poles A and B or A and C are closed, the currents flowing through these poles are different, so that interruption of phases B and C does not automatically mean interruption of phase A.

In Fig. 2, a W system (synchronous generator) is defined on the left and a Z system (high-voltage step-up transformer) on the right. Both systems are characterized by complex impedances in symmetrical components (the short-circuit impedances), in the following referred to as W_1, W_2, W_0 or Z_1, Z_2, Z_0 and the voltages E_W and E_Z.

It is assumed that the earth faults are on phase B on the W side and on phase C on the Z side, and that the B and C poles of the circuit-breaker are already open. The last phase to interrupt the current is therefore phase A.

The following conditions were defined:

$$I_{WA} = -I_{ZA};$$

$$I_{WC} = I_{ZB} = 0;$$

$$U_{WA} = U_{ZA};$$

$$U_{WB} = U_{ZC} = 0.$$

Given $a = e^{j120^\circ}$ and $a^2 = e^{-j120^\circ}$, the sequence of currents is:

$$I_{W1}+I_{W2}+I_{W0}=-I_{Z1}-I_{Z2}-I_{Z0};$$

$$aI_{W1}+a^2I_{W2}+I_{W0}=0;$$

$$a^2I_{Z1}+aI_{Z2}+I_{Z0}=0;$$

and the sequence of voltages:

$$U_{W1}+U_{W2}+U_{W0}=U_{Z1}+U_{Z2}+U_{Z0};$$

$$a^2U_{W1}+aU_{W2}+U_{W0}=0;$$

$$aU_{Z1}+a^2U_{Z2}+U_{Z0}=0.$$

The relationship between the voltage sequence and the current sequence is given by the following equations:

$$U_{W1}=E_W-W_1I_{W1};$$

$$U_{W2}=-W_2I_{W2};$$

$$U_{W0}=-W_0I_{W0};$$

$$U_{Z1}=E_Z-Z_1I_{Z1};$$

$$U_{Z2}=-Z_2I_{Z2};$$

$$U_{Z0}=-Z_0I_{Z0}.$$

The system of equations can be solved by substitution and gives the values of the current and voltage sequences as functions of E_W, E_Z, and impedances. Retransforming to phase values gives the general expression of the current through the last interrupting pole [9], [10], [12].

$$\underline{I}_{WA} = \\ = \frac{(1-\underline{a})[\underline{E}_Z(\underline{W}_1+\underline{W}_2+\underline{W}_0)(\underline{a}^2\underline{Z}_2-\underline{Z}_0)+\underline{E}_W(\underline{Z}_1+\underline{Z}_2+\underline{Z}_0)(\underline{W}_2-\underline{a}^2\underline{W}_0)]}{(\underline{Z}_1+\underline{Z}_2+\underline{Z}_0)(\underline{W}_1\underline{W}_0+\underline{W}_2\underline{W}_0+\underline{W}_1\underline{W}_2)+(\underline{W}_1+\underline{W}_2+\underline{W}_0)(\underline{Z}_1\underline{Z}_0+\underline{Z}_2\underline{Z}_0+\underline{Z}_1\underline{Z}_2)} \tag{7}$$

For simplicity, the following assumptions are made:

- all impedances are predominantly inductive and have the same angle (same *X*/*R* ratio);
- positive and negative sequence impedances are equal;
- the absolute values for E_W and E_Z are equal ($E_W=E_Z e^{j\varphi}$);
- a realistic hypothesis for the configuration in Fig. 1 is that $W_0=Z_0\rightarrow\infty$.

Thus, we can define the simplified equation for the current in phase A:

$$I_{WA} = \frac{a-1}{2}\frac{E_Z + a^2 E_W}{W_1+Z_1} = \frac{a-1}{2}\frac{E_Z(1+e^{j(\varphi-120^\circ)})}{W_1+Z_1}$$

$$|I_{WA}| = \frac{\sqrt{3}}{2}\left|\frac{E_Z}{W_1+Z_1}\right|\left|(1+e^{j(\varphi-120^\circ)})\right|$$

$$= \frac{\sqrt{3}}{2}\left|\frac{E_Z}{W_1+Z_1}\right||F(\varphi)| \tag{8}$$

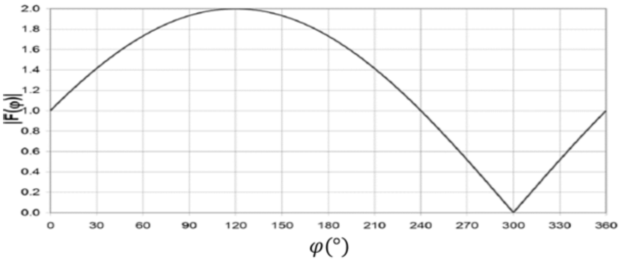

Fig. 3. Graph of $F(\varphi)$ function for $W_0=Z_0\rightarrow\infty$ and $E_W=E_Z e^{j\varphi}$.

Figure 3 shows $F(\varphi)$ as a function of angle φ. Note that for $\varphi=0°$, the generator is operating at no load. For the maximum of 2, the angle is 120°.

In power plants, the range of Z_1 is between 0.5 W_1 and $1W_1$. The phase A current on the I_{WA} supply side has the highest value when $Z_1=0{,}5W_1$. In this situation, equation (8) is simplified:

$$|I_{WA}| = \left|\frac{E_Z}{W_1}\right|\frac{1}{\sqrt{3}}|F(\varphi 0| \tag{9}$$

E_Z/W_1 is the synchronous generator short-circuit current.

Thus, under normal operating conditions ($0°<\varphi<30°$), the current on phase A remains below the generator short-circuit current. In summary, this value is exceeded only under phase shift conditions (by a factor of $\frac{2}{\sqrt{3}} = 1{,}15$ at an angle of 120°).

IV. EXPECTED RESULTS

Using assisted simulation, predicted values were obtained for the single and double earth fault tests.

Figure 4 shows the circuit to obtain the expected values:

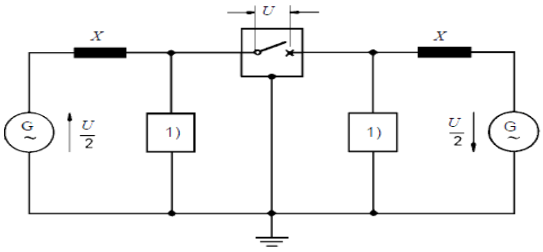

Fig. 4. The circuit used for the test simulation.

In the figure above, a single-phase test circuit is considered, consisting of two equivalent sources located on each side of the circuit breaker, denoted by G.

The elements denoted by X represent the equivalent reactances used for modeling the source-side networks.

The blocks marked 1 represent equivalent combinations of capacitors and resistors used to model the transient recovery voltage circuit.

To obtain the required values for the circuit breaker, the following values have been entered for the circuit elements:

- for a single earth fault: source voltage 9.7 kV with a current of 35 kA, 285 mΩ reactance, 2.14 transformer ratio, and to model the transient recovery voltage, a capacitance of 0.25 µF with a resistance of 50 Ω;
- for the double earth fault, the same assumed circuit was used, but the source voltage value was changed to 11.2 kV and 44 kA.

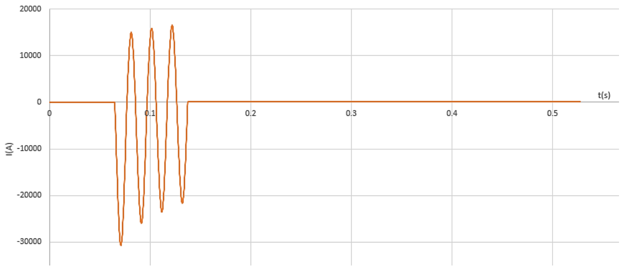

Fig. 5. The shape of the current obtained from the simulation.

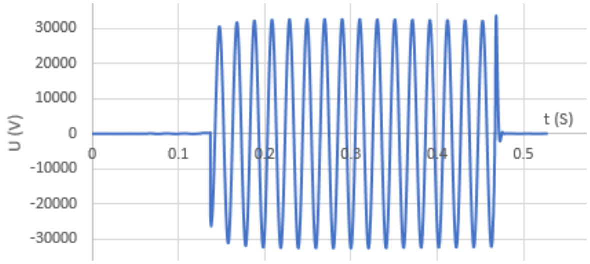

Fig. 6. The shape of the voltage obtained from the simulation.

Numerical simulations (fig.5 and fig. 6) were performed using the dedicated Micro-Cap software to obtain the predicted values for the single and double earth fault tests.

For the sake of simplicity, the arcing time of the circuit breaker was ignored and an opening operation of the switchgear was performed. A peak current of 31 kA was obtained, with an rms value of 14 kA and a voltage of 34 kV for the double earth fault test.

This provides the peak current value required by the test standards.

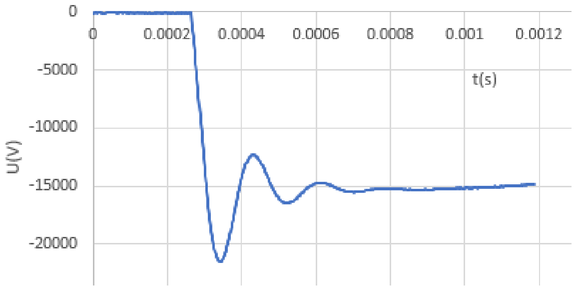

Fig. 7. Transient recovery voltage.

Because the impedance of transformers is generally higher than that of generators, the TRV value is significantly higher. So t_3= 60 µs, and U_C= 28 kV. The TRV values are also required by IEC 62271-100 depending on the rated voltage of the circuit breaker. Figure 7 shows the assumed value for a 12 kV circuit breaker.

V. EXPERIMENTAL RESULTS

A 36 kV, 630 A, 16 kA, 630 A vacuum circuit breaker was used for single and double earth fault tests. The parameters of the single earth fault test were: U=36 kV/$\sqrt{3}kV = 20.9\ kV,\ I = 16kA$ (rated breaking capacity),

$$u_{c,sp} = 1.4\frac{U_n\sqrt{2}}{\sqrt{3}} = 61.4\,(kV);\ t_{3,sp} = \frac{u_{c,sp}}{\frac{u_c}{t_3}} = 109\,(\mu s);$$

The test circuit may be similar to that shown in Fig. 8, depending on laboratory capacity:

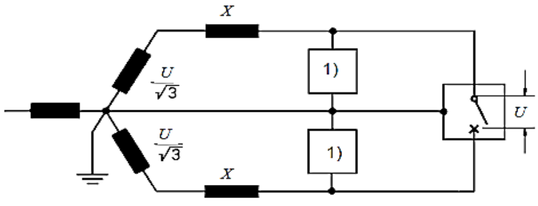

Fig. 8. Test circuit for testing phase opposition using two voltages phase-shifted by 120 electrical degrees ((1) - combinations of capacitors and resistors for TRV modelling).

A single-phase test with a Y_2 connection generator source was selected:

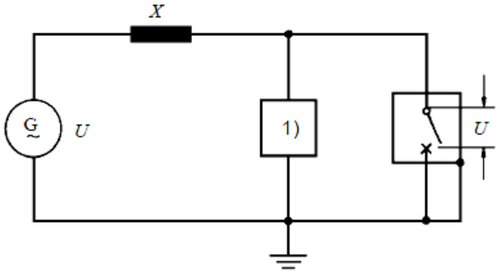

Fig. 9. The circuit used for experimental testing.

The circuit in Fig. 9 is grounded, and the oscillation factor k used in the transient recovery voltage calculations is 1.4. The test sequence consists of a single opening operation of the circuit-breaker, the test being performed on a side pole, thus placing maximum stress on the operating mechanism.

Prior to the single and double earth fault tests, the T100s test was performed to determine the minimum arcing time. This was used in the equation $t_a \geq t_{a\,100s} + 0{,}7\,T/2$, and by adjusting the opening command of the device in relation to the current zero crossing, the maximum arcing time value is obtained.

Figure 10 shows the oscillogram for the single earth fault test. During the test, the following parameters were recorded: circuit breaker control current ($I_{C}\_I_{O}$), recovery voltage (U), transient recovery voltage, short-circuit current (I), reference source voltage (U_G), contact stroke on the stroke sensor, time base (s).

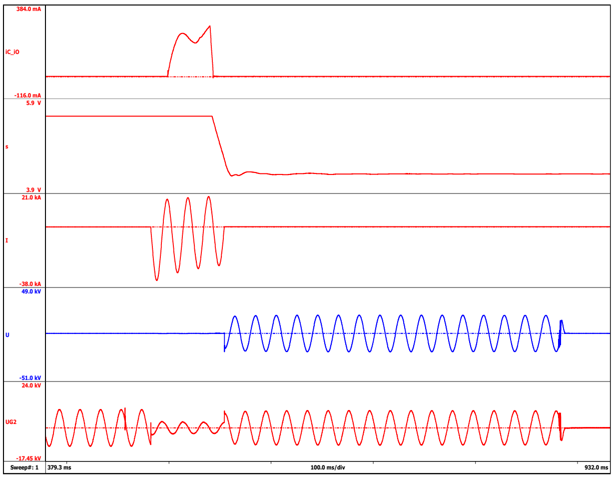

Fig. 10. Oscillogram obtained during the single earth fault test.

Values obtained: peak current value 34 kA; rms current value 16.1 kA; rms voltage value $36/\sqrt{3}$ kV.

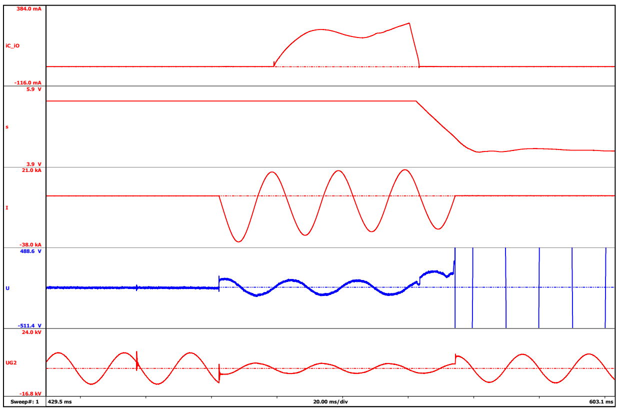

Fig. 11. Oscillogram obtained during the single earth fault test - details.

Figure 11 shows the same oscillogram, but zoomed in on the current sine wave to show the value of the 10.8 ms arc time.

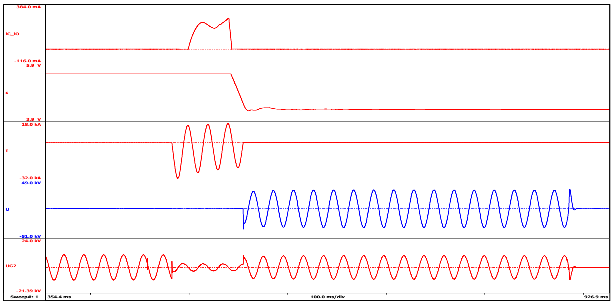

Fig. 12. Oscillogram obtained during the double earth fault test.

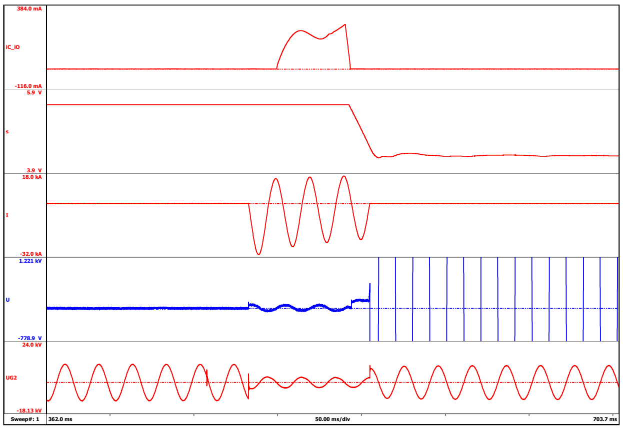

Fig. 13. Oscillogram obtained during the double earth fault test – details.

In the double earth fault test, a current of 30.7 kA peak, 14.1 kA rms and a voltage of 22.7 kV were obtained. Caption of the oscillogram: IC_IO shows the control current through the circuit-breaker's closing or opening coil, recorded by means of a shunt; s - the curve of the motion sensor of the circuit-breaker's moving contacts.

To measure the arcing time, the level previously measured on the motion sensor at the moment of contact separation during no-load operation and at the moment of arc extinction (current passing through zero) and recovery of the industrial frequency voltage are taken into account. In this experiment, an arcing time value of 10.7 ms was obtained. The time measured between the occurrence of the opening command and the moment of contact separation is 44.7 ms, resulting in a total current interruption time of 55.4 ms.

VI. CONCLUSIONS

This article presents the most unfavourable situations encountered in the operation of circuit-breakers in the case of single and double earth faults. The case encountered in substations where the connection between the generator and the associated step-up transformer is made through generator bus bars (IPB) is studied and the current equation for the side interrupting pole is expressed.

The test results confirm the predicted values for voltage, current and transient recovery voltage.

The worst case is a double earth fault under phase opposition conditions. Further tests will be carried out to verify this, but it is estimated that under normal operating conditions (0°<φ<30°) the current at the last breaking pole should not exceed the short-circuit current of the generator.

Tests will be carried out on the test circuit shown in Figure 8 and it is expected that the magnitude will increase under phase opposition conditions (by a factor of $2/\sqrt{3}$ at an angle of 120°).

ACKNOWLEDGMENT

The paper was developed with funding from the Ministry of Research, Innovation and Digitisation - Romania through the NUCLEU PN 23 33 02 01 programme.

Contribution of authors:
First author – 30%;
First coauthor – 20%;
Second coauthor – 20%;
Third coauthor – 15%;
Fourth coauthor – 15%.

Received on September 14, 2025
Editorial Approval on December 3, 2025

REFERENCES

[1] IEC 62271-100, *High-voltage switchgear and controlgear – Part 100: Alternating-current circuit-breakers, International Electrotechnical Commission*, Geneva, Switzerland, 2017.

[2] IEC 62264-1, *Enterprise-control system integration – Part 1: Models and terminology*, International Electrotechnical Commission, Geneva, Switzerland, 2003.

[3] A. Greenwood - *Electrical Transients in Power Systems*, 2nd ed. New York, USA: Wiley, 1991.

[4] D. Braun – "New aspects for neutral grounding of generators considering intermittent faults, presented at the CIDEL", Buenos Aires, Argentina, Sept. 27–29, 2010.

[5] M. Palazzo, D. Braun, and M. Delfanti, "Investigation on the Occurrence of Delayed Current Zeros Phenomena in Power Stations and Related Stress Imposed on Generator Circuit-Breakers," *Proceedings of the International Conference on Power Systems Transients (IPST)*, Delft, Netherlands, June 14-17, 2011.

[6] IEEE Std C37.06-2018, *Standard for AC High-Voltage Circuit Breakers Rated on a Symmetrical Current Basis*, IEEE, 2018.

[7] IEC 60076-25, *Power transformers – Part 25: Neutral grounding resistors*, International Electrotechnical Commission, Geneva, Switzerland, 2023.

[8] J. Ruan, H. Zhang, and X. Li, "Fault Identification of High Voltage Circuit Breaker Trip by Correlating Vibration and Current Signal," *IET Generation, Transmission & Distribution*, vol. 17, no. 5, pp. 1123–1132, 2023, doi: 10.1049/gtd2.12892.

[9] Y. Chen, "Circuit Breaker Fault Diagnosis Method Based on Coil Current Signal Phase Space Reconstruction," *Processes*, vol. 11, no. 4, Art. no. 1241, 2023, doi: 10.3390/pr11041241.

[10] S. Wang, L. Zhou, and F. Liu, "Research on Fault Identification of High Voltage Circuit Breakers Based on Voiceprint Information Data," *Journal of Electrical Engineering & Technology*, vol. 19, no. 4, pp. 1351–1360, 2024, doi: 10.1038/s41598-024-59999-0.

[11] R. P. P. Smeets and N. A. Belda, "High-voltage direct current fault current interruption: A technology review," High Voltage, vol. 6, no. 3, pp. 171–192, Dec. 2020, doi: 10.1049/hve2.12063.

[12] Schweitzer Engineering Laboratories, Inc., "Review of Ground Fault Protection Methods for Grounded, Ungrounded, and Compensated Distribution Systems," Pullman, WA, USA, 2000.

DOI: 10.52846/AUCEE.2025.03

Efficient Solution of PV System with Solar Tracker – Laboratory Prototype

Cosmin-Ionuț Toma*, Denisa Rușinaru*, Mihăiță Lincă*, Cosmin-Gabriel Buzatu* and Cristian Bratu*
*University of Craiova/Faculty of Electrical Engineering, Craiova, Romania, ctoma@em.ucv.ro,
ORCID: 0009-0008-3965-3857
*University of Craiova/Faculty of Electrical Engineering, Craiova, Romania, denisa.rusinaru@incesa.ro,
ORCID: 0000-0003-2340-9143
*University of Craiova/Faculty of Electrical Engineering, Craiova, Romania, mlinca@em.ucv.ro,
ORCID: 0009-0009-7727-3684
*University of Craiova/Faculty of Electrical Engineering, Craiova, Romania, cosmin.buzatu@incesa.ro,
ORCID: 0009-0008-2099-4336
*University of Craiova/Faculty of Electrical Engineering, Craiova, Romania, cristian_bratu_elth@yahoo.com,
ORCID: 0009-0004-9655-4944

Abstract - **Despite its inexhaustible nature, the use of solar energy is temporally limited. In addition, the efficiency of fixed photovoltaic panels is influenced by climatic conditions over a day, resulting in lower efficiency of energy production (about 15%). To operate close to the maximum production point, the photovoltaic panels must be kept perpendicularly to the solar radiation. Therefore, there is a need for solutions to improve the energy efficiency of the PV solar panel and a solar tracker system could be a solution. The paper presents the features of a bi-axial solar tracking system developed by the authors in the laboratory and based on an Arduino Uno microcontroller platform. A small solar panel is oriented in the direction corresponding to the maximum energy point by means of two servomotors controlled by the microcontroller platform, which receives the information from a system of 4 photodetectors.**

Cuvinte cheie: *microcontroller, panou solar, fotorezistor, sistem de monitorizare.*

Keywords: *microcontroller, PV panel, photoresistor, tracking system.*

I. INTRODUCTION

The solar energy is an alternative energy source, clean, easily accessible and inexhaustible.

In order to develop a solar energy conversion system, it is necessary to know the available potential of the solar energy in the country, data provided by literature or specialized sites. Information on solar radiation is available for two cases of atmospheric transparency: clear sky conditions (nebulosity 0-3 degrees), which characterizes the maximum possible sun radiation, as well as medium nebulous conditions [1-3].

Sunshine duration is the time interval of a day when the sun shines and is expressed in hours and tenths of an hour. In Romania, according to data provided by the National Meteorological Administration NMA, the highest values, over 2300 hours per year, are recorded in the south-east of the country, on the Black Sea coast, due to the clear weather in the most part of the year and the downstream airflow at the seaside. Plain regions are distinguished by a characteristic duration of sunshine generated by the air mass circulation conditions. Thus, in the Romanian Plain, the average annual sunshine sums over 2100 hours in the eastern and south-east and over 2200 hours in the central and western parts, predominantly the continental air. In the Western Plain, it varies between 2047 hours and 2178 hours, under the influence of the oceanic circulation from the West. In the case of the high mountain ridge regions, the annual duration exceeds 2000 hours. In hilly and mountainous regions, mist and heavier skies have a higher incidence, the average annual sunshine hours are between 1900 hours in hill and plateau areas and 1,600 hours at altitudes higher than 2500 m. In the intermountain depressions, the duration of the insolation is greatly reduced due to the obstacles that limit the horizon, as well as the persistence of the fog and stratiform nebulosity due to the predominant thermal inversions [4-6].

In order to design a solar energy conversion installation, it is necessary to know the possible solar radiation on the collector surface of either the solar collector or the photovoltaic module. In addition, the solar radiation is a variable function depending on: site position, season, day, day's hour, degree of nebulosity, dust, water vapor and aerosol content in the atmosphere. The prediction of these parameters is based on systematic historical measurements available in NMA publications. In order to maximize the solar energy extraction process and to increase the efficiency of the photovoltaic system, the solar collector plane should be normal to the incident radiation. The diurnal and seasonal motion of the Earth affects the intensity of the radiation received by the solar collector. A sun tracking device allows the solar collector to move in order to track the solar trajectories and maintain its orientation at an optimal angle of inclination, thus leading to increased energy output [7,8].

This paper presents the features of an automatic prototype system with bi-axial tracking (azimuth angle and altitude angle) of solar radiation captured by a small-size photovoltaic panel. The system was designed, programmed and developed by the authors in the laboratory, being driven with a servomotor controlled by a platform with Arduino microcontroller, which accesses the control data from photodetectors - photoresistors (LDRs).

II. THE SOLAR TRACKING SYSTEM'S TECHNOLOGY

A solar tracker allows the sunlight orientation of photovoltaic panels, reflectors, lenses, or other optical devices.

For the photovoltaic panels (PV) applications, the trackers are used to minimize the angle of incidence of solar radiation with the panel. This allows for increasing the amount of energy by comparison with that produced by a fixed power generation unit.

The solar beam has two components: the "direct beam" carrying about 90% of the solar energy and the "diffuse skylight" carrying the rest - the diffuse fraction increases proportionally on cloudy days. Since most of the energy is contained in the direct beam, maximum reception requires the sun to be as much as possible in the panel's exposure area. Using a bi-axial solar tracker is extremely beneficial, following the azimuth and altitude. The bi-axial tracking device is following the nearly permanent perpendicular orientation of the sunlight on the controlled panel, resulting in a net superior performance over the fixed or with limited freedom degrees solar panels [9].

There are four main types of solar energy tracking technologies:

- solar tracker based on photodetectors, achieved with light dependent resistors (LDRs) [3];
- the astronomical method, using a historical pattern of annual sunshine radiation [4];
- a digital camera tracker that uses the processed digital images of the sun [5];
- tracker with hill-climbing algorithm, which uses an iterative algorithm to obtain the maximum power point [6].

The prototype system developed by the authors includes a solar tracker that operates on the basis of information gathered by light-dependent resistors LDRs.

A photoresistor is a passive device whose resistance changes under the influence of a luminous flux. It is based on the phenomenon of photoconductivity by which, the electrons released under the action of light radiation increase the electrical conductivity of the semiconductor and implicitly decrease the resistance of the resistor. This property is used to locate the sun's position. In LDR-based solar tracking systems, three or more sensors are arranged in different ways to locate the sun's position. The method used by the prototype tracker uses shadow formation by changing the position of the sun to locate its current position with 4 LDR sensors. They are located one in the immediate vicinity of the other, being separated from dark areas (partitions) with an LDR sensor in each area. The data achieved from different LDR’s are compared to determine relative radiation and therefore to find the sun's position relative to the panel. This data are provided to an Arduino microcontroller platform, which calculates the difference and controls two actuators to align the panel. This method of tracking the sun is cheap and relatively simple. Photoresistors tracking tools have a position control system that periodically checks the current position of the panel.

Nevertheless, this method has the disadvantage of lower precision for the weather with cloudy sky or fog. The system tends to enter in a stand-by mode, which leads to substantial energy consumption [7].

III. THE CONFIGURATION AND COMPONENTS OF THE SOLAR TRACKER SYSTEM

A. *Characteristics of Component Parts*

The tracking system includes in principle two subsystems: the mechanical subsystem and the electrical one, with the block diagram shown in Fig.1.

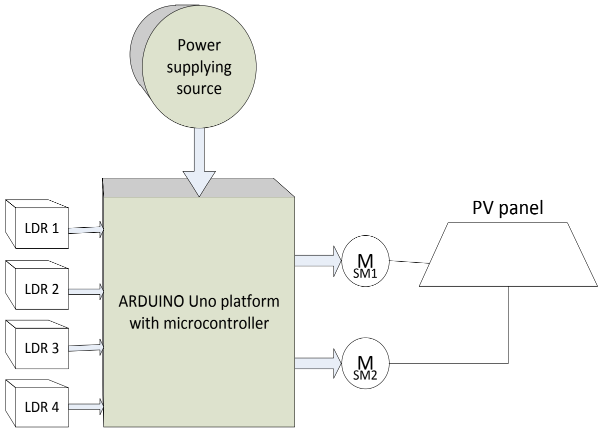

Fig. 1. Block diagram of the solar tracker system

The mechanical subsystem is represented by the metal structure supporting the PV panel and allowing it to rotate with 180^0 around the vertical axis and 90^0 around the horizontal axis.

The electrical subsystem consists of:

i) Arduino Uno platform control module with ATmega328P microcontroller [8];

ii) powering module with battery type 9V or HUAWEI 100-input 240 V AC, 50 Hz, 0.5 A, 12 VDC output, 1.5 A;

iii) data acquisition module with 4 Token photoresistors, 150 V cc, 100 mW, 30 ... 90 kΩ resistance to 10 lx;

iv) 2 controlled actuators for solar panel positioning, type FS5109M, with following characteristics: supply voltage 4.8 ... 6 V; speed 0.16 sec / 60 degrees at 6V, 0.18 sec / 60 degrees to 4.8V; torque 10.2 kgf x cm at 6V, 9 kgf x cm at 4.8 V; rotation angle 1800 counterclockwise; weight 56 g.

The system controls a PV mini panel of 30 x 25 cm^2, 4 x modules (6x12 cells), with a surface of 0.075 m^2 and an efficiency of 12% yield. It works only in the presence of the sunlight.

LDRs detect the intensity of light incident to the solar panel and send sequentially information to the Arduino microcontroller that controls the powering of the two servomotors. The actuators’ control is performed according to the algorithm implemented on the Arduino platform. This one will move the solar panel toward the LDR whose resistance will be lower, that is the one on which the light beam falls so that the panel will continue to follow the light.

If two neighboring LDR units are subject to equal light radiation, then the connected servomotor will not be actuated. This one will attempt to move the solar panel to the position where both LDRs will have the same resistance (when exposed to the same light radiation) and will rotate only if the resistance of one of LDRs will decrease (according to higher sun radiation) [10-13].

B. *System Architecture*

Execution of the control algorithms for actuating the positioning servomotors of the PV mini-panel's support structure is performed in accordance with the wiring diagram included in the solar tracker are detailed in Fig.2 and architecture shown in Fig.3.

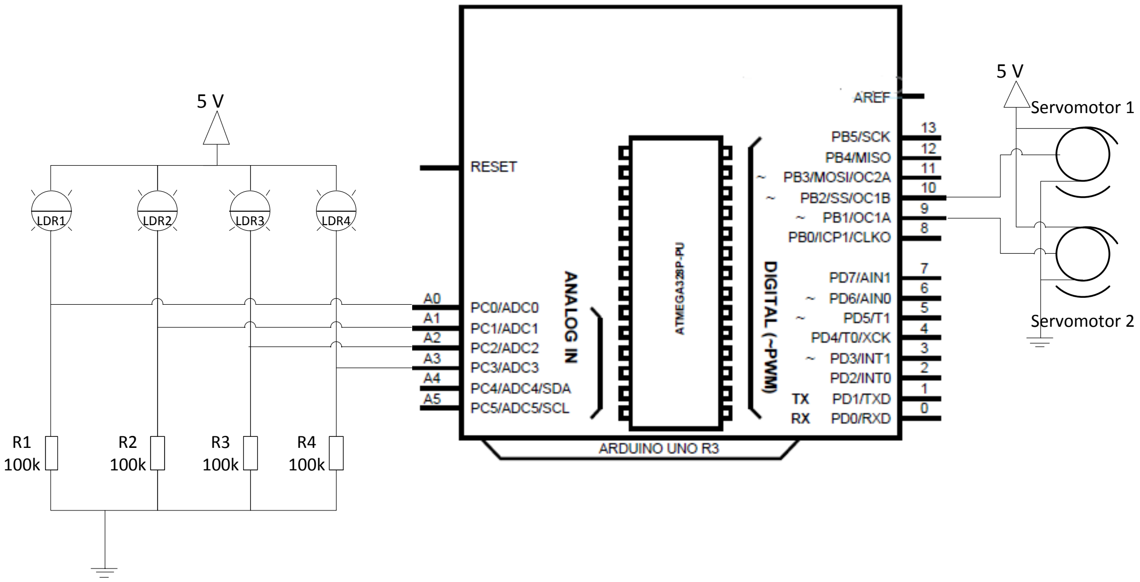

Fig. 2. Connection of the control subsystem components to the microcontroller platform

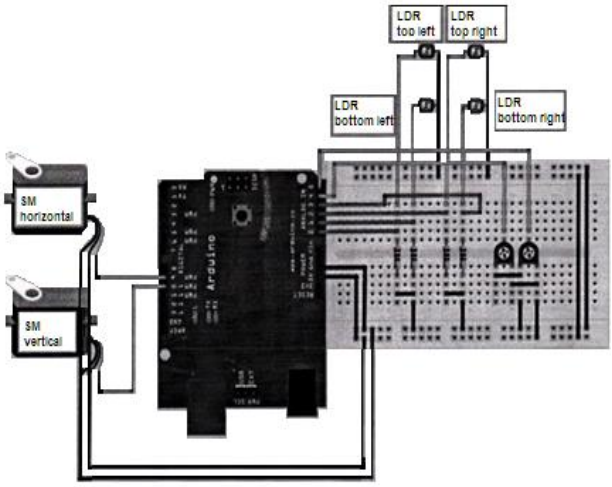

Fig. 3. Picture of base plate subsystem control with Arduino Uno platform

The connections of the servomotors to Arduino are accordingly to Fig. 3, the following:

- positive servomotor pin to microcontroller's + 5V pin;
- servomotor's negative terminal to GND pin of microcontroller;
- the signal cable of the actuators connected to the microcontroller's digital pin 9 (horizontal actuating), respectively 10 (vertical actuating).

The connection of photoresistors to Arduino is achieved as:

- terminal 1 of photoresistor 1, 2, 3, respectively 4 to pin A0, respectively A1, A2, A3 of microcontroller;
- terminal 2 of photoresistor 1, 2, 3, respectively 4 to pin + 5V of microcontroller.

IV. ANALYSIS OF THE SOLAR TRACKER SYSTEM PERFORMANCES

A. *Test Conditions*

The solar tracker prototype system shown in Fig.4 has been tested under real conditions for different daytime and atmospheric conditions.

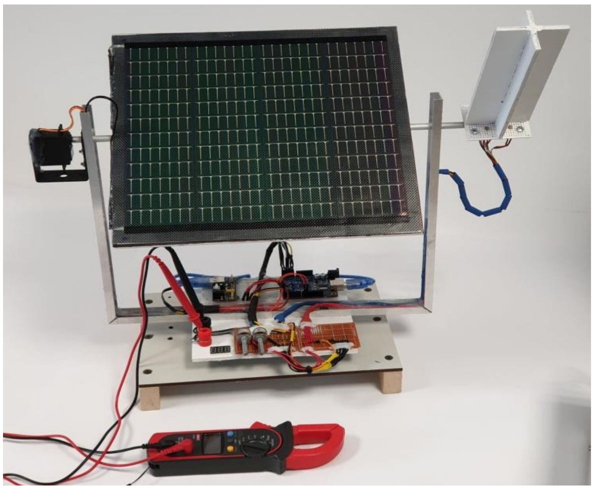

Fig. 4. Bi-axial solar tracker system controlled with Arduino platform and LDR photoresistors - laboratory prototype

The test site is located on the INCESA Applied Science Research Infrastructure building of the University of Craiova, at a height of 20 m. The geographic coordinates of the location are 44.3302 ° N x 23.7949 ° E.

According to NASA application Power Data Access Viewer [6], the annual solar radiation at the terrestrial surface, available at the location with indicated coordinates, has registered a value of approximately 1347 kWh / m^2 year during the past year (01.01.2024-01.01.2025), as in Fig.5.

The application also allows computing the maximum power value produced by the controlled PV panel of 8W power and 12% efficiency under climatic and environmental conditions specific to the considered location [7].

As it can be seen in Fig. 6, for annual solar radiation of 1347 kWh / m^2, a maximum power of about 9 kWp can be estimated to be delivered by the actuated PV panel.

B. *Testing the Performances of the PV System with Solar Tracker*

Determining the performance of the PV power system oriented with a solar tracker requires the determination of the characteristic electrical values for different PV panel orientations, given by the panel’s tilt angle and the rotation of its support frame.

The PV’s panel position controlled by the solar tracker's electrical subsystem is depending on the available sun radiation at that time for the chosen location.

The results of successive readings of the operation electrical values associated with different light conditions and correspondent positions of the mechanical structure are given in Table I.

Experimental testing of the solar panel tracking system has led to the extraction of important observations that allow comparison of the performance of the tracked solar panels with those of the similar fixed panels.

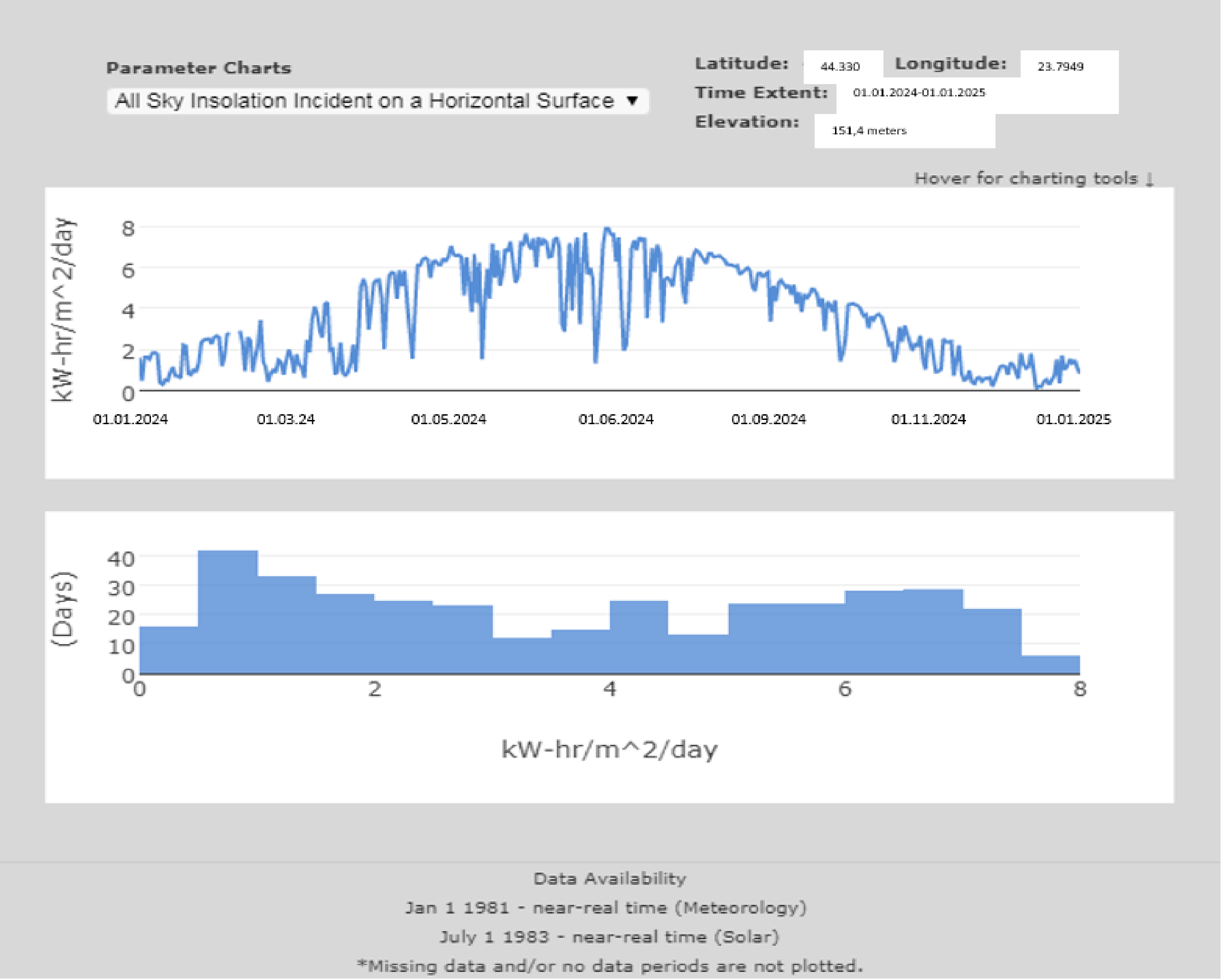

Parameter Charts

All Sky Insolation Incident on a Horizontal Surface ▼

Latitude: 44.330 **Longitude:** 23.7949

Time Extent: 01.01.2024-01.01.2025

Elevation: 151,4 meters

Data Availability

Jan 1 1981 - near-real time (Meteorology)

July 1 1983 - near-real time (Solar)

*Missing data and/or no data periods are not plotted.

Fig. 5. Annual solar radiation at ground level of approx. 1347 kWh / m^2.year - 44.3302 ° N (lat) x 23.7949 ° E (long), 01.01.2024-01.01.2025) (NASA Forecast of Worldwide Energy Resource POWER Higher Resolution Daily Time Series 1/2 x 1 / 2 degree, Climatology Resource for SSE-Renewable Energy)

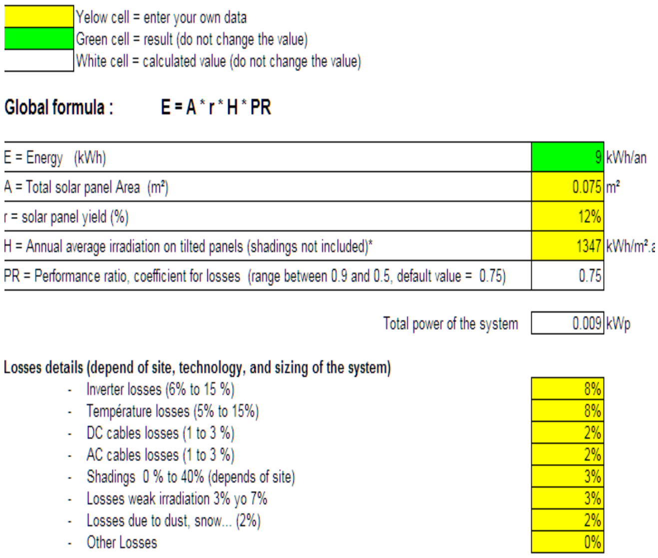

🟨 Yelow cell = enter your own data
🟩 Green cell = result (do not change the value)
☐ White cell = calculated value (do not change the value)

Global formula : **E = A * r * H * PR**

E = Energy (kWh)	9	kWh/an
A = Total solar panel Area (m²)	0.075	m²
r = solar panel yield (%)	12%	
H = Annual average irradiation on tilted panels (shadings not included)*	1347	kWh/m².a
PR = Performance ratio, coefficient for losses (range between 0.9 and 0.5, default value = 0.75)	0.75	

Total power of the system 0.009 kWp

Losses details (depend of site, technology, and sizing of the system)

- Inverter losses (6% to 15 %)	8%
- Température losses (5% to 15%)	8%
- DC cables losses (1 to 3 %)	2%
- AC cables losses (1 to 3 %)	2%
- Shadings 0 % to 40% (depends of site)	3%
- Losses weak irradiation 3% yo 7%	3%
- Losses due to dust, snow... (2%)	2%
- Other Losses	0%

Fig. 6. Computing of the power of PV panel injected in the specified location

TABLE I.
OUTPUT ELECTRICAL VALUES OF THE PV MINI-PANEL ACCORDING TO RADIANCE (MAY 2024, 14:00)

PV panel's values		Weather conditions					
		Cloudy		Partly cloudy		Sunny	
		Tracker off	Tracker on	Tracker off	Tracker on	Tracker off	Tracker on
Tilt angle(deg)	Horiz. axis	45^0	50^0	45^0	35^0	45^0	40^0
	Vert. axis	0^0	15^0	0^0	15^0	0^0	15^0
Open circuit voltage *Voc*, (V)		14.200	14.500	18.900	19.020	18.900	19.020
Short circuit current *Isc*, (A)		0.048	0.050	0.180	0.200	0.318	0.340
Maximum power, (W)		0.681	0.725	3.402	3.804	6.010	6.466
Power gain with tracker, (%)			5.986		10.567		7.061

It can be seen that the maximum output power of the panel increases by up to 11% for panel displacements up to (35^0, 15^0) by comparison with the value corresponding to the fixed reference position (45^0, 0^0). Further testing measurements confirm the opportunity of extending the prototype application in order to increase the efficiency of a larger-scale PV installation [14, 15].

V. CONCLUSIONS

The paper presents the characteristics and performance of a prototype bi-axial tracking system of small solar panels, designed, programmed and developed by the authors in the laboratory.

The purpose of the solar tracker is to track the position of the sun for a better efficiency of the solar installations with PV panels, as demonstrated by the experimental results.

System performance can be improved by using smarter and more efficient sensors, as well as individual components with lower power consumption (e.g. servomotors).

These measures would make possible to increase efficiency and reduce the time till the break even.

ACKNOWLEDGMENT

Source of research funding in this article: Research program of the Electrical Engineering Department financed by the University of Craiova.

Contribution of authors:
First author – 20%
First coauthor – 20%
Second coauthor – 20%
Third coauthor – 20%
Fourth coauthor- 20%

Received on September 27,2025
Editorial Approval on December 7, 2025

REFERENCES

[1] G. O. Young, "Synthetic structure of industrial plastics," in *Plastics*, 2nd ed. vol. 3, J. Peters, Ed. New York: McGraw-Hill, 1964, pp. 15–64.

[2] W.-K. Chen, *Linear Networks and Systems*, Belmont, CA: Wadsworth, 1993, pp. 123–135.

[3] H. Poor, *An Introduction to Signal Detection and Estimation*. New York: Springer-Verlag, 1985, ch. 4.

[4] B. Smith, "An approach to graphs of linear forms," unpublished.

[5] E. H. Miller, "A note on reflector arrays," *IEEE Trans. Antennas Propagat.*, to be published.

[6] J. Wang, "Fundamentals of erbium-doped fiber amplifiers arrays," *IEEE J. Quantum Electron.*, submitted for publication.

[7] C. J. Kaufman, Rocky Mountain Research Lab., Boulder, CO, private communication, May 1995.

[8] Y. Yorozu, M. Hirano, K. Oka, and Y. Tagawa, "Electron spectroscopy studies on magneto-optical media and plastic substrate interfaces," *IEEE Transl. J. Magn.Jpn.*, vol. 2, Aug. 1987, pp. 740–741 [*Dig. 9th Annu. Conf. Magnetics* Japan, 1982, p. 301], doi: 10.1109/TJMJ.1987.4549593.

[9] M. Young, *The Techincal Writers Handbook.* Mill Valley, CA: University Science, 1989.

[10] V. Fedenko and B. Dzundza, "Application of solar tracking systems for enhancing the energy yield of photovoltaic modules: a review," *Technology and Design in Electronic Equipment*, vol. 1–2, pp. 27–35, 2025, doi: 10.15222/TKEA2025.1-2.27.

[11] S. S. Jaafar, H. A. Maarof, H. B. Hamasalh, and K. M. Ahmed, "Comparative performance evaluation of dual-axis solar trackers: Enhancing solar harvesting efficiency," *Journal of Mechatronics, Electrical Power, and Vehicular Technology*, vol. 15, no. 2, pp. 23–31, 2024, doi: 10.55981/j.mev.2024.808.

[12] S. Chen, B. Mulgrew, and P. M. Grant, "A clustering technique for digital communications channel equalization using radial basis function networks," *IEEE Trans. Neural Networks*, vol. 4, pp. 570–578, July 1993, doi: 10.1109/72.238312.

[13] R. W. Lucky, "Automatic equalization for digital communication," *Bell Syst. Tech. J.*, vol. 44, no. 4, pp. 547–588, Apr. 1965. doi: 10.1002/j.1538-7305.1965.tb01678.x.

[14] S. P. Bingulac, "On the compatibility of adaptive controllers," in *Proc. 4th Annu. Allerton Conf. Circuits and Systems Theory*, New York, 1994, pp. 8–16.

[15] G. R. Faulhaber, "Design of service systems with priority reservation," in *Conf. Rec. 1995 IEEE Int. Conf. Communications*, pp. 3–8.

Annals of the University of Craiova, Electrical Engineering series, No. 49, Issue 1, 2025; ISSN 1842-4805 eISSN 2971-9852

DOI: 10.52846/AUCEE.2025.04

A Comparative Analysis of Estimated and Actual Energy Output in Residential Photovoltaic Systems in Craiova, Romania

Ionel-Laurentiu Alboteanu*, Gheorghe Eugen Subtirelu*, Cristian Bratu†, Daniel Cristian Cismaru*
* University of Craiova / Department of Electromechanical, Environmental and Applied Informatics, Craiova, Romania, e-mail: lalboteanu@em.ucv.ro, esubtirelu@em.ucv.ro, dcismaru@gmail.com,
ORCID: 0000-0001-5154-4145; 0000-0001-8559-946X; 0009-0002-4685-5795
† University of Craiova / Department of Electrical, Energy and Aerospace Engineering, Craiova, Romania, e-mail: cbratu@elth.ucv.ro, ORCID: 0009-0004-3142-687X

***Abstract* - Accurate estimation of photovoltaic (PV) energy production is essential for ensuring the optimal design, operation, and economic viability of solar installations. However, discrepancies often arise between predicted and actual energy yields, particularly in regions characterized by variable meteorological conditions. The paper presents a synthesis of methods for estimating energy production of photovoltaic systems. For two types of residential systems located in Craiova, a comparative analysis is presented between the estimated values obtained using the most efficient methods and the actual measured values. The research combines simulation-based predictions with real operational data collected over a defined monitoring period to evaluate the accuracy of commonly used estimation models. To estimate solar radiation and energy production, some of the most common specialized software for renewable energy sources were used. The findings reveal that estimation tools tend to overpredict energy output during periods of high temperature and unstable atmospheric conditions, while performing more accurately during stable seasonal intervals. These results highlight the importance of localized calibration of prediction models and the integration of detailed climatic data for improving accuracy. The study contributes valuable insights for system designers, operators, and policymakers seeking to enhance PV system reliability and advance renewable energy planning in Romania and similar climatic regions.**

Cuvinte-cheie: *sisteme fotovoltaice rezidentiale, energie estimata, energie produsa, radiatie solara.*

Keywords: *residential photovoltaic systems, energy estimation energy production, solar irradiation.*

I. INTRODUCTION

The rapid global expansion of photovoltaic (PV) technologies has intensified the need for accurate methods of estimating energy production in order to ensure efficient system design, economic feasibility, and long-term operational reliability [1]. In this context, comparing estimated energy output with actual measured production is essential for evaluating both the performance of PV installations and the accuracy of the prediction models employed. Such assessments are particularly relevant in regions with variable climatic conditions, where meteorological fluctuations can significantly influence solar energy yields.

Craiova, located in the southwestern part of Romania, represents an area characterized by a temperate-continental climate with distinct seasonal variations. These conditions can lead to notable discrepancies between predicted and real PV energy generation, making the region suitable for case studies aimed at performance evaluation and model validation. Understanding these discrepancies is crucial for improving forecasting methodologies, optimizing system configurations, and enhancing the overall reliability of renewable energy integration into the local grid.

Energy production estimation for PV systems can be conducted through various approaches, depending on the desired level of accuracy, the availability of input data, and the intended application (e.g., system design, performance monitoring, research). Existing literature [2], [3], [4] has addressed this topic extensively, with most studies focusing on the quantification of available solar radiation.

The present paper outlines several specific methods for evaluating the energy production of residential photovoltaic systems located in a specific area [5],[6],[7]. The chosen location is the city of Craiova, Romania. The photovoltaic energy production estimated using these methods is compared with the actual energy generated by residential photovoltaic systems.

A comparative case study is conducted on two residential PV configurations: an off-grid system with panels installed on a flat terrace and a grid-connected system with panels mounted on a pitched roof.

A preliminary version of this study was presented in [5].

II. A COMPARATIVE ANALISYS OF THE METHODS USED TO ESTIMATE THE ENERGY PRODUCED BY PHOTOVOLTAIC SYSTEMS

In the specialized literature, numerous methods exist for estimating the energy output of photovoltaic (PV) systems. Essential factors that must be considered in any estimation method include [8], [9], [10]:

- local solar irradiation – the primary variable
- panel orientation and tilt
- effect of temperature
- losses: cables, inverter, shading, dust, mismatch
- annual panel degradation (0.3–0.8% per year)
- system availability (operating time without interruptions).

A synthesis of the main estimation methods is presented below:

1. First-approximation method

This approach is based on simple theoretical estimates using the equation [5]:

$$E = G \cdot A \cdot \eta \qquad \text{[kWh]} \qquad (1)$$

where:

E-energy produced [kWh]

G-average annual solar irradiation (irradiance) [kWh/m²]

A-PV panels area surface [m²]

η- overall efficiency (panels + inverter + losses).

This method is fast and easy to apply, but does not account for seasonal variations, detailed losses, or specific local conditions.

2. Method based on climatological data and correction factors

This method uses meteorological databases (e.g., Meteonorm, PVGIS) for radiation and temperature, applying specific loss factors such as those caused by temperature, shading, or soiling of the PV modules.

It offers greater accuracy by using real-world data, but requires access to climatic datasets and knowledge of the installation parameters [8], [9].

3. Computer simulation (dedicated software)

Examples of software include PVGIS, PVsyst, PV*SOL, Helio Scope, and SAM (NREL).

These tools model the PV system using actual parameters and hourly meteorological conditions, including 3D shading effects [9], [10].

Such methods are highly accurate and ideal for system sizing and economic analysis, but may require a license, as well as time for detailed modeling.

4. In-situ measurement method

This approach involves radiation and temperature sensors that measure actual production over a short period (e.g., several months), followed by long-term extrapolation [4].

It accurately reflects local conditions, but requires a longer time to obtain estimates and entails additional equipment costs.

5. Statistical method based on similar installations

Historical data from PV systems with comparable characteristics and location are used.

This method is quick and based on real performance results, but depends on the availability of relevant data and the exact similarity of operating conditions.

The above methods are summarized in Table I, and a complexity–accuracy analysis of these methods is illustrated in the chart shown in Figure 1.

The selection of an appropriate method for estimating the energy production of photovoltaic systems depends on the purpose of the analysis and the required level of accuracy. Software simulations are suitable for preliminary assessments and system sizing, whereas on-site measurements provide more precise data, essential for detailed feasibility studies and performance optimization.

A 2024 study [11] shows that PV system performance depends significantly on local climatic conditions (irradiance, temperature, humidity, and losses) and recommends incorporating all these factors into the modelling framework to obtain realistic predictions.

The comparative analysis [12] highlights that the choice of the irradiance database (satellite products, reanalysis data, or ground measurements) strongly influences production estimates — differences between datasets can lead to substantial variations in the predicted annual energy yield.

Recent research [13] emphasizes that software-based simulation methods — integrating irradiance, module temperature, losses, and degradation — provide the most robust production estimates, particularly when input parameters are well characterized.

For short-term forecasting (hours to days), hybrid approaches that combine physical models, automatically bias-corrected climatological data, and machine-learning/statistical techniques tend to reduce errors compared to simple baseline methods [14].

TABLE I.
COMPARATIVE TABLE OF METHODS FOR ESTIMATING THE ENERGY OUTPUT OF PHOTOVOLTAIC SYSTEMS

Method	**Principle**	**Required Data**	**Deviation**	**Advantages**	**Disadvantages**	**Example Applications**
Simple Theoretical Estimation	Calculates energy based on average solar radiation and overall efficiency	Average annual irradiation, panel surface area, overall efficiency	±20–30%	Fast, easy to apply, does not require software	Does not account for seasonal variations, detailed losses, or local conditions	Preliminary estimates, concept-stage projects
Climatological Data + Correction Factors	Uses tilted-plane irradiation and associated loss factors	Monthly/hourly meteorological data, technical parameters of the system	±10–15%	Relatively accurate, accounts for real losses	Requires reliable local data	Technical and economic feasibility studies
Software Simulation	Models the system using actual parameters and hourly conditions	Detailed meteorological data, panel and inverter specifications, site geometry	±5–10%	Highly accurate, includes shading, orientation, and degradation	Requires software and modeling time	Professional projects, tenders, investment analysis

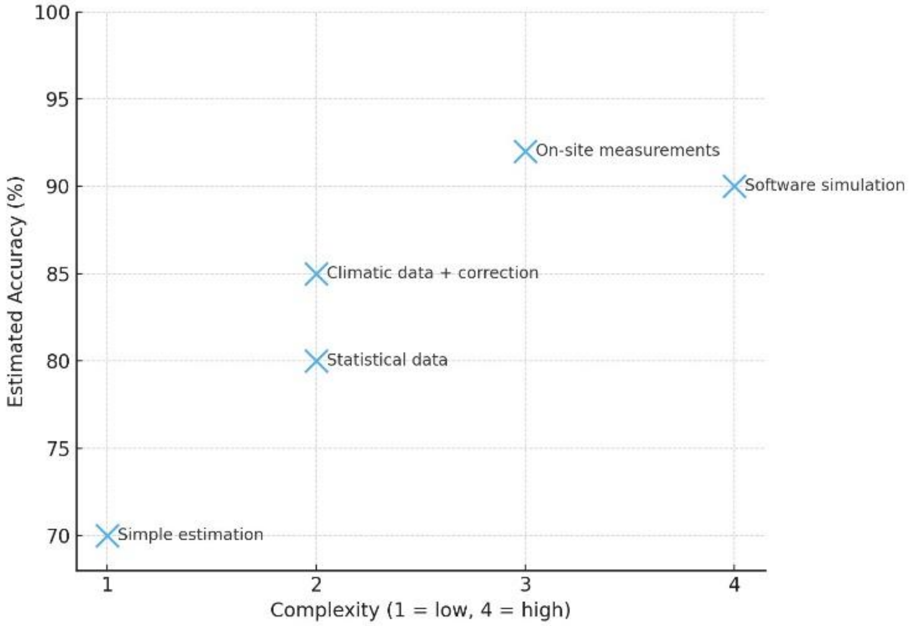

Fig. 1. PV energy production estimation methods. Complexity versus accuracy

The accuracy of PV energy yield estimation is most commonly determined by comparing the estimated output with the measured production and quantifying the deviation. For instance, in the case of a simple theoretical estimation method, a 30% deviation corresponds to an estimated accuracy of approximately 70%. According to the chart in Figure 1, it can be observed that, in terms of complexity and accuracy, methods based on dedicated simulation software and those employing on-site measurements are the most suitable.

Therefore, in the case study presented in this paper, these methods will be applied.

III. IMPLEMENTATION OF ENERGY YIELD ESTIMATION METHODS FOR PHOTOVOLTAIC SYSTEMS LOCATED IN CRAIOVA

The case study analyzes the energy production of two types of residential photovoltaic systems located in Craiova, Romania. The first photovoltaic system is an off-grid type with PV panels mounted on a terrace, while the second system is an on-grid type with PV panels mounted on a pitched roof.

A. *Off Grid Photovoltaic System*

The off-grid photovoltaic system (Figure 2) has the following characteristics:

- PV capacity: 3 kWp

- PV module type: 12 polycrystalline silicon PV modules, model Conergy 245P

- total module area: 20 m²

- PV module efficiency: 15.6%

Because solar radiation is the most important parameter for estimating the energy production of photovoltaic systems, in the first part a comparative analysis is made between the estimated and the real, measured solar radiation.

To estimate the solar irradiation and the energy production, the PVGIS24 software was used.

The PVGIS software, through the GIS component, provides information about the geolocation of the analyzed photovoltaic system as seen in Figure 2.

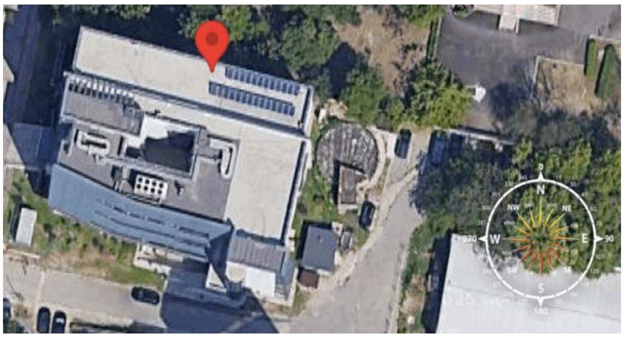

Fig. 2. Geolocation of photovoltaic system

PVGIS24 is a modernized version featuring an advanced interface, geolocation through Google Maps, and complex simulations with multiple inclinations and orientations. It includes intuitive charts, CSV/JSON export options, and an analysis of natural terrain shading; however, it does not account for artificial obstacles such as trees or buildings.

Key Features of the PVGIS24 Software:

• Estimation of annual energy production (kWh), equivalent full-load hours at nominal power (kWh/kWp), monthly distribution, and graphical tools to support optimization.

• Data export capabilities in CSV, JSON, or PDF formats.

• Integrated Financial Simulator that enables the assessment of self-consumption, cost savings, and return on investment (ROI) by incorporating information on energy consumption, costs, subsidies, and other parameters.

- High flexibility, making it suitable for both basic users and professionals (households, institutions, consultants, etc.).
- High accuracy, based on satellite-derived datasets and climate reanalysis.
- Terrain shading analysis, particularly relevant in mountainous regions or densely built urban areas.

The simulation results are presented in Figure 3. In estimating solar irradiation and energy production using the PVGIS software, in addition to the technical characteristics of the photovoltaic system, other real operating conditions were also considered, such as the positioning of the PV panels, the tilt angle, and related parameters.

Measurement of solar irradiation was carried out with the monitoring equipment of a photovoltaic system located in Craiova (Figure 4 and Figure 5).

Weather parameters were monitored online and stored on an SD card.

Data is downloaded in * CSV format that can be easily imported into Excel and then processed in the desired form.

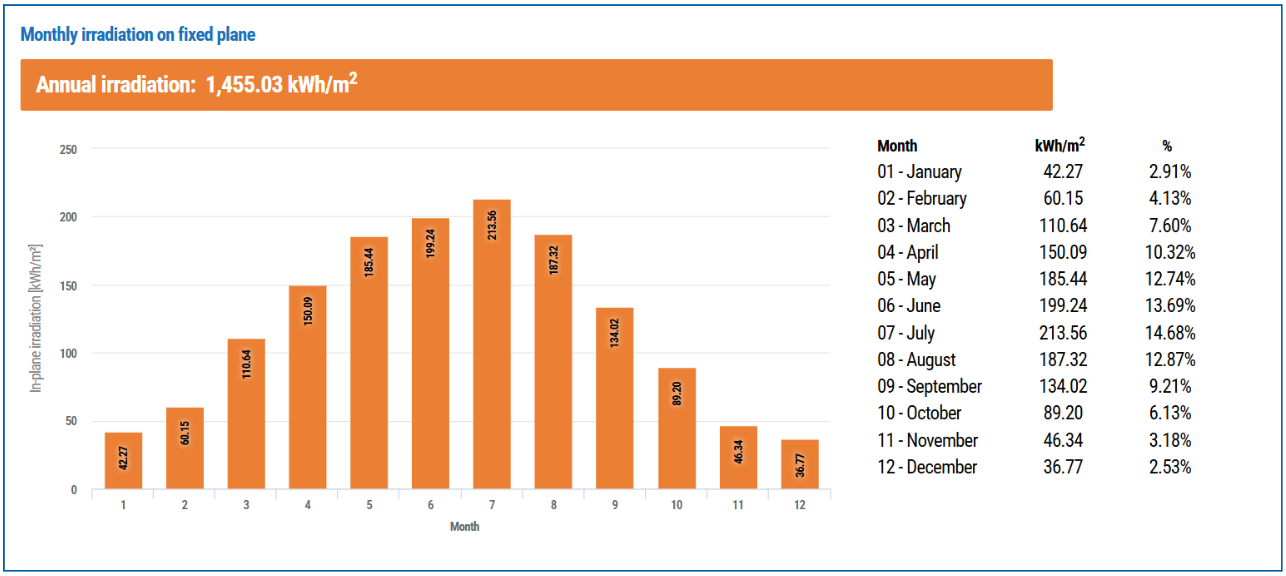

Monthly irradiation on fixed plane

Annual irradiation: 1,455.03 kWh/m^2

Month	kWh/m^2	%
01 - January	42.27	2.91%
02 - February	60.15	4.13%
03 - March	110.64	7.60%
04 - April	150.09	10.32%
05 - May	185.44	12.74%
06 - June	199.24	13.69%
07 - July	213.56	14.68%
08 - August	187.32	12.87%
09 - September	134.02	9.21%
10 - October	89.20	6.13%
11 - November	46.34	3.18%
12 - December	36.77	2.53%

Fig. 3. Monthly irradiation on fixed PV plan – estimated values

Fig. 4. Equipment for measuring weather parameters: 1- pyranometer; 2- anemometer.

SENS0802:38491

Radiation	898	W/m^2
Module temperature	37.3	°C
Ambient temperature	27.6	°C
Wind speed	3.1	m/s
Radiation (external)	0	W/m^2

Fig. 5. Window of monitoring system

The resulting graph of solar radiation monitoring is presented in Figure 6 during the year 2025, up to the present.

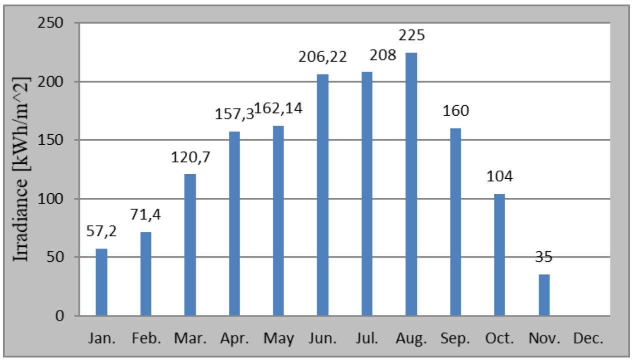

Fig. 6. Monthly irradiation on PV plan measured during the year 2025

To verify the accuracy and performance of the monitoring system's pyranometer, a Skylinx weather station containing a high-precision pyranometer was used.

The used pyranometer to measure the global solar irradiation was Li-200S, manufactured by Li-Cor Inc. Lincoln, Nebraska, US, (City, State if US, Country), with a measurement error ±5%, and with a measurement accuracy comparable to pyranometers of class 1, according to [15]. This pyranometer transmits a current output signal with a sensitivity of 10 µA at 1000 W/m^2.

For the comparative analysis, two days with different levels of solar radiation were taken into account, namely 2025.01.15 and 2025.06.15. The resulting graphs are presented in Figure 7 and Figure 8, respectively.

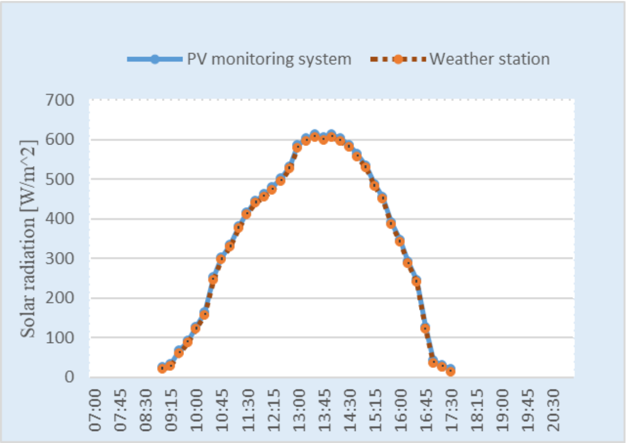

Fig. 7. Chart of global solar irradiation, measured on 2025.01.15

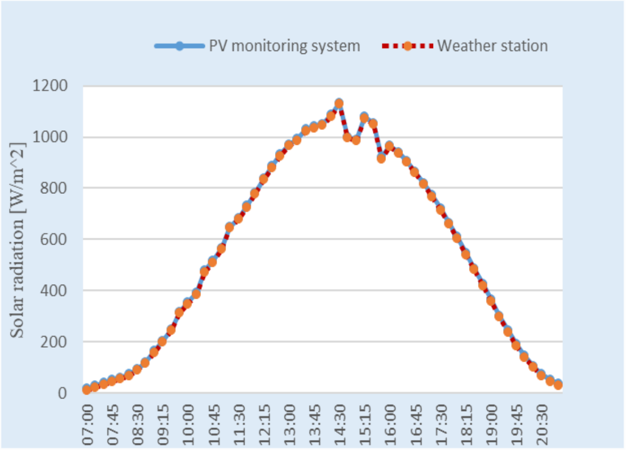

Fig. 8. Chart of global solar irradiation, measured on 2025.06.15

As seen in Figures 7 and 8 the measurements obtained from the two pyranometers show no significant differences

Based on the solar radiation graphs presented in Figures 3 and 6, a comparative analysis was made between the estimated and calculated solar radiation. The numerical values are presented in Table II.

TABLE II
ESTIMATED AND MEASURED SOLAR RADIATION VALUES DURING THE YEAR 2025

Month	Estimated solar radiation [kWh/m^2]	Measured solar radiation [kWh/m^2]	Relative deviation [%]
Jan.	42,27	57,2	26,10
Feb.	60,15	71,4	15,75
Mar.	110,64	120,7	8,33
Apr.	150,09	157,3	4,58
May	185,44	162,14	14,37
Jun.	199,24	206,22	3,38
Jul.	213,56	208	2,67
Aug.	187	225	16,88
Sep.	134	160	16,25
Oct.	89	104	14,42
Nov.	46	35	31,42
Average value	**128,25**	**136,99**	**14,01**

According to the values presented in the table II, there is an average relative deviation between the estimated and measured solar radiation of 14.01 %. It is mentioned that the comparative analysis was made until December 2025, the current moment when the article was elaborated.

Similarly, for the photovoltaic system analyzed using the PVGIS24 software, the estimated energy production graph was generated (Fig. 9).

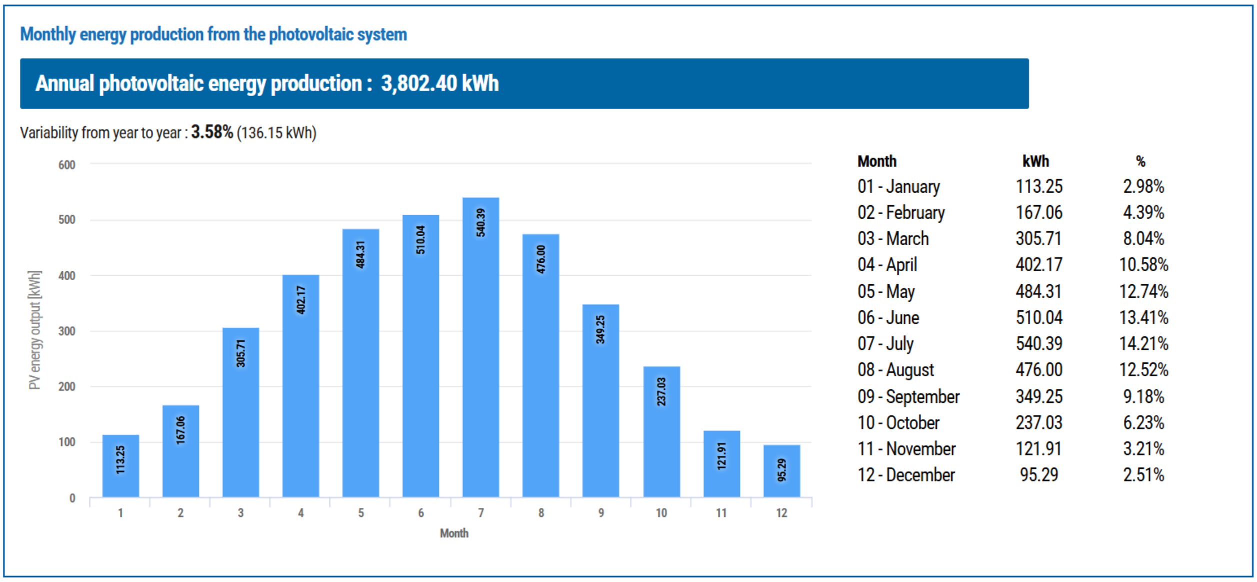
Monthly energy production from the photovoltaic system

Annual photovoltaic energy production : 3,802.40 kWh

Variability from year to year : **3.58%** (136.15 kWh)

Month	kWh	%
01 - January	113.25	2.98%
02 - February	167.06	4.39%
03 - March	305.71	8.04%
04 - April	402.17	10.58%
05 - May	484.31	12.74%
06 - June	510.04	13.41%
07 - July	540.39	14.21%
08 - August	476.00	12.52%
09 - September	349.25	9.18%
10 - October	237.03	6.23%
11 - November	121.91	3.21%
12 - December	95.29	2.51%

Fig. 9. Monthly energy production from the off-grid PV system – estimated values

Over the course of one year, the monthly solar irradiation reaches approximately 1445 kWh/m², whereas the annual energy output of the PV system amounts to 3802 kWh.

To perform a comparative analysis between the estimated photovoltaic energy production and the actual photovoltaic energy production, data provided by the PV system's own monitoring system were used.

The data regarding energy production were processed and presented in a graphical format suitable for comparative analysis (Fig. 10, 11).

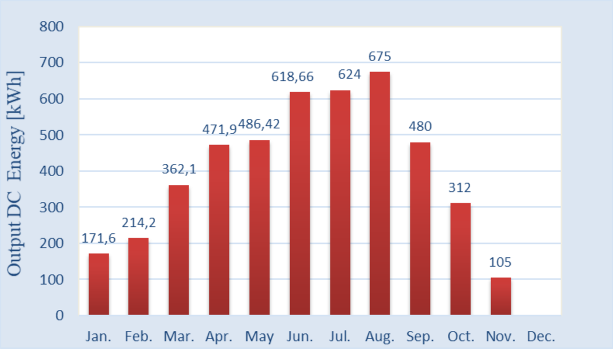

Fig. 10. Monthly DC energy production from the PV system measured during the year 2025

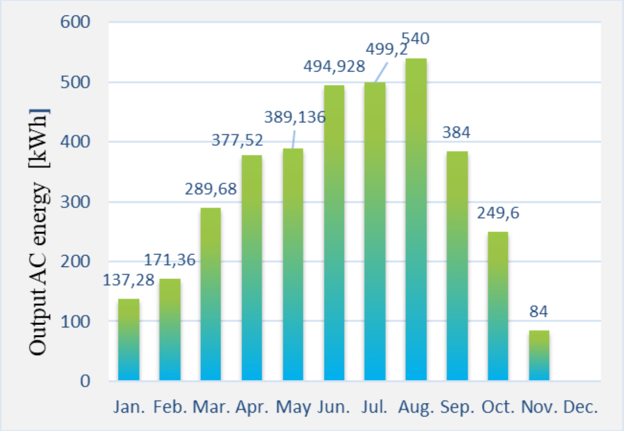

Fig. 11. Monthly AC energy production from the PV system measured during the year 2025

Based on the energy production graphs presented in Figures 9 and 11, a comparative analysis was made between the estimated and calculated output energy. The numerical values are presented in Table III.

TABLE III
ESTIMATED AND MEASURED OUTPUT ENERGY VALUES OF PV SYSTEM DURING THE YEAR 2025

Month	Estimated output energy [kWh]	Measured AC output energy [kWh]	Relative deviation [%]
Jan.	113,25	137,28	17,50
Feb.	167,06	171,36	2,50
Mar.	305,71	289,68	5,53
Apr.	402,17	377,52	6,52
May	484,31	389,136	24,45
Jun.	510,04	494,928	3,05
Jul.	540,3	499,2	8,23
Aug.	476	540	11,85
Sep.	349	384	9,11
Oct.	237	249,6	5,04
Nov.	121	84	44,04
Average value	**336,89**	**328,79**	**12,53**

According to the values presented in the Table III, there is an average relative deviation between the estimated and measured output energy of 12.53%.

In general, the differences between the estimated and measured energy are not significant. The exception is November, because in 2025 it was an atypical month, with few sunny days.

B. *On grid photovoltaic system*

The on-grid connected photovoltaic system (without storage) is installed at a residential house and mainly consists of:

- 16 photovoltaic panels grouped into two strings (PV1 and PV2), each with 8 panels;
- a single-phase HUAWEI SUN2000-6KTL-L1 inverter with a power rating of 6 kW.

The photovoltaic panels are mounted in a fixed position on the south-facing slope (PV1) and the west-facing slope (PV2) of the building's roof. The main technical characteristics of a photovoltaic panel are as follows:

- PV capacity: 7,4 kWp
- type of PV panels: monocrystalline - half-cell PV modules, model Huawei, MF0020, 465 W
- photovoltaic surface area: 35,34 m²
- PV panel efficiency: 21,05%

Fig. 12. Image of the PV panels mounted on the West facade of the roof (PV2 string)

The PV system contains a monitoring software application called Fusion Solar. This is Huawei's inverter software ecosystem for PV system monitoring and management. It includes a mobile application and a web platform/cloud-portal.

The web platform is often called SmartPVMS — Smart PV Management System — and enables the management, monitoring, and maintenance (O&M) of PV plants.

A screenshot of the main application screen is shown in Figure 13.

This image displays the energy produced by the PV system instantly.

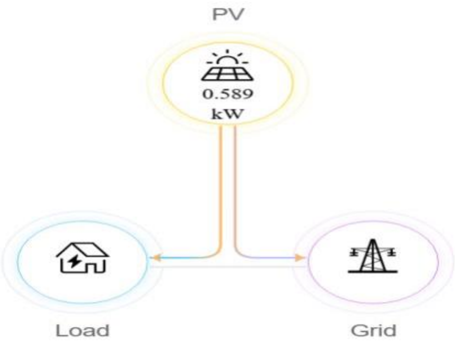

Fig. 13. The main screen of FusionSolar application

Similarly, to the previous example, the estimation of energy production was performed using the PVGIS24 software. The simulation result is illustrated in the graph shown in Figure 14.

By employing the FusionSolar monitoring software associated with the Huawei inverter, the actual energy output of the photovoltaic system was recorded.

The monthly graph of the energy produced throughout the year 2025, up to the present, is presented in Figure 15.

As in the previous case, to make a comparative analysis between the estimated and measured energy, the numerical values were represented in Table IV.

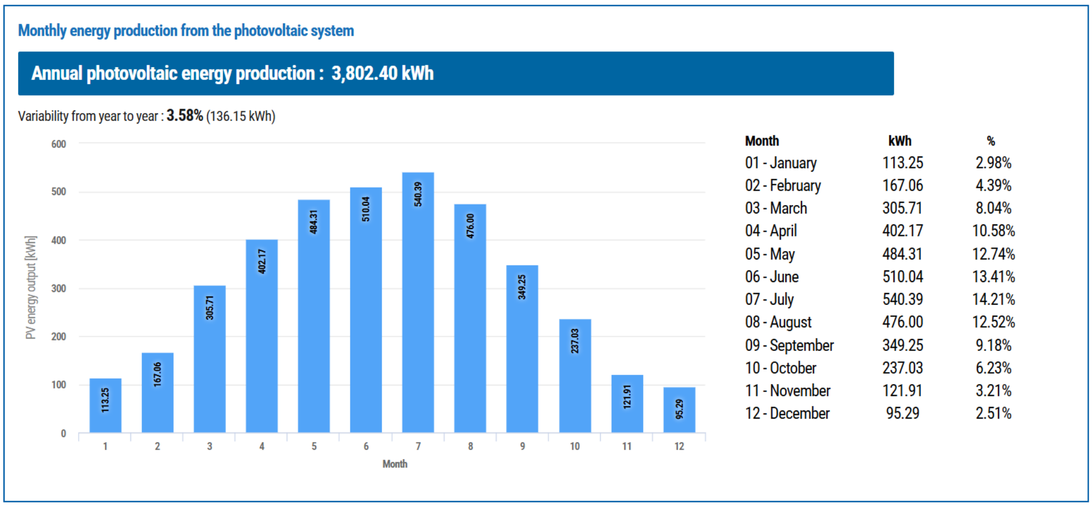

Month	kWh	%
01 - January	113.25	2.98%
02 - February	167.06	4.39%
03 - March	305.71	8.04%
04 - April	402.17	10.58%
05 - May	484.31	12.74%
06 - June	510.04	13.41%
07 - July	540.39	14.21%
08 - August	476.00	12.52%
09 - September	349.25	9.18%
10 - October	237.03	6.23%
11 - November	121.91	3.21%
12 - December	95.29	2.51%

Fig. 14. Monthly energy production from the on-grid PV system - estimated values

Fig. 15. Monthly energy production from the on-grid PV system measured during the year 2025

TABLE IV
ESTIMATED AND MEASURED OUTPUT ENERGY VALUES OF ON GRID PV SYSTEM DURING THE YEAR 2025

Month	Estimated output energy [kWh]	Measured output energy [kWh]	Relative deviation [%]
Jan.	334	405	17,53
Feb.	452	384	17,70
Mar.	758	619	22,45
Apr.	930	880	5,68
May	1059	949	11,59
Jun.	1090	1132	3,71
Jul.	1169	1040	12,40
Aug.	1087	1008	7,83
Sep.	839	763	9,96
Oct.	639	505	26,53
Nov.	358	198	80,80
Average value	**792,27**	**716,63**	**19,65**

According to the data in the table, it can be observed that the difference between the estimated energy and the measured energy is 19.65%, which is approximately 7% higher compared to the previously analyzed off-grid PV system.

IV. DISCUSSIONS

The comparative analysis performed for the two photovoltaic systems highlights several important aspects regarding the accuracy of energy production estimation models under the climatic conditions specific to the Craiova region. In both case studies, the simulation results obtained with the PVGIS24 software show a tendency to overestimate the actual energy output. This effect is consistent with observations reported in the literature, especially for areas characterized by variable atmospheric transparency, periods with increased cloudiness and elevated temperatures during the summer months.

For the off-grid system, the average deviation between estimated and measured energy production is 12.53%. This value indicates a relatively good agreement between the prediction models and real-world operating conditions, with the exception of specific months in which irradiation variability was more pronounced. The November deviation corresponds to an atypical month in terms of solar availability, which confirms the sensitivity of simulation tools to meteorological anomalies not fully captured in historical databases.

The on-grid system exhibits a higher average deviation of 19.65%, approximately 7% above the value obtained for the off-grid system. This difference can be attributed to several technical and environmental factors: 1) the presence of two roof orientations—south and west—which introduces non-uniform irradiation profiles; 2) higher operating temperatures on rooftop-mounted modules, which reduce electrical efficiency; and 3) potential partial shading or local obstacles not considered in the PVGIS terrain-based shading model. Additionally, inverter clipping during periods of high irradiance may contribute to reduced energy yield, especially for the 6 kW inverter operating with a 7.4 kWp installed capacity.

Solar radiation analysis further indicates an average deviation of 14.01% between estimated and measured irradiation. Since irradiation is the primary variable used in PV energy models, this discrepancy directly influences the accuracy of the estimated energy outputs. Therefore, improving the precision of local irradiation data—through the use of in-situ sensors, long-term monitoring, or refined satellite datasets—would significantly enhance predictive accuracy.

Overall, the study confirms that while PVGIS24 provides reliable preliminary estimations, localized calibration and real-time monitoring remain essential for accurate performance assessment, system optimization, and investment decision-making.

V. CONCLUSIONS

This research presents a comparative evaluation of estimated and measured energy production for two residential photovoltaic systems installed in Craiova, Romania. The results demonstrate that simulation tools such as PVGIS24 offer reasonably accurate predictions but tend to overestimate the real energy yield, with deviations ranging between 12% and 20% depending on system configuration and seasonal conditions.

For the off-grid system, the average deviation of 12.53% indicates that the estimation model performs well when the installation is less influenced by complex shading or thermal effects. In contrast, the on-grid rooftop system shows a higher deviation of 19.65%, emphasizing the influence of module orientation, roof mounting temperature effects, and other local factors not fully integrated into the simulation model.

The comparison of estimated and measured solar radiation further reveals an average deviation of 14.01%, suggesting that irradiation data is a major source of uncertainty in predictive simulations. This finding reinforces the importance of continuous on-site monitoring using calibrated pyranometers to improve long-term prediction accuracy.

In conclusion, the study shows that software-based estimation remains a valuable tool for preliminary design, feasibility studies, and performance assessment. However, for detailed analysis and optimization, real operational data and localized calibration are indispensable. Future work may focus on integrating machine-learning-based correction models, extending measurement campaigns, and developing hybrid datasets combining satellite and in-situ information to further enhance prediction accuracy for photovoltaic systems in Romania's variable climatic conditions.

ACKNOWLEDGMENT

Source of research funding in this article: Research program of the Electrical Engineering Department financed by the University of Craiova.

Contribution of authors:
First author – 50%
First coauthor – 20%
Second coauthor – 20%
Third coauthor- 10%

Received on September 25,2025
Editorial Approval on December 4, 2025

REFERENCES

[1] International Energy Agency – Photovoltaic Power Systems Programme (IEA-PVPS). (2022). "Trends in Photovoltaic Applications". Available at: https://iea-pvps.org.

[2] I. L. Alboteanu, C.A. Bulucea, and S. Degeratu, "Estimating solar irradiation absorbed by photovoltaic panels with low concentration located in Craiova, Romania", *Sustainability Journal*, Volume 7, Issue 3, 2015, pp. 2644-2661, doi:10.3390/su7032644.

[3] M. Paulescu and Z. Schlett, *Photovoltaic Conversion of Solar Energy*, Timişoara: Mirton Publishing House, Romania, 2001.

[4] W. Yao, C. Yue, A. Xu, X. Kong , W. Cao, Z. Zheng, Q. Yue, "Power generation evaluation of solar photovoltaic systems using radiation frequency distribution", *Journal of Building Engineering* Vol. 98, 1 December 2024, doi.org/10.1016/j.jobe.2024.110981.

[5] I. L. Alboteanu, G. Manolea, G.E. Subtirelu and C. Bratu, "Residential photovoltaic systems energy production estimation", *2025 International Conference on Electromechanical and Energy Systems (SIELMEN)*, 16-18 October 2025, doi: 10.1109/SIELMEN67352.2025.11260738.

[6] M.A. Green, *Solar Cells: Operating Principles, Technology, and System Applications*, University of New South Wales, 2022.

[7] E. Skoplaki and J.A. Palyvos, "On the temperature dependence of photovoltaic module electrical performance: A review of efficiency power correlations", Solar Energy, 83, 2009, pp. 614–624, doi: 10.1016/j.solener.2008.10.008.

[8] Meteotest. (2023). Meteonorm – Global Meteorological Database for Engineers, Architects, and Education. Available at: https://meteonorm.com.

[9] European Commission, Joint Research Centre (JRC). (2023). PVGIS – Photovoltaic Geographical Information System. Available at: https://joint-research-centre.ec.europa.eu/pvgis.

[10] NREL – National Renewable Energy Laboratory. (2023). System Advisor Model (SAM). Available at: https://sam.nrel.gov.

[11] A. Meflah, F. Chekired, N. Drir and L. Canale, "Accurate method for solar power generation estimation for different PV panels technologies", *Resources* 2024, 13(12), 166, doi.org/10.3390/resources13120166.

[12] J. AlFaraj, E. Popovici and P. Leahy, "Solar irradiance database comparison for PV system design: A case study", *Sustainability* 2024, 16(15), 6436, doi.org/10.3390/su16156436.

[13] C. Luo, N. Al-Messabi, Z. Kuang, C. Ma, I. El-Amin, H. Deng, Y. Li, "Photovoltaic system modeling and forecasting techniques: A survey", *Engineering Applications of Artificial Intelligence*, Volume 162, Part E, 2025, doi.org/10.1016/j.engappai.2025.112516.

[14] S. Baran, J.C. Marín, O. Cuevas, M. Díaz, M. Szabó, O. Nicolis, M. Lakatos, "Machine-learning-based probabilistic forecasting of solar irradiance in Chile", *Advances in Statistical Climatology, Meteorology and Oceanography*, Volume 11, issue , pp. 89–105, 2025, doi.org/10.5194/ascmo-11-89-2025.

[15] LI-200 Pyranometer Light Sensors. Available online: http://www.licor.com/env/products/light/pyranometer

Annals of the University of Craiova, Electrical Engineering series, No. 49, Issue 1, 2025; ISSN 1842-4805 eISSN 2971-9852

DOI: 10.52846/AUCEE.2025.05

Practical Installation of a Battery Management System with V2X Capability

Mihai Rotaru*, Mihai Iordache*, Steliana Pușcașu* and Georgiana Zainea*

* Electrical Engineering Faculty, National University of Science and Technology POLITEHNICA Bucuresti, Bucharest, Romania, mihai.rotaru2002@stud.electro.upb.ro, ORCID: 0009-0004-3277-6775, mihai.iordache@upb.ro, ORCID: 0000-0002-2990-0227, steliana.puscasu@upb.ro, ORCID: 0009-0008-5898-0634, georgiana.zainea@upb.ro, ORCID: 0000-0002-5599-7210

Abstract - **This paper presents an experimental demonstration of a basic bidirectional energy transfer consistent with the Vehicle-to-Everything (V2X) concept, using a commercial Battery Management System (BMS) not originally intended for automotive applications. A 14-series (14S) lithium-ion battery pack integrated with a 48 V BMS and a bidirectional inverter is experimentally evaluated under low-power operating conditions. The study focuses on practical system integration, protection behavior, and cell balancing functionality using minimal laboratory equipment. The results show that essential BMS functions are sufficient to support controlled bidirectional energy flow at low power levels, highlighting both the feasibility and limitations of low-cost BMS-based V2X experimental setups.**

Cuvinte cheie: *baterie, sistem de management al bateriei (BMS), vehicul electric (EV), capabilitate V2X.*

Keywords: *battery, battery management system (BMS), electric vehicle (EV), V2X capability.*

I. INTRODUCTION

Battery Management Systems (BMS) are essential components for the safe and reliable operation of lithium-ion battery packs in electric vehicles (EVs), stationary storage systems, and other energy-related applications. Their primary role is to ensure that battery cells operate within predefined electrical and thermal limits by continuously monitoring cell voltages, current, temperature, and state of charge (SOC), while implementing protection and balancing mechanisms to prevent degradation or hazardous conditions [1]-[3]. Advanced BMS architecture also includes model-based estimation algorithms and diagnostic functions [4], [20].

Traditionally, BMS architectures are designed to support unidirectional energy flow, where the battery pack is charged from an external source and discharged to supply a dedicated load. In this context, the BMS mainly functions as a supervisory and protective unit, without actively participating in energy exchange control beyond enforcing safety constraints [5]. However, the increasing penetration of electric vehicles and distributed energy resources has accelerated interest in bidirectional energy transfer concepts, commonly referred to as Vehicle-to-Everything (V2X). V2X encompasses Vehicle-to-Grid (V2G), Vehicle-to-Home (V2H), and Vehicle-to-Load (V2L) interactions, enabling batteries to act as temporary energy storage units capable of supplying external loads or the electrical grid [6], [7]. The economic and grid-support potential of V2G systems has been extensively analyzed in the literature [8].

In conventional automotive implementations, V2X functionality relies on advanced power electronics, dedicated communication protocols, and grid-compliant control strategies, typically integrated into the vehicle's onboard charger and energy management system [4]. Such systems are complex, costly, and tightly coupled with manufacturer-specific hardware and software platforms. Consequently, experimental access to V2X functionality is often limited, particularly in academic or educational environments.

From a theoretical perspective, the feasibility of bidirectional energy flow is primarily governed by the capability of the power conversion stage and the BMS to maintain safe operating conditions during both charging and discharging processes. While the inverter or bidirectional converter determines the direction and quality of energy transfer, the BMS remains responsible for enforcing voltage limits, current constraints, and cell balancing requirements [5], [9]. Even in the absence of grid-synchronized control or communication layers, a BMS that ensures stable and balanced operation of a battery pack can enable a basic form of bidirectional energy utilization, particularly at low power levels.

In this context, the present work investigates the use of a commercial 14S, 48 V BMS, originally intended for light electric mobility applications such as electric scooters, in a simplified experimental configuration aimed at demonstrating fundamental V2X principles. The BMS is integrated with a 14-cell lithium-ion (18650) battery pack and a commercially available bidirectional inverter, forming a laboratory-scale system capable of charging the battery pack and subsequently supplying an external AC load of up to 100 W. Unlike full-scale automotive V2X systems, the proposed setup does not implement grid interaction, communication protocols, or active power control strategies. Instead, it focuses on the physical feasibility of bidirectional energy transfer under the supervision of a standard BMS.

The main objective of this study is to experimentally assess the role of essential BMS functions (cell voltage monitoring, protection mechanisms, SOC supervision, and cell balancing) in supporting controlled bidirectional operation using accessible and low-cost components. By emphasizing practical system integration and real operating conditions, this work aims to bridge the gap between theoretical V2X concepts and simplified experimental validation platforms.

Having established the theoretical background and motivation for employing a non-automotive BMS in a bidirectional energy flow scenario, the following sections present the materials, methods, and experimental setup in detail, followed by an analysis of the observed system behavior and limitations.

II. MATERIALS, METHODS AND SCHEMATICS OF THE PRACTICAL INSTALLATION

A. *System Architecture and Practical Implementation*

The overall electrical configuration of the experimental setup, including the battery pack, Battery Management System (BMS), inverter, and protection elements, is illustrated in Figure 1.

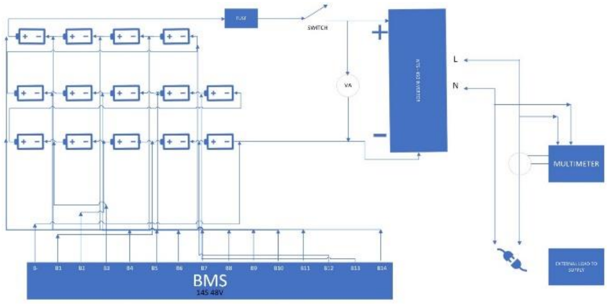

Fig. 1. Electrical wiring diagram of the practical installation.

Figure 1 illustrates the electrical wiring diagram of the proposed experimental setup, which represents a laboratory-scale implementation of a bidirectional energy transfer system supervised by a Battery Management System (BMS). The schematic provides a detailed representation of the electrical interconnections between the battery pack, the BMS, the inverter, and the external load, emphasizing the practical realization of the system under real operating conditions.

The core of the installation consists of a 14-series (14S) lithium-ion battery pack, assembled from individual 18650 cells and connected to a commercial 48 V BMS. Each cell connection is routed to the BMS through dedicated sense wires, enabling continuous monitoring of individual cell voltages. This configuration allows the BMS to detect voltage imbalances and activate the internal balancing circuitry when predefined thresholds are exceeded. The BMS is connected in series with the battery pack on both the charging and discharging paths, ensuring that all current flowing into or out of the battery is supervised and protected.

A bidirectional inverter is interfaced with the battery pack through the BMS power terminals, enabling the conversion between direct current (DC) and alternating current (AC). In charging mode, the inverter operates as an AC–DC converter, supplying controlled DC power to charge the battery pack. In discharging mode, the inverter converts the DC energy stored in the battery into AC power to supply an external load. The inverter selection was based on compatibility with the nominal 48 V battery voltage and the availability of integrated protection feature relevant for experimental validation.

To ensure operational safety and facilitate experimental observation, additional protective and measurement components were incorporated into the installation. A fuse rated at 16 A was placed in series on the main DC power line supplying the inverter, providing protection against overcurrent and short-circuit conditions. A manual DC disconnect switch was also included, allowing complete electrical isolation of the inverter from the battery pack during setup, maintenance, or emergency conditions.

Electrical measurements of the battery pack voltage and current were performed using a combined voltmeter–ammeter instrument connected in series with the DC link. This instrumentation enables real-time monitoring of the charging and discharging processes, ensuring that the operating limits defined by the BMS—namely maximum charging voltage and minimum discharge voltage—are not exceeded. On the AC side, the inverter output is provided through a standard Schuko socket, allowing the connection of common household loads. For experimental evaluation, a low-power load was selected to ensure operation within the safe current limits of both the inverter and the BMS.

The schematic shown in Figure 1 bridges the gap between theoretical V2X concepts and their practical realization by illustrating a simplified but functional configuration. While the setup does not include grid synchronization, communication interfaces, or advanced energy management algorithms, it captures the essential elements required for controlled bidirectional energy transfer. This approach enables a clear assessment of the role played by the BMS in supervising battery operation during both charging and discharging phases.

The experimental methodology adopted in this work focuses on repeatable charge–discharge cycles performed under controlled conditions. During each test, the battery pack is charged up to the maximum allowable voltage defined by the BMS and subsequently discharged by supplying an external AC load until the minimum voltage threshold is reached. This procedure allows direct observation of BMS protection behavior, inverter operation, and cell balancing activity, providing a consistent basis for the analysis presented in the following sections.

B. *Experimental Procedure*

The experimental evaluation was carried out through controlled charge–discharge cycles to assess the behavior of the Battery Management System (BMS), the inverter, and the battery pack during bidirectional energy transfer. All tests were performed under laboratory conditions, with operating parameters selected within the nominal limits specified by the equipment manufacturers.

Prior to testing, the battery pack connections and BMS sense wiring were verified, and the initial state of charge (SOC) of the individual cells was assessed by measuring their open-circuit voltages. The charging process was performed using the inverter operating in AC–DC mode, while the battery voltage and current were continuously monitored. Charging was terminated when the total pack voltage reached 58.8 V, corresponding to 4.2 V per cell in the 14S configuration.

Subsequently, the system was operated in discharging mode by supplying a low-power AC load of approximately 45 W through the inverter in DC–AC conversion mode. The discharge process was stopped when the battery voltage decreased to the minimum allowable limit of 44.8 V (3.2 V per cell). During both operating modes, the activation of BMS protection and cell balancing functions was monitored through voltage and current measurements. The experiments were repeated under identical conditions to ensure repeatability, and the recorded data were used for the analysis presented in the following sections

III. EQUIPMENT USED IN ASSEMBLY

A. *Battery pack*

The experimental setup employs a lithium-ion battery pack assembled from cylindrical 18650 cells, a widely used cell format in energy storage and electric mobility applications due to its favorable energy density, availability, and cost-effectiveness [2]– [10]. The 18650 cells have standardized mechanical dimensions of 18 mm in diameter and 65 mm in height, which facilitates modular pack assembly and reproducibility of experimental configurations. However, lithium-ion chemistry imposes strict safety constraints regarding voltage and temperature limits [11].

The battery pack used in this work consists of 14 lithium-ion cells connected in series (14S configuration), resulting in a nominal voltage compatible with the selected 48 V Battery Management System (BMS). The individual cells are of type 18650C, manufactured by YDJW, with a nominal energy rating of 9.25 Wh per cell. The main electrical and thermal characteristics of the employed cells are summarized in Table I.

TABLE I.
TYPICAL SPECIFICATIONS OF THE 18650 LITHIUM-ION CELLS USED IN THE BATTERY PACK

Parameter	Value
Nominal cell voltage	3.7 V
Cell capacity	2200–3500 mAh
Nominal energy	9.25 Wh
Continuous discharge rate	2C–20C
Recommended charging current	0.5C–1C
Cycle life	500–800 cycles
Operating temperature	0°C to 45°C
Cell mass	45–50 g
Cell dimensions	18 mm × 65 mm

The selection of 18650 cells is justified by their stable voltage characteristics over a wide state-of-charge (SOC) range and their suitability for low- to medium-power experimental applications. These characteristics make them appropriate for investigating controlled charge–discharge behavior under the supervision of a commercial BMS.

B. *Inverter*

The conversion between direct current (DC) and alternating current (AC) in the proposed setup is performed using a Mean Well NTS-450 inverter. This inverter generates a pure sinusoidal AC output and is commonly employed in off-grid, mobile, and backup power systems due to its reliability and integrated protection features [10],[13].

In the present application, the inverter serves a dual role: it enables charging of the battery pack from an AC source and, during discharging, supplies AC power to an external load. The inverter was selected based on its compatibility with the nominal 48 V battery voltage and its power rating, which significantly exceeds the low-power experimental load used in this study, ensuring operation within safe limits. The electrical characteristics and protection thresholds were verified using the manufacturer’s official technical documentation [15].

The main characteristics of the inverter relevant to the experimental setup are summarized in Table II.

TABLE II.
MAIN CHARACTERISTICS OF THE INVERTER USED IN THE EXPERIMENTAL SETUP

Parameter	Value
Inverter model	Mean Well NTS-450
Rated output power	450 W
Input voltage	48 V DC
Output voltage	230 V AC
Output waveform	Pure sine wave
Efficiency	>90% (typical)
Integrated protections	Overload, short circuit, over-temperature, low battery voltage

By operating the inverter well below its rated power, the experimental setup minimizes thermal stress and conversion losses, allowing a clearer assessment of the BMS-supervised bidirectional energy flow.

C. *BMS (Battery Management System)*

The battery pack is supervised by a commercial 14S, 48 V Battery Management System designed for lithium-ion battery applications. The primary function of the BMS is to ensure safe battery operation by continuously monitoring electrical parameters and enforcing protection thresholds during both charging and discharging processes.

The BMS supports cell balancing, which is essential for series-connected battery packs to reduce voltage imbalances caused by manufacturing tolerances, aging effects, or uneven load distribution. The employed BMS implements passive balancing, where excess energy from higher-voltage cells is dissipated as heat through resistive elements [5]. Compared to passive balancing, active balancing improves overall efficiency and enhances the usable capacity of the battery pack, particularly in low-power, long-duration applications. Passive balancing remains the most used method in low-cost commercial BMS implementations due to its simplicity and reliability [12].

The codification and main electrical characteristics of the employed BMS are presented in Table III.

The selected BMS operates as a supervisory and protective element rather than an active energy management controller. Nevertheless, its essential functions—cell voltage monitoring, protection enforcement, and balancing—are sufficient to support the low-power bidirectional energy transfer investigated in this work.

State-of-charge estimation methods typically rely on coulomb counting and model-based correction techniques [18].

TABLE III.
MAIN SPECIFICATIONS OF THE BATTERY MANAGEMENT SYSTEM

Parameter	**Value**
Cell configuration	14S
Nominal pack voltage	48 V
Maximum charging voltage	58.8 V
Minimum discharge voltage	44.8 V
Maximum continuous current	20 A
Cell balancing	Passive / Active (model-dependent)
Protection functions	Overcharge, over-discharge, over-current, short circuit, temperature
SOC estimation	Yes

IV. RESULTS AND PRACTICAL ASSEMBLY

This section presents the experimental results obtained from the practical implementation described in Section II, with emphasis on charging and discharging behavior, protection enforcement by the Battery Management System (BMS), and the observed effectiveness of cell balancing in a low-power bidirectional energy transfer scenario.

A. *Practical Assembly and Initial Observations*

The practical assembly of the experimental setup enabled direct observation of BMS-supervised battery operation during controlled charge–discharge cycles. Initial measurements indicated small voltage differences between individual cells within the 14S lithium-ion battery pack, attributable to manufacturing tolerances and prior usage history.

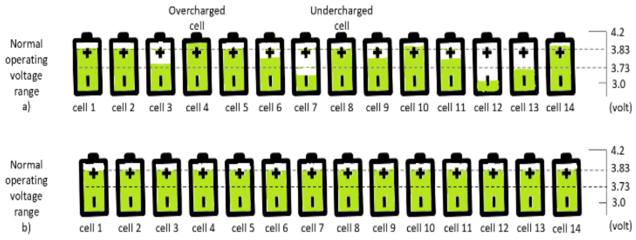

Fig. 2. Cell balancing technique.

Figure 2 provides a conceptual reference for interpreting experimental observations related to cell imbalance and subsequent voltage equalization during system operation.

B. *Charging and Discharging Experimental Results*

During the charging phase, the battery pack voltag increased progressively under BMS supervision unt reaching the maximum allowable voltage of 58.8 V (4.2 per cell). The charging process was terminated at thi threshold, confirming correct overvoltage protection behavior. No abnormal current levels or protection-triggere interruptions were observed.

In the discharging phase, the inverter supplied a low-power external AC load rated at approximately 45 W. The battery voltage decreased smoothly until the minimum cutoff limit of 44.8 V (3.2 V per cell) was reached, at which point the discharge process was stopped in accordance with the BMS protection strategy. Deep discharge below recommended voltage thresholds significantly accelerates capacity degradation in lithium-ion cells [12].

TABLE IV.
EXPERIMENTAL CHARGING AND DISCHARGING RESULTS

Parameter	**Charging phase**	**Discharging phase**
Battery pack voltage range [V]	53.1 – 58.8	58.8 – 44.8
Average battery current [A]	2.2	0.95
Peak battery current [A]	2.8	1.1
AC load power [W]	–	45
Operating mode	AC–DC	DC–AC

The measured values indicate stable system operation well within the continuous current rating of the BMS, validating the suitability of the selected components for low-power bidirectional operation.

C. *Cell Balancing Performance*

Initial voltage measurements revealed a noticeable, though moderate, dispersion among the individual cell voltages within the battery pack. During successive charge–discharge cycles, the BMS automatically activated its cell balancing function, resulting in a gradual reduction of voltage differences between cells. Cell-to-cell variations significantly influence long-term performance and lifetime in automotive battery packs [21].

TABLE V.
CELL VOLTAGE DISPERSION BEFORE AND AFTER BALANCING

Operating condition	**Max cell voltage [V]**	**Min cell voltage [V]**	**Voltage difference [mV]**
Before balancing	4.11	4.01	100
After balancing	4.07	4.04	30
During discharge	3.46	3.42	40

The quantitative reduction in voltage dispersion confirms the effectiveness of the balancing mechanism in maintaining a more uniform state of charge across the series-connected cells.

To further contextualize these results, representative battery behavior with and without effective balancing is illustrated in Figures 3–6.

Figure 3 shows the battery pack at full charge under balanced conditions, where cell voltages are nearly uniform, confirming effective BMS supervision.

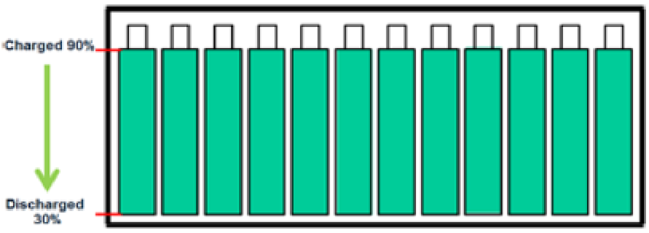

Fig 3. Battery pack at full capacity

Figure 4 illustrates a mismatched discharged pack, highlighting voltage dispersion between cells that can lead to premature cutoff and reduced usable capacity.

Figure 5 presents full discharge with active balancing enabled, demonstrating improved voltage uniformity and better energy utilization.

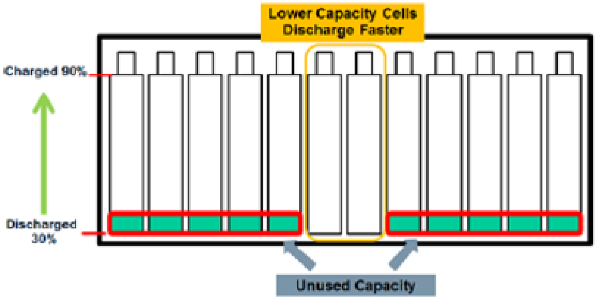

Fig 4. Mismatched discharged battery pack

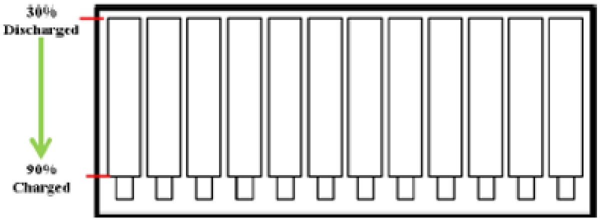

Fig 5. Full depletion with active balancing

Figure 6 depicts charging without balancing, where certain cells reach the maximum voltage limit earlier, increasing the risk of overvoltage protection activation.

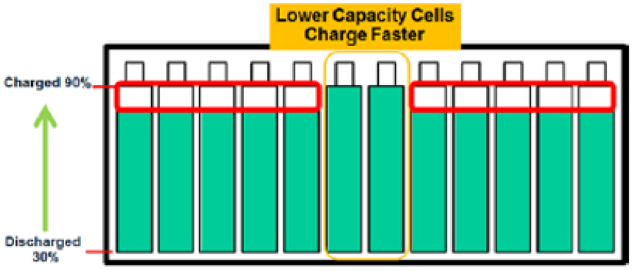

Fig 6. Charging without balancing

D. Discussion and System-Level Interpretation

The experimental observations confirm that one of the primary responsibilities of a BMS—maintaining lithium-ion cells within safe operating limits—is effectively fulfilled during both charging and discharging. This function becomes particularly relevant in bidirectional energy transfer scenarios, where repeated cycling may otherwise accelerate cell degradation. Repeated cycling associated with V2X services may increase degradation if proper voltage and thermal control is not enforced [14], [16].

Although the internal balancing algorithm of the commercial BMS used in this study is not directly accessible, the observed voltage convergence behavior is consistent with the decision-making principles illustrated in Figure 7.

To emphasize the scope and originality of the proposed setup, a comparison with conventional automotive V2X systems is presented in Table VI.

Overall, the results validate the original contribution of this work: a standard, low-cost BMS can effectively supervise controlled bidirectional energy transfer under laboratory conditions, enabling functional demonstration of fundamental V2X principles using accessible components.

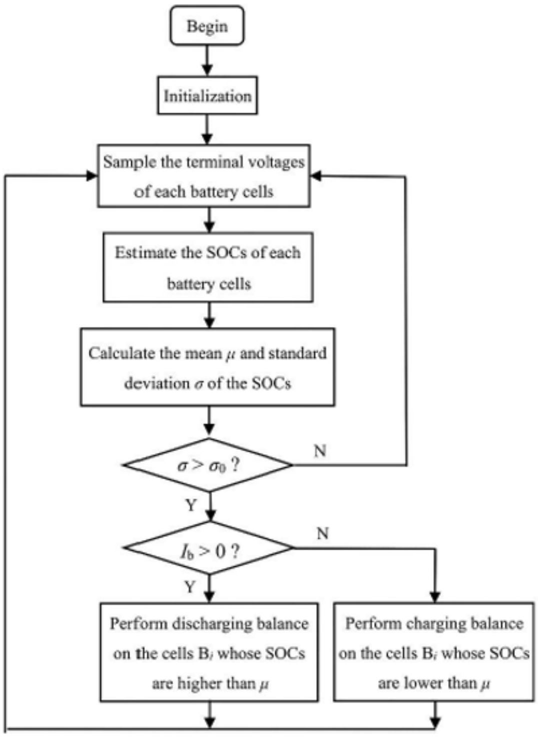

Fig. 7. Flowchart of active cell balancing method.

TABLE VI.
COMPARISON BETWEEN THE PROPOSED EXPERIMENTAL SETUP AND CONVENTIONAL V2X SYSTEMS

Feature	**Proposed setup**	**Automotive V2X systems**
BMS type	Commercial, non-automotive	Automotive grade
Power level	Low (<100 W)	kW range
Grid synchronization	No	Yes
Communication protocols	No	Yes
Intended application	Experimental / educational	Grid services

Advanced prognostic approaches based on probabilistic models are increasingly used for remaining useful life prediction in lithium-ion batteries [19].

V. CONCLUSIONS

This paper presented an experimental validation of a simplified bidirectional energy transfer setup supervised by a commercial Battery Management System (BMS) not originally intended for automotive applications. A 14-series lithium-ion battery pack integrated with a 48 V BMS and a commercial inverter was successfully operated under controlled laboratory conditions to supply a low-power external AC load.

The experimental results demonstrated that essential BMS functions—cell voltage monitoring, protection enforcement, and balancing—are sufficient to ensure safe and stable operation during both charging and discharging at power levels below 100 W. Measured voltage and current profiles confirmed correct activation of overvoltage and undervoltage protection thresholds, while observed reductions in cell voltage dispersion validated the effectiveness of the balancing mechanism.

Although the proposed setup does not implement grid synchronization, communication protocols, or active power management strategies required for full Vehicle-to-Grid (V2G) operation, it provides a practical and reproducible platform for preliminary testing and educational demonstrations of fundamental V2X concepts. The use of accessible, low-cost components highlights both the feasibility and the inherent limitations of non-automotive BMS solutions in bidirectional energy transfer applications.

Future work will focus on extending the experimental platform toward higher power levels, integrating measurement of individual cell currents, and exploring advanced control strategies to bridge the gap between simplified laboratory demonstrations and fully compliant V2X systems.

ACKNOWLEDGMENT

Source of research funding in this article: This research received no external funding.

Contribution of authors:
First author – 40%
First coauthor – 25%
Second coauthor – 20%
Third coauthor – 15%

Received on September 24, 2025
Editorial Approval on December 7, 2025

REFERENCES

[1] B. Barré, B. Deguilhem, S. Grolleau, M. Amara and S. Gérard, ”A review on lithium-ion battery ageing mechanisms and their impact on electric vehicle range,” *Journal of Power Sources*, 241, pp.680-689, 2013, doi: 10.1016/j.jpowsour.2013.05.040.

[2] A. Miłkowski and B. Orłowska, ”Battery management systems: Challenges associated with lithium-ion battery applications in electric and hybrid vehicles,” *Przeglad Elektrotechniczny*, 92, pp.165-170, 2016, doi: 10.1007/978-981-96-6624-9_9.

[3] A. Jossen, V. Späth, H. Doring and J. Garche, ”Reliable battery operation—a challenge for the battery management system, ” *J. Power Sources*, 84, pp. 283–286, 1999, doi:10.1016/S0378-7753(99)00329-8.

[4] G. L. Plett, *Battery Management Systems, Volume I: Battery Modeling*, Norwood:Artech House, 2015.

[5] J. Cao, N. Schofield and A. Emadi, “Battery balancing methods: A comprehensive review”. In *Proceedings of IEEE Vehicle Power Propulsion Conference* (VPPC 2008), Harbin, China, 3–5 September 2008, pp. 1–6, doi: 10.1109/VPPC.2008.4677669.

[6] M. Ehsani, M. Falahi and S. Lotfifard. “Vehicle to grid services: Potential and applications,” *Energies*, 5, pp. 4076-4090, 2012, doi:10.3390/en5104076.

[7] S. Duryea, S. M. Islam and W. Lawrance, “A battery management system for stand-alone photovoltaic energy systems,” *IEEE Industry Applications Magazine*, 7(3): pp. 67 – 72, 2001, doi: 10.1109/2943.922452.

[8] W. Kempton and J. Tomic, “Vehicle-to-grid power fundamentals: Calculating capacity and net revenue, ” *Journal of Power Sources*, 144(1), pp. 268–279, June 2005, doi: 10.1016/j.jpowsour.2004.12.025.

[9] Q. Zhang and R. E. White, “Capacity fade analysis of a lithium-ion cell,” *J. Power Sources*, 179, pp. 793–798, May 2008, doi: 10.1016/j.jpowsour.2008.01.028.

[10] K. H. Chao and J.W. Chen, “State-of-health estimator based on extension theory with a learning mechanism for lead-acid batteries,” *Expert Syst. Appl*., 38, pp. 15183–15193, 2011, doi: 10.1016/j.eswa.2011.05.084.

[11] J. M. Tarascon and M. Armand, “Issues and challenges facing rechargeable lithium batteries,” *Nature*, 414, pp. 359–367, 2001 doi: 10.1038/35104644.

[12] A. Khaligh and Z. Li, “Battery, ultracapacitor, fuel cell, and hybrid energy storage systems for electric vehicles,” *IEEE Transactions on Vehicular Technology*, 59(6), pp. 2806–2814, 2010, doi: 10.1109/TVT.2010.2047877.

[13] A. A. Pesaran, “Battery thermal models for hybrid vehicle simulations,” *J. Power Sources*, 10, pp. 377–382, 2002, doi: 10.1016/S0378-7753(02)00200-8.

[14] J. B. Goodenough and K. S. Park, “The Li-ion rechargeable battery: a perspective,” *J Am Chem Soc.*, 135(4), pp. 1167-1176, Jan 2013, doi: 10.1021/ja3091438.

[15] Mean Well. (n.d.). NTS-450 Series Datasheet. Retrieved from https://www.meanwell.com/productPdf.aspx?i=1018.

[16] M. Uno and K. Tanaka, “Influence of high-frequency charge–discharge cycling induced by cell voltage equalizers on the life performance of lithium-ion cells,” *IEEE Trans. Veh. Technol.*, 60, pp.1505–1515, 2011, doi: 10.1109/TVT.2011.2127500.

[17] K, S. Ng, C. S. Moo, Y. P. Chen and Y. C. Hsieh, “Enhanced Coulomb counting method for estimating state-of-charge and state-of-health of lithium-ion batteries,” *Appl. Energy*, 86, pp. 1506–1511, 2009, doi: 10.1016/j.apenergy.2008.11.021.

[18] W. He, N. Williard, M. Osterman and M. Pecht, “Prognostics of lithium-ion batteries based on Dempster–Shafer theory and the Bayesian Monte Carlo method,” *Journal of Power Sources*, vol. 196, iss. 23, pp. 10314-10321, 2011, doi: 10.1016/j.jpowsour.2011.08.040.

[19] R. Ravi and U. Surendra, “Battery Management Systems (BMS) for EV: Electric Vehicles and the Future of Energy-Efficient Transportation,” in *Electric Vehicles and the Future of Energy Efficient Transportation*, pp.1-35, 2021, doi: 10.4018/978-1-7998-7626-7.ch001

[20] N. I. Nikolov, A. Chahbaz, F. Hildenbrand, M. Kateri, D. Uwe Sauer, “Statistical investigation of temperature-dependent cycle lifetime and cell-to-cell variance in lithium-ion batteries: A model-based approach,” *Journal of Power Sources*, vol. 623, 2024, 235334, doi:10.1016/j.jpowsour.2024.235334.

[21] S. Lee, J. Kim, J. Lee and B.H. Cho, “State-of-charge and capacity estimation of lithium-ion battery using a new open-circuit voltage versus state-of-charge,” *Journal of Power Sources*, vol. 185, iss.2, pp. 1367-1373, 2008, doi: 10.1016/j.jpowsour.2008.08.103.

[22] M.A. Hannan, M.M. Hoque, A. Mohamed and A. Ayob, “Review of energy storage systems for electric vehicle applications: Issues and challenges,“ *Renewable and Sustainable Energy Reviews*, vol. 69, pp. 771-789, 2017, doi: 10.1016/j.rser.2016.11.171.

Annals of the University of Craiova, Electrical Engineering series, No. 49, Issue 1, 2025; ISSN 1842-4805 eISSN 2971-9852

DOI: 10.52846/AUCEE.2025.06

Simplified Field-Oriented Control Algorithm Implementation on 1.15 MW Traction System

Constantin Vlad Suru[*], Tudor Mătușa[†], Mihaela Popescu[*] and Alexandru Bitoleanu[*]
[*] University of Craiova/Department of Electromechanics, Environment and Applied Informatics, Craiova, Romania,
vsuru@em.ucv.ro, mpopescu@em.ucv.ro, a_bitoleanu@yahoo.com,
ORCID: 0000-0002-2839-1686, 0000-0002-5292-5529, 0000-0001-9621-5011
[†] Promat SA, Craiova, Romania, matusa.tudor.e8y@student.ucv.ro, ORCID: 0009-0006-7263-547X

Abstract - **The purpose of this work is the implementation and experimental validation of a quasi-oriented rotor flux control algorithm on a full scale, railway locomotive traction system. This control method can be useful for industrial applications based on DSPs which have limited computation power, given the fact that the real time flux-oriented control needs relatively high computation power, especially for the flux estimator. The advantage of this method is given by the elimination of flux estimation as it assumes the control system is oriented. This way, a processor hungry control section is avoided, the flux control loop being also avoided. The control algorithm had been implemented in the Matlab Simulink environment, using the dSPACE RTI toolbox, for the DS1103 prototyping board. The dSPACE board had been used for the control of the full-scale traction system experimental stand.**

Cuvinte cheie: *control cu orientare după câmp, sistem de tracțiune, control cu DSP.*

Keywords: *field-oriented control, traction system, DSP control.*

I. INTRODUCTION

For its known advantages, the induction motor is widely used for the traction system of modern rail vehicles [1][2][3][4]. Irrespective to the vehicle traction power, the traction system is equipped with multiple relatively large power induction motors. The control of the traction system is assured by a DSP [5]. For the most railway vehicles, the power inverter is fed from the overhead catenary by means of a power transformer and bidirectional rectifier (necessary to recover the braking energy to the power grid. A new type of railway vehicles is the battery fed locomotives which can recover the braking energy by charging the battery [6]. The disadvantage of induction motor traction systems is given by the relatively complex and computing hungry closed loop control system. An example of such a control system is the rotor field-oriented control algorithm which can give good results, but which needs the estimation of the motor flux [4][5]. The flux estimator is sensitive to computing error; therefore, it needs a high-performance DSP which can give a sufficiently small sample time [7][8].

Another limitation of such systems is the relatively low switching frequency of the power inverter transistors which leads to high current ripple.

The prototyping systems are characterized by high computing power (as dSPACE DS1103, for example [9]), but industrial DSPs have limited computing power, which means that the sample time is inevitably higher for the latter. High sample time values lead to cumulative computing errors which can further lead to instable and peculiar system response, different than the response defined by the equations [7].

An alternative to a small sample time is a simpler control algorithm, obtained by eliminating the flux estimator and assuming that the control system is oriented. The control algorithm becomes quasi-oriented, which had been validated on a small-scale experimental system [10].

After the introduction, the simplified, quasi-oriented control algorithm is briefly described in the second section, and its implementation is presented in the third section. The experimental setup is described in the fourth section and the experimental results are discussed in the sixth section. Finally, the conclusions are drawn.

II. SIMPLIFIED ROTOR FIELD ORIENTED CONTROL ALGORITHM

For the rotor field-oriented control, the motor currents are computed in a rotating referential (d-q) which is synchronized with the rotor flux. Because the flux estimator is no longer used, the rotor flux is now unknown, so the algorithm uses the assumption that the system is oriented. The advantage is given by the fact that the flux estimator is not used. This implies that the flux controller can be eliminated also. The disadvantage is given by the fact that the active and magnetizing motor current components cannot be regulated separately (on the d and q axes) but commonly, by regulating the motor current magnitude [10].

The simplified control is illustrated in Fig. 1 [10], where:

- $|I_m|$ - motor current magnitude computation block;
- R_i - motor current magnitude controller;
- VSI - voltage source inverter;
- ≋ - Sinusoidal control signals generator;
- f_2^* - slip frequency computation block.

The algorithm inputs are the imposed rotor flux and the imposed motor speed. For a given flux value, assuming that the control system is oriented, the imposed magnetizing current is [12][10]:

$$i_{sd} = \frac{1}{L_m}\cdot\left(\Psi_{rd} + T_r\cdot\frac{d\Psi_{rd}}{dt}\right) \qquad (1)$$

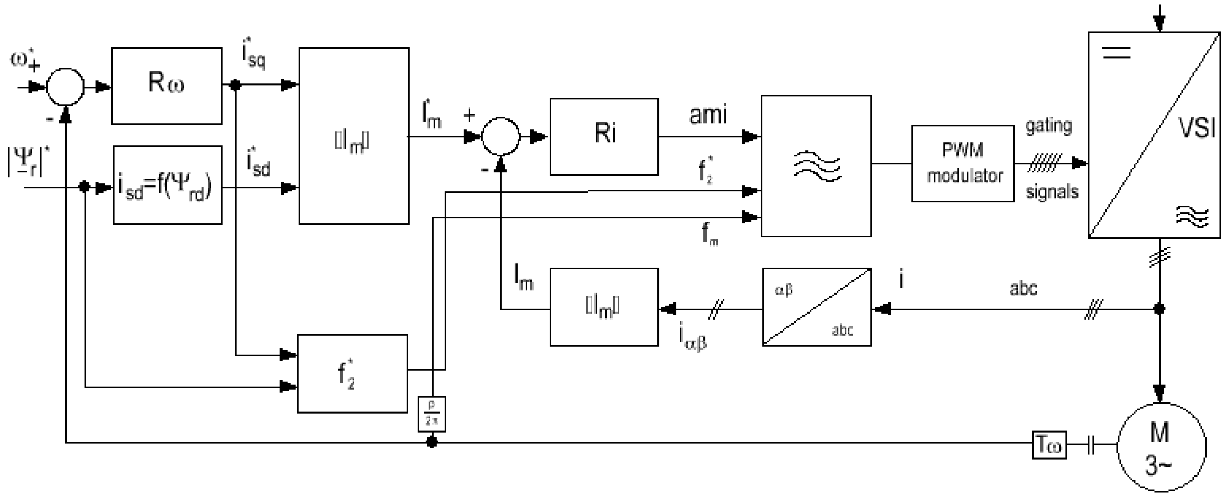

Fig. 1. Block diagram of the simplified field-oriented control algorithm

where:

- L_m - magnetizing inductance;
- Ψ_{rd} - rotor flux on d axis or the referential;
- T_r - rotor circuit time constant:

$$T_r = \frac{L_r}{R_r} = \frac{L_m + L_{\sigma r}}{R_r} \qquad (2)$$

- $L_{\sigma r}$ - rotor leakage inductance;
- R_r - rotor resistance.

The active current (q axis) is obtained at the output of the speed controller.

The imposed active and magnetizing currents are used for the magnitude of the imposed motor current phasor, which is regulated by a proportional-integrative regulator (Fig. 1):

The feedback quantity of the current magnitude controller is the real motor current phasor magnitude (computed from the sampled stator currents in the stationary reference frame [1][7], using the Clarke transform.

The current magnitude controller gives the amplitude modulation index (“ami” in Fig. 1) for the three-phase sinusoidal control voltages, software generated based on the motor frequency and slip frequency. The slip frequency is computed considering the imposed active current, and flux [12]:

$$f_2^* = i_{sq} \cdot \frac{L_m}{2 \cdot \pi \cdot \Psi_{rd} \cdot T_r} \qquad (3)$$

The software generated control voltages are applied to the sinusoidal PWM modulator.

III. SIMPLIFIED ROTOR FIELD CONTROL ALGORITHM IMPLEMENTATION

The control algorithm has been experimentally validated on a full-scale locomotive traction stand. The implementation was done for a dSPACE DS1103 prototyping board, programmed in Matlab Simulink (the machine code was obtained by compiling the model, using Simulink Coder and dSpace Real Time Interface library - Fig. 2.

Although the actual control system is synthetized in a grouped subsystem, some auxiliary blocks are needed:

- Model input signals, from the power section – the measured quantities from the transducers are acquired by the DS1103 analog to digital converters and made available to the model as Simulink signals by means of the RTI blocks attached to the board hardware resources;
    - The DS1103 analog inputs range is ±10V, so the transducers output signals had been calibrated to this range – yellow Gain blocks in Fig. 2. are used to denormalize the analog measured signals;
- Model output signals to the power section – gating pulses for the power transistors (obtained by the integrated PWM modulator), validation logic signals;
- Local blocks needed for real time control, imposed quantities and interlocks.

Although the inverter is controlled by the DS1103 board, the power inverter has its own local DSP who manages the power system initialization and protection (overcurrent, overvoltage, etc.). This means that some validation signals are exchanged between the DS1103 and the local DSP. A special kind of control signals received by the DS1103 are the signals from the locomotive control panel (containing the torque and speed levers).

The actual field-oriented control simplified algorithm is detailed in Fig. 3. It can be seen that the control system has two validation signals:

- The main validation signal, en, which validates the flux-imposed value and the current controller;
- The secondary validation signal, which validates the speed controller, the torque to active current conversion block (for manual, torque control), and the active current value.

The speed controller is a special proportional-integrative controller whose limits are dynamically adjusted (the upper and lower limits are given by the torque imposing lever.

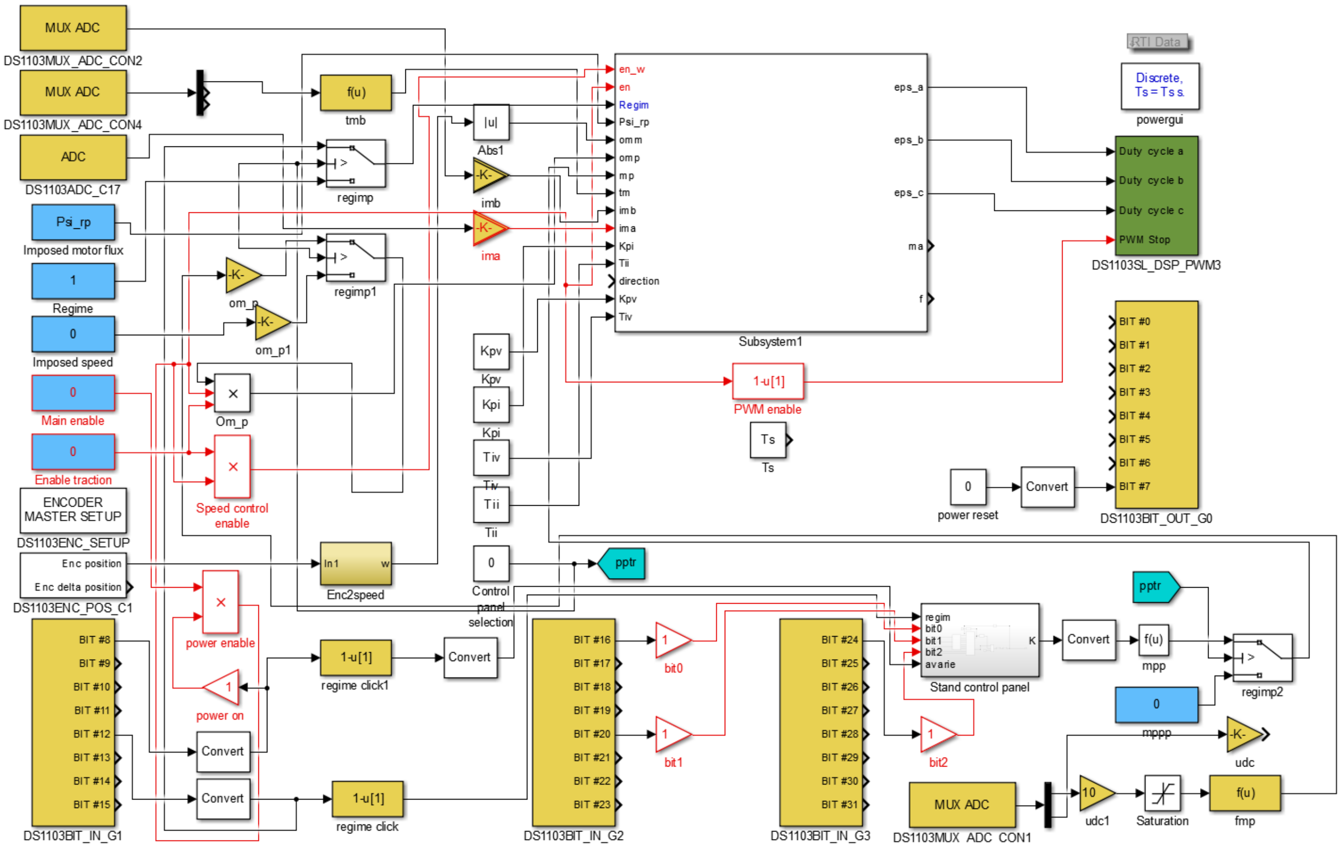

Fig. 2. Experimental Simulink control model

The remaining blocks in the control subsystem are:

- *im abc* - third motor phase current computation block (because only two currents are acquired);
- *Manual mode* - imposed torque to imposed active current conversion block;
- *Motor imposed flux* - gives the real time motor flux as a function of the imposed value, imposed torque and frequency (given the fact that the motor can operate above the rated speed);

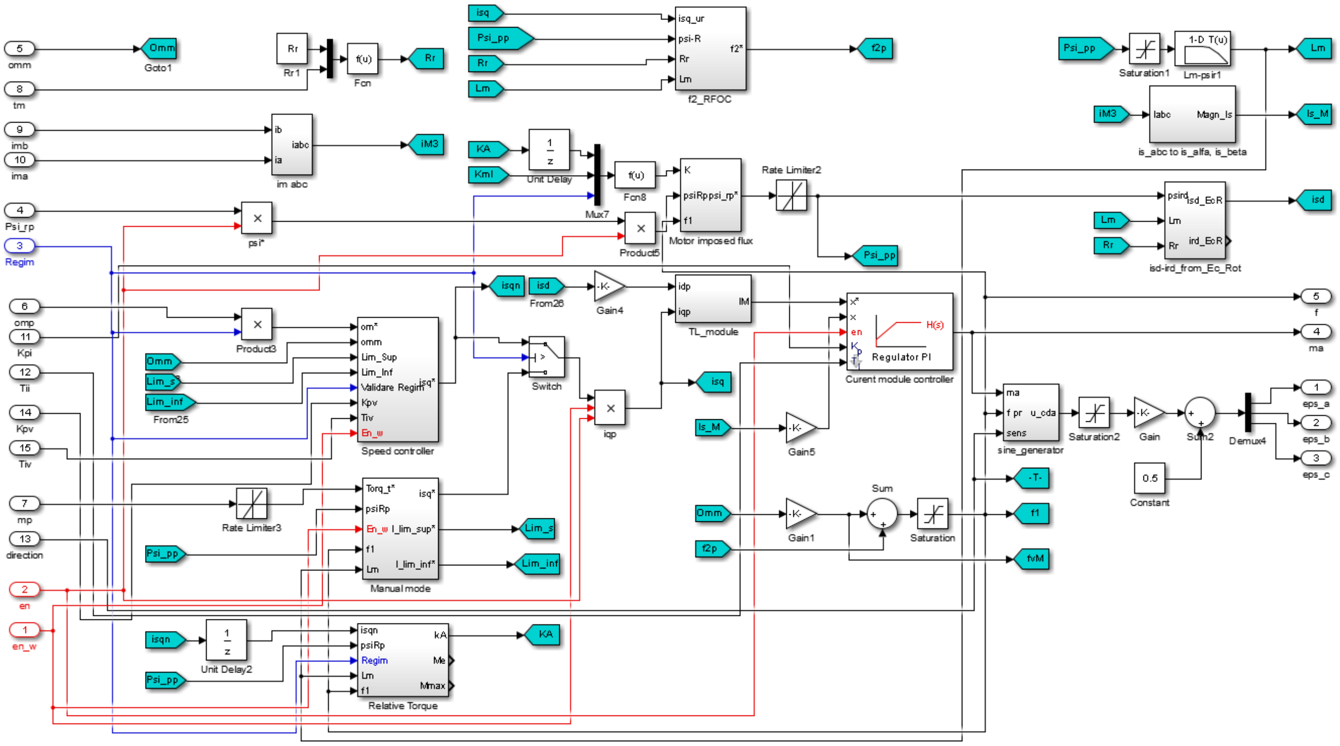

Fig. 3. The simplified field-oriented control system

- *f2_RFOC* - computes the slip frequency;
- *TL_module* - computes the imposed motor current magnitude from the d and q axis currents;
- *is_abc to is_alfa, is_beta* - computes the measured motor current magnitude în the $\alpha\beta$ referential;
- *isd-ird_from_Ec_Rot* - gives the imposed magnetizing current for the imposed flux;
- *sine_generator* - software generator of the three phase control signals for the PWM modulator.

The real-time control of the experimental system is done using a virtual control panel, built in ControlDesk NG, which gives the interface between the operator and the Simulink model parameters and signals [9][13]. By modifying the model block parameters, the validation signals and the control system parameters can be modified in real-time. The Simulink model signals can also be displayed on panel meters and virtual scopes.

At the same time, the panel meters are displaying instantaneous model signal values, so in order to virtually measure RMS or mean values, the corresponding quantity computing block is necessary.

The virtual control panel of the experimental traction system, captured during an experiment is illustrated in Fig. 4.

The data displayed on the virtual oscilloscopes was decimated, given the large timespan (75 s), therefore the lower left scope (displaying the three phase duty factors) is distorted. The low rate of change quantities (motor speed, current controller output and the current in the d-q referential) are displayed correctly.

IV. EXPERIMENTAL SETUP

The main elements of the experimental stand are:

- Single phase boost rectifier;
- Three-phase traction inverter;
- Three-phase traction motor:
  - U_N = 1400 V, I_N = 576 A, P_N = 1.39 MW;
  - f_N = 62.5 Hz; n_N = 1250 rpm.

The traction inverter is dedicated to the traction motor, so its rated parameters are in accordance. The inverter power source is a single-phase boost rectifier, which can have bidirectional power flow (the braking energy is recovered to the power grid). The DS1103 board controls only the inverter power transistors, the transistors if the boost rectifier are controlled by the power section local DSP (the traction rectifier was used just as power source, the DS1103 board cannot modify the imposed DC-Link voltage, but the work status of the rectifier is controlled by the DS1103 by means of the binary validation signals exchanged with the local DSP).

V. EXPERIMENTAL RESULTS

The experimental protocol considered the following steps:

- The system is initialized (the rectifier is connected to the grid and the DC-Link capacitor is charged to 1800 V);

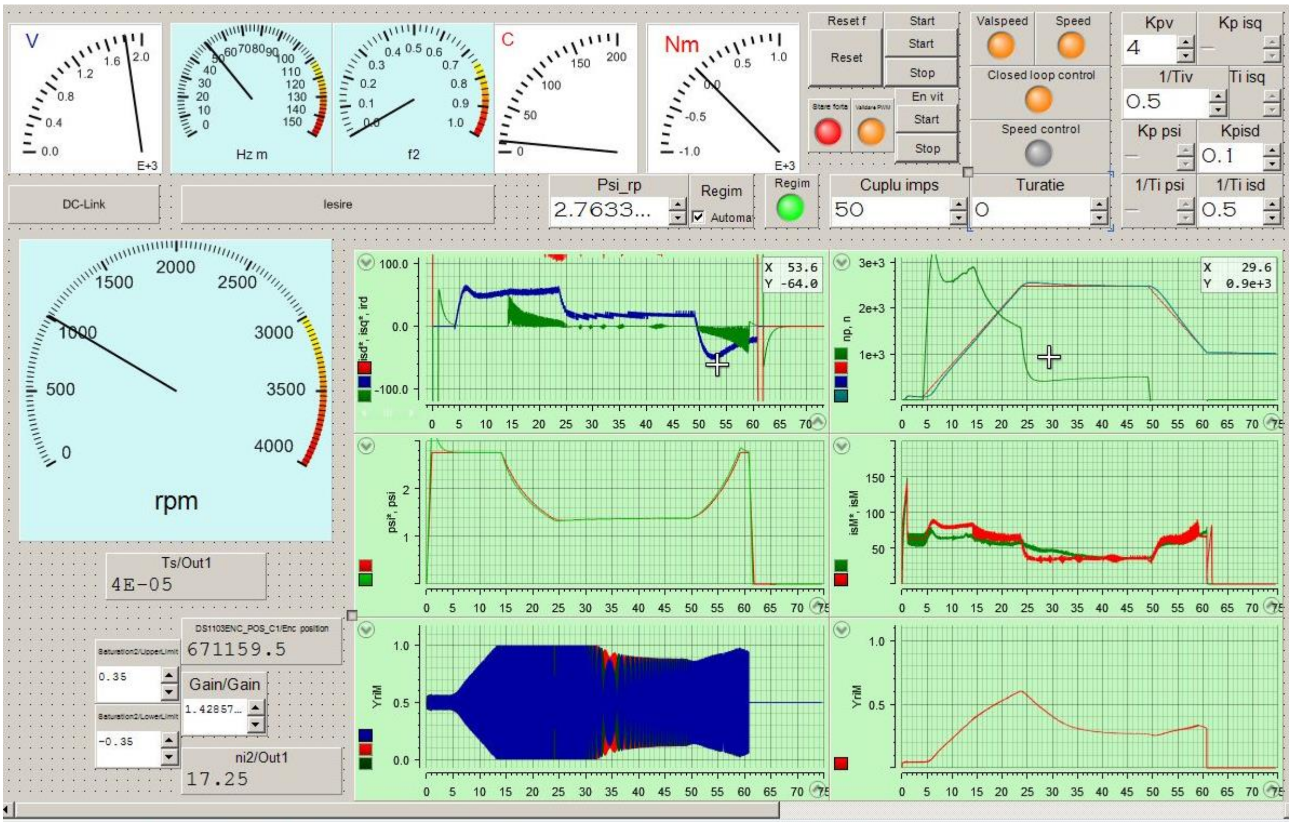

Kpv 4
Kp isq
1/Tiv 0.5
Ti isq
Kp psi
Kpisd 0.1
Psi_rp 2.7633...
Regim ☑ Automat
Cuplu imps 50
Turatie 0
1/Ti psi
1/Ti isd 0.5
Ts/Out1 4E-05
DS1103ENC_POS_C1/Enc position 671159.5
Saturation2/UpperLimit 0.35
Gain/Gain 1.42857...
Saturation2/LowerLimit -0.35
ni2/Out1 17.25

Fig. 4. The experimental traction system control panel

- The motor is magnetized (for this step, only the flux imposing system and the current controller are validated, the imposed torque to active current converter block and the speed controller being inhibited);
- The traction motor is accelerated to 2500 rpm and the stationary regime is obtained;
- The motor is decelerated to 1000 rpm.

The relevant quantities had been recorded by the DS1103 and saved as Matlab workspace file. The recorded signals were subsequently analyzed in Matlab.

As stated, the first step of the experiment consisted in accelerating toe traction motor to twice the rated speed, when the motor is magnetized. For this, the two validation signals are set one by one (the torque and speed subsystems are manually validated when the motor is magnetized. The motor imposed/assumed flux is illustrated in Fig. 5. The imposed flux reaches the steady state value (motor rated flux) in 1 s. For this, the d axis-imposed current is given in Fig. 6. The necessary current in order to obtain 2.76 Wb is 277 A.

After another 3 s, after the motor flux reaches the steady state value, the speed control subsystem is validated, and the first imposed speed of 2474 rpm is established. The imposed speed increases linearly from close to 0 to the steady state value in 20 s. The first interesting thing is that when the motor is only magnetized (the first 4 s of the experiment), although the imposed q axis current is null (Fig. 8.), more than that, the speed control subsystem is inhibited, the motor real speed is not null, but about 72 rpm. The fact that the motor was not driven at this time is further confirmed by the estimated electromagnetic torque, presented in Fig. 9.

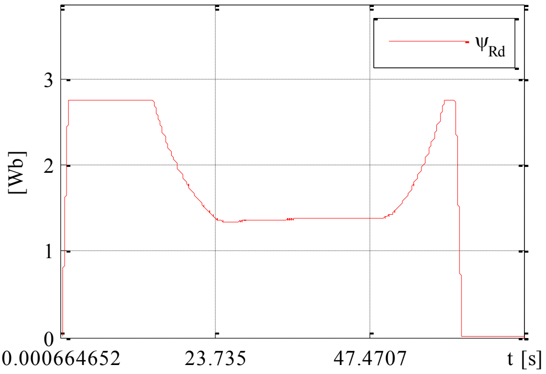

Fig. 5. The motor imposed flux

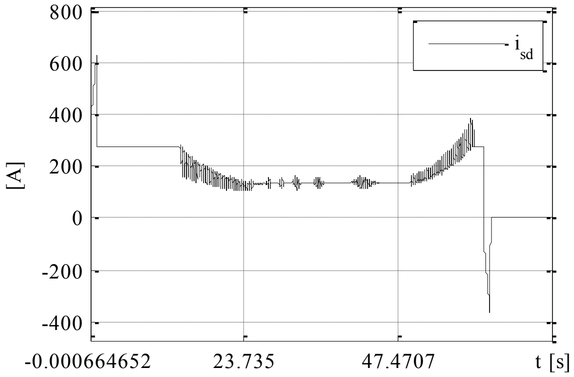

Fig. 6. Imposed d axis current

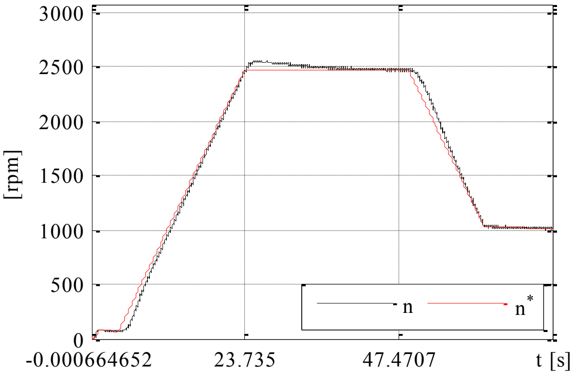

Fig. 7. Motor speed

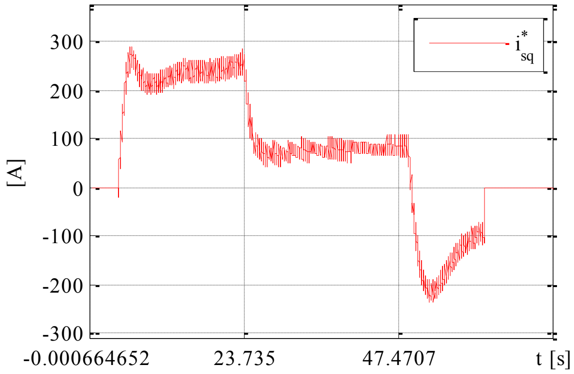

Fig. 8. Motor imposed q axis current

It must be mentioned that the speed controller was designed to have the imposed speed equal to the real speed when the controller is inhibited, so the initial imposed speed is not null, but equal to the real speed of 72 rpm.

The motor speed catches up with the imposed value, although an overshoot of about 3% is noted. An important fact is that the traction motor is driven idle. The steady state q axis current is 75 A. The settling time is about 15 s.

It can be seen that above the motor rated speed, the flux is diminished (the d axis-imposed current is corrected with the speed).

After the steady state regime is settled, the imposed speed is reduced to 1000 rpm. The imposed q axis current becomes negative (as well as the estimated torque), as the motor enters the electromagnetic braking regime. Again, the motor speed follows the imposed speed. The motor estimated flux (given by the d axis current) increases to the motor rated value, as the speed decreases to and below the rated speed.

The motor current magnitude is illustrated in Fig. 10. It results that the current control is good, but the current controller is somewhat slow, and the fast transients of the imposed current are missed. Although, the motor performance (respective to the speed) is not affected.

Looking at the current controller output signal (Fig. 11. – the amplitude modulation index), it results that the traction system has sufficient power reserve.

It must be mentioned that at 61th second (experiment time) the system is manually powered off (by resetting the two validation signals).

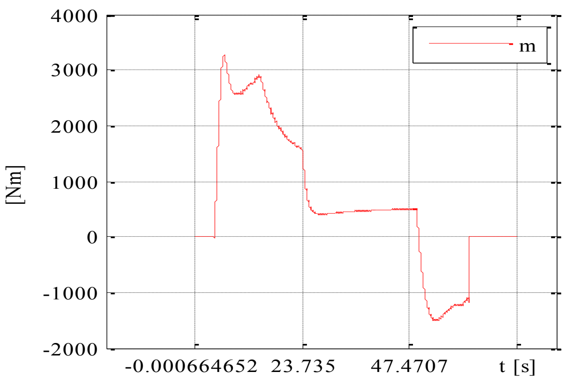

Fig. 9. The estimated electromagnetic torque

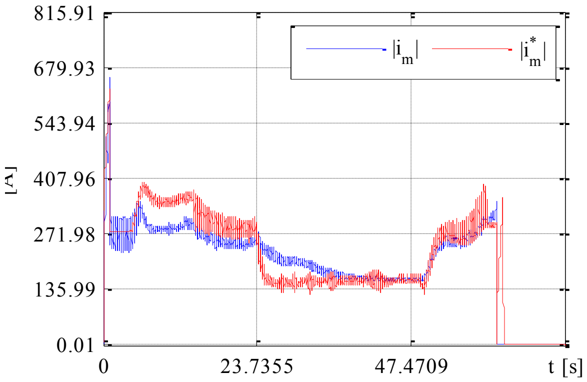

Fig. 10. The motor current magnitude

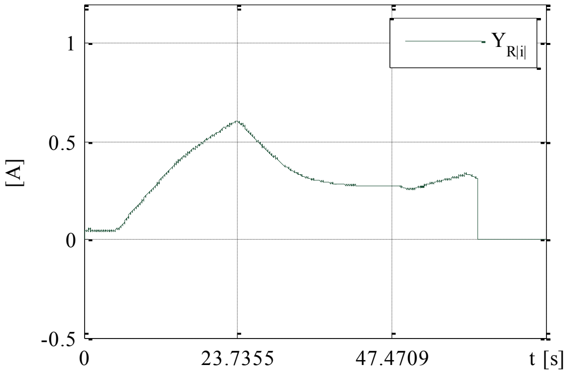

Fig. 11. The current magnitude controller output

CONCLUSIONS

The simplified rotor field-oriented control system was successfully validated on the experimental full scale traction system with good speed regulation results, given the fact that the orientation is only assumed. The filed weakening regime is also obtained with good performance. The DSP sample time for the experiment was 40 µs, but the control algorithm can be used with equally good results with sample times as high as 100 µs. The speed control was good even more so as the idle motor control is difficult. The drawback of the control system is given by the fact that the motor tends to rotate at low speed, when only magnetized, even the fact that the q axis current is null (and the entire speed and torque subsystem is inhibited). This happens also due to the fact that the motor is idle (so the resistant torque is low), which is not the case of a heavy railway vehicle.

Source of research funding in this article: Research program of the Electrical Engineering Department financed by the University of Craiova.

Contribution of authors:
First author – 25%
First coauthor – 25%
Second coauthor – 25%
Third coauthor – 25%

Received on September 28, 2025
Editorial Approval on December 5, 2025

REFERENCES

[1] S. Pancorbo, G. Ugalde, J. Poza and E. A, "Comparative study between induction motor and Synchronous Reluctance Motor for electrical railway traction applications," in 2015 5th International Electric Drives Production Conference (EDPC), Nuremberg, 2015, pp. 1-5, doi: 10.1109/EDPC.2015.7323219.

[2] H. Yamashita, "A traction control method for slip suppression of electric locomotives driven by parallel-connected dual induction motors controlled by one inverter," in 2016 International Conference on Electrical Systems for Aircraft, Railway, Ship Propulsion and Road Vehicles & International Transportation Electrification Conference (ESARS-ITEC), Toulouse, 2016, pp. 1-6, doi: 10.1109/ESARS-ITEC.2016.7841429.

[3] J. Tang, Y. Yang, L. Diao, J. Chen, Y. Chang and Z. Liu, "Parameter identification of induction motors for railway traction applications," in 2018 IEEE Energy Conversion Congress and Exposition (ECCE), Portland, 2018, pp. 284-288, doi: 10.1109/ECCE.2018.8557866.

[4] R. Gomez, L. Pugliese, W. Silva, C. Souse, G. Rezende and F. Rodor, "Speed control with indirect field orientation for low power three-phase induction machine with squirrel cage rotor," *Machines*, vol. 9, no. 12, p. 24, 2021, doi: 10.3390/machines9120320.

[5] M. Ergen and E. Afacan, "Optimizing control of railway traction motor performance with a hardware-in-the-loop method," in 2024 11th International Conference on Electrical and Electronics Engineering (ICEEE), Marmaris, 2024, pp. 101-106, doi: 10.1109/ICEEE62185.2024.10779283.

[6] A. Bitoleanu, M. Popescu and C. Suru, "Experimental performances of the battery charging system of an autonomous locomotive," 2022 22nd International Symposium on Electrical Apparatus and Technologies (SIELA), Bourgas, Bulgaria, 2022, pp. 1-4, doi: 10.1109/SIELA54794.2022.9845794.

[7] CV. Suru, A. Bitoleanu, M. Popescu, M. Linca and F. Ravigan, "Particularities of rotor field orientation control implementation on industrial DSP systems," *Revue Roumaine des Sciences Techniques — Série Electrotechnique et Energétique*, vol. 70, no. 1, 2025, doi: https://doi.org/10.59277/RRST-EE.2025.1.3.

[8] M. Sulaiman, F. Patakor and Z. Ibrahim, "DSP based implementation of field oriented control of three-phase induction motor drives," *IJRET: International Journal of Research in Engineering and Technology*, vol. 2, no. 9, pp. 179-186, 2013.

[9] "DS1103 PPC Controller Board, Features, Release 5.2 – December 2006," dSPACE GmbH, 2006.

[10] M. Linca, C. Suru, M. Popescu and A. Bitoleanu, "Rotor field quasi-oriented control algorithm implementation for railway traction systems on dSPACE DS1103," in 2024 International Conference on Applied and Theoretical Electricity (ICATE), Craiova, 2024, pp. 1-6, doi: 10.1109/ICATE62934.2024.10748608.

[11] M. Popescu and A. Bitoleanu, "New achievements in the rotor field-oriented control for autonomous locomotives: Part 1: System synthesis and theoretical investigations," in 2021 7th International Symposium on Electrical and Electronics Engineering (ISEEE), Galati, 2021, pp. 1-6, doi: 10.1109/ISEEE53383.2021.9628690.

[12] A. Kelemen and M. Imecs, *Field-Oriented Control Systems for Alternating Current Machines*, Bucharest: Academiei, 1989.

[13] “ControlDesk Next Generation Reference For ControlDesk 5.3Release 2014 B – November 2014," dSPACE GmbH, 2014.

Annals of the University of Craiova, Electrical Engineering series, No. 49, Issue 1, 2025; ISSN 1842-4805 eISSN 2971-9852

DOI: 10.52846/AUCEE.2025.07

Implementation and Experimental Validation of Shunt Active Filter Control Strategies on dSPACE Prototyping System

Mihăiță-Daniel Constantinescu*, Mihaela Popescu*, Mihăiță Lincă*, Florin Ravigan*, Ionuț-Cosmin Toma*
*University of Craiova, Faculty of Electrical Engineering, Craiova, Romania, mconstantinescu@em.ucv.ro,
ORCID: 0009-0001-5674-8195
*University of Craiova, Faculty of Electrical Engineering, Craiova, Romania, mpopescu@em.ucv.ro,
ORCID: 0000-0002-5292-5529
*University of Craiova, Faculty of Electrical Engineering, Craiova, Romania, mlinca@em.ucv.ro,
ORCID: 0009-0009-7727-3684
*University of Craiova, Faculty of Electrical Engineering, Craiova, Romania, ravigan.florin@gmail.com,
ORCID: 0009-0001-5138-4863
*University of Craiova, Faculty of Electrical Engineering, Craiova, Romania, ctoma@em.ucv.ro,
ORCID: 0009-0008-3965-3857

Abstract - **This paper presents a comparative analysis of control strategies applied to active power filtering, aiming to compensate a nonlinear three-phase load with a current of 20 A per phase. The study focuses on the comparison between direct power control (DPC) and indirect current control, analyzed in two distinct configurations: (i) reference current calculation based solely on the voltage regulator, and (ii) reference current calculation including the active component of the load current. The active power filter system is modeled and simulated in the Matlab/Simulink environment and subsequently implemented in real time on the dSPACE DS1103 platform for experimental validation. The evaluations are carried out under identical load conditions, allowing for a relevant and fair performance comparison. Experimental results highlight the ability of both strategies to reduce harmonic distortions and compensate reactive power, while showing notable differences in terms of total harmonic distortion (THD), DC-link voltage stability, and dynamic response to load variations. The comparative analysis provides a clear perspective on the advantages and limitations of each method, emphasizing the impact of the reference current calculation approach on the overall performance of the active power filter and its relevance for practical power quality compensation applications.**

Cuvinte cheie: *filtru activ de putere, control direct al puterii (DPC), control indirect al curentului, sarcină neliniară trifazată, factor total de distorsiune armonică (THD), compensarea puterii reactive, implementare în timp real.*

Keywords: *active power filter, direct power control (DPC), indirect current control, nonlinear three-phase load, total harmonic distortion (THD), reactive power compensation, real-time implementation.*

I. INTRODUCTION

The increasing use of power-electronic-based equipment has led to a proliferation of nonlinear loads in distribution networks, generating harmonic and reactive currents that degrade power quality, increase system losses, and affect the operation of sensitive equipment [1], [2].

Active Power Filters (APFs) have emerged as an effective solution for compensating harmonic and reactive currents, offering superior performance compared to passive filters and rapid adaptability to load variations [3]-[6]. The performance of an APF strongly depends on the control strategy employed.

This paper focuses on a comparative analysis between indirect current control (CI) and direct power control (DPC), two efficient methods for active power filtering [7]-[12,], [16], [17]. Indirect current control is investigated in two configurations: (i) with the reference current calculated solely from the DC-link voltage regulator, and (ii) with the reference current calculated based on the active load current [16].

The system is modeled and simulated in Matlab/Simulink and implemented in real time on the dSPACE DS1103 platform [13]–[15]. The comparative analysis evaluates the performance of both strategies in terms of harmonic reduction, reactive power compensation, and dynamic response, providing relevant conclusions for practical applications in power quality improvement.

II. THEORETICAL BACKGROUND

Nonlinear loads degrade power quality by introducing harmonics, reactive power, and voltage distortion. Unlike passive filters, active power filters use power electronics to inject controlled compensating currents, maintaining nearly sinusoidal supply currents in phase with the grid voltage and thus reducing THD.

A. Concept of Indirect Current Control

Indirect current control (ICC) is an effective method for operating APFs by regulating the reference compensating current calculated from the DC-link voltage and/or the active load current. The ICC principle is illustrated in the block diagram in Fig. 1 [6], [13]-[20], where:

- I.F. – interface filter;
- TU – voltage transducer;

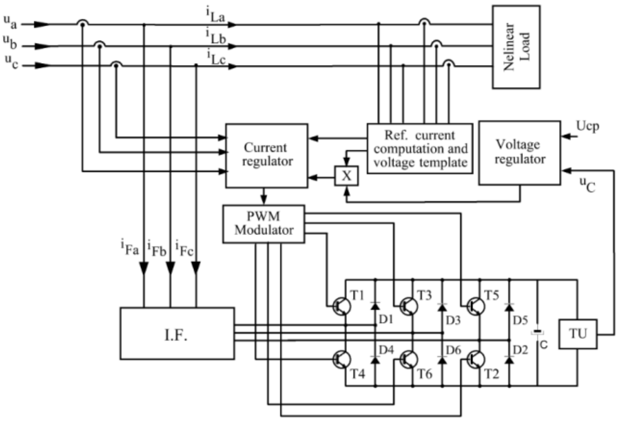

Fig. 1. Single-line diagram of a parallel three-phase active power filter with indirect current control.

- X – multiplication block which multiplies the voltage controller output with the voltage template.

In this work, ICC has been implemented on the dSPACE DS1103 platform, ensuring sinusoidal supply currents in phase with the grid voltage while effectively compensating harmonic and reactive components.

B. *Direct Power Control*

The Direct Power Control algoritm its described in Fig.2.

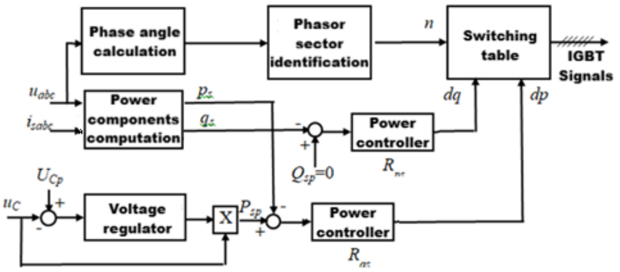

Fig. 2. Block diagram for direct power control

The power components (instantaneous active and reactive powers, p and q) are computed from the supply voltages and the grid currents. The reference reactive power is set to zero in order to ensure reactive power compensation, whereas the reference active power is defined as the product of the voltage controller output and the DC-link voltage across the compensation capacitor (Fig. 2). The power controllers are implemented as hysteresis-band controllers [17].

In the design of the switching table, twelve sectors corresponding to the possible positions of the voltage space vector in the fixed (α,β) reference frame are considered, as a function of the angle θ (Fig. 3).

TABLE I.
SWITCHING TABLE FOR THE ADOPTED DPC [17]

dp	dq	θ_1	θ_2	θ_3	θ_4	θ_5	θ_6	θ_7	θ_8	θ_9	θ_{10}	θ_{11}	θ_{12}
1	0	101	111	100	000	110	111	010	000	011	111	001	000
	1	111	111	000	000	111	111	000	000	111	111	000	000
0	0	101	100	100	110	110	010	010	011	011	001	001	101
	1	100	110	110	010	010	011	011	001	011	101	101	100

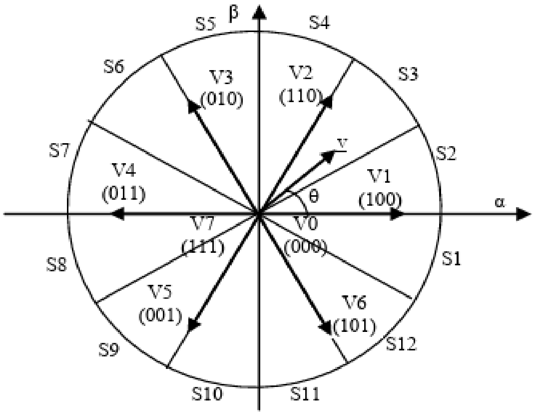

Fig. 3. Sectors and voltage vectors in the stationary reference frame [17]

Based on the outputs dp and dq of the hysteresis controllers and on the identified sector number (n) of the voltage vector, the inverter transistor switching states are determined according to the adopted switching table (Table I).

III. MODELING OF THE ACTIVE FILTERING SYSTEM

A. *Modeling of the Active Filtering System in the Case of Indirect Current Control*

The gating signals for the inverter transistors are generated by the three-phase hysteresis current regulator. The reference current is obtained in two variants:

- from the voltage controller – the reference currents are obtained by multiplying the output of the voltage controller with the voltage template (three-phase unitary amplitude signals synchronized with the grid voltages, given by the phase locked loop, PLL) (Fig. 4);
- from the load active current – the reference current are obtained by the sum of two components (Fig. 5):
    - o the active filter charging current – obtained like in the previous case;
    - o the load active current – obtained from the load computed active power.

The advantage of the second control system is given by the fact that the voltage controller output gives the amplitude of the active filter charging current and not the amplitude of the current absorbed from the grid by the entire active filtering system like in the first control system. This is because the controller output ripple is much smaller, given the fact that the output magnitude is smaller. This way the distortion introduced by the voltage controller itself two the compensated current is reduced [21]-[24].

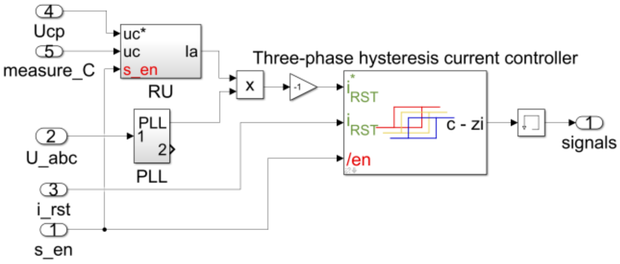

Fig. 4. Block structure in the case of indirect control with the reference current computed solely from the voltage controller

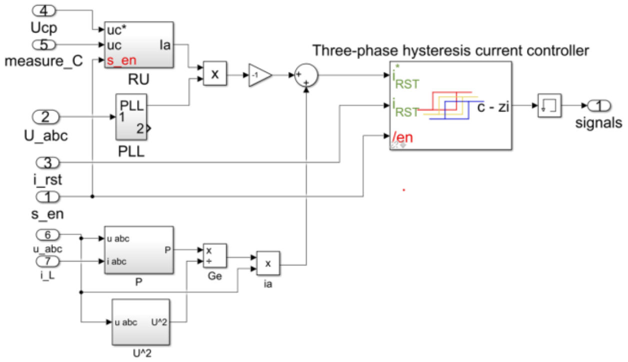

Fig. 5. Block structure in the case of indirect control with the computation of the load active current

B. *Modeling of the Active Filtering System in the Case of Direct Power Control*

For direct power control, the Simulink model developed based on the principles of the method is shown in Fig. 6. The instantaneous active and reactive powers are calculated using the supply voltages and the grid currents, inside the block “Calculation of , and ϕ”, which also provides the phase angle, θ (Fig. 7). The sector number corresponding to the position of the voltage space vector is obtained at the output of the “Sector Determination” block (Fig. 8).

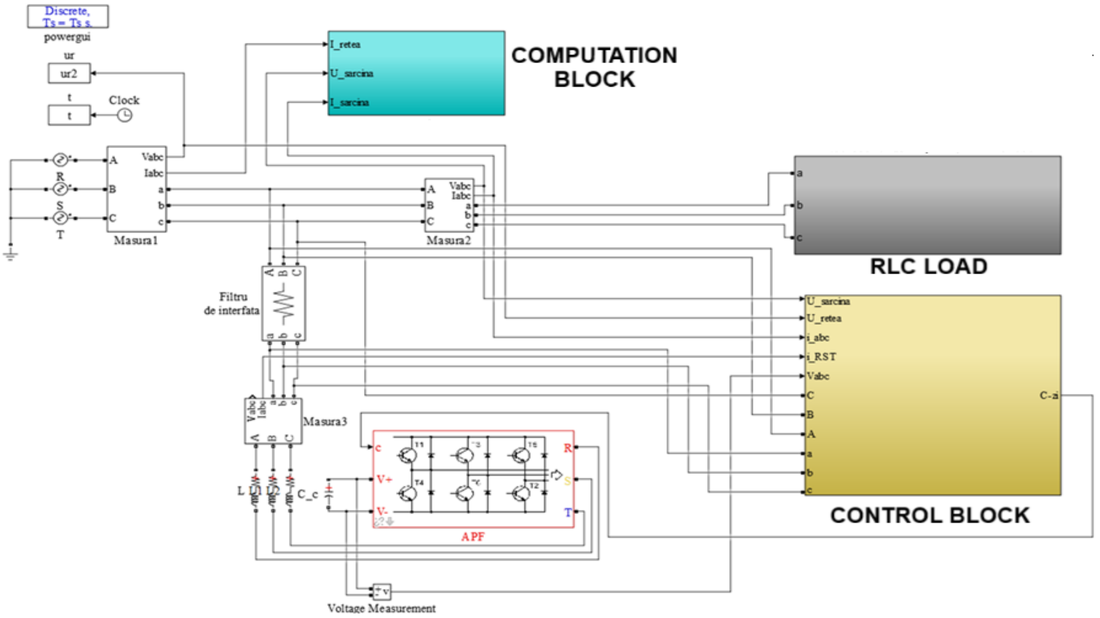

Fig. 6. Simulink model of the whole active filtering system.

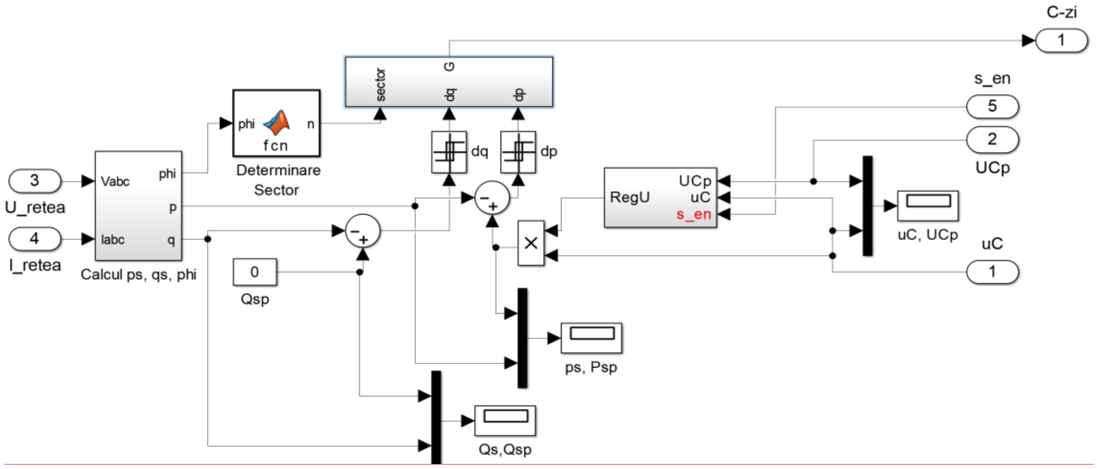

Fig. 7. SIMULINK model of the control block for Direct Power Control

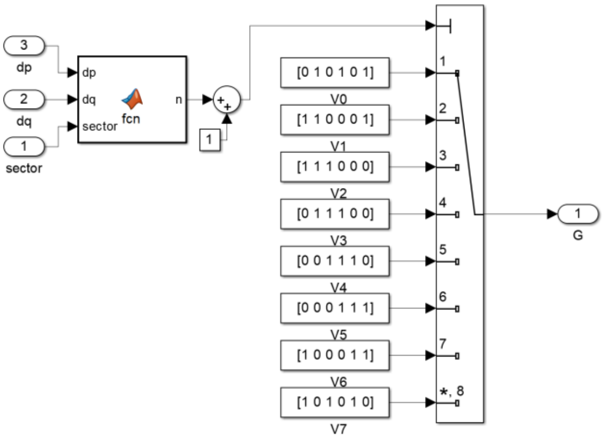

Fig. 8. SIMULINK model of the transistor gate control block based on the outputs of the hysteresis controllers and the identified sector number

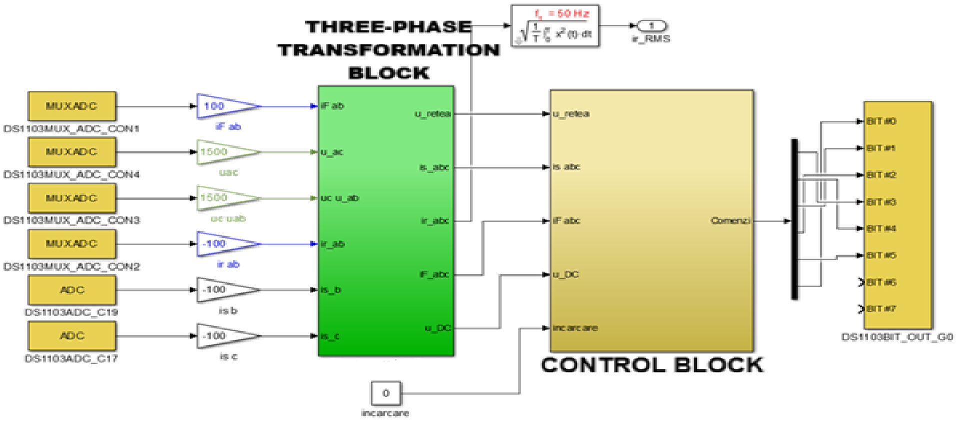

Fig. 9. The real-time control SIMULINK block of the active power filter.

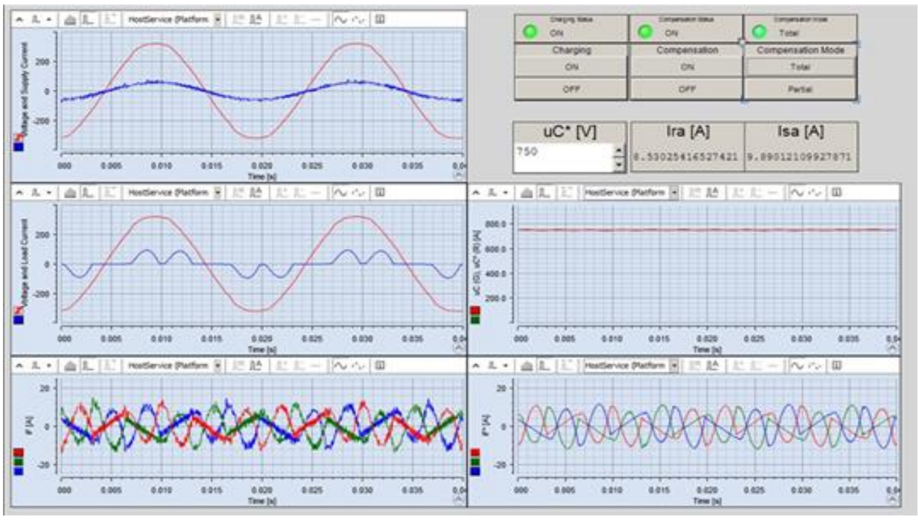
Charging Status ON
Compensation Status ON
Compensation Mode Total

uC* [V]: 750

Ira [A]: 8.53025416527421

Isa [A]: 9.89012109927871

Fig. 10. The virtual ControlDesk panel for the active power filter control.

IV. EXPERIMENTAL VALIDATION

The development of the SIMULINK control model of the experimental active power filter is based on extracting the control algorithm sub-model of the virtual active filter from the active filtering system complete model (presented in Section III), and replaceing the virtual power-section with the dSpace library blocks. These blocks are the link between the dSpace board hardware resources and the SIMULINK environment. Accordingly, the SIMULINK control model of the active power filter is shown in Fig. 9.

To achieve the real-time execution machine code, the control model was compiled with the sampling time of 30 μs. This value represents a compromise between accuracy and computational load, given the complexity of the implemented algorithms.

The virtual control panel developed for this approach, in ControlDesk NG is illustrated in Fig. 10.

To evaluate the performance of the active filtering system, the operating point was set for a load current of 20 A RMS.

A. Active Filtering System in the Case of Indirect Current Control

1) Active Filtering System under Indirect Current Control Based on the Reference Current Computed Solely from the Voltage Controller

The voltage and current waveforms for phase 'a' drawn from the grid by the active filtering system, had been measured with a Tektronix TPS2024 oscilloscope (Fig. 11). The current was measured with the Fluke 80i-500s Current clamp (1mV/1A transfer ratio). The same quantities had been acquired with the dSpace board analog to digital converters and ploted in MATLAB (Fig. 12).

Fig. 13 shows the harmonic spectrum of the grid current under total p–q compensation for a 20 A load current. The current THD for phase 'a' is 5.25%, and for phases 'b' and 'c' is 5.8% and 5.81%..

Furthermore, the comparison between the oscilloscope and dSPACE measurements shows good agreement, with minor differences mainly due to sampling and signal conditioning. The harmonic spectrum confirms the effectiveness of the p–q compensation strategy, reducing the grid current distortion and ensuring a nearly sinusoidal waveform. The similar THD values across all phases indicate balanced operation and stable controller performance.

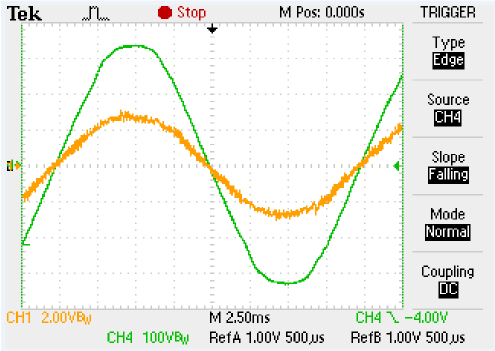

Fig. 11. Experimental voltage (green) and current (orange) waveforms at the grid side sampled with the Tektronix oscilloscope. TPS2024

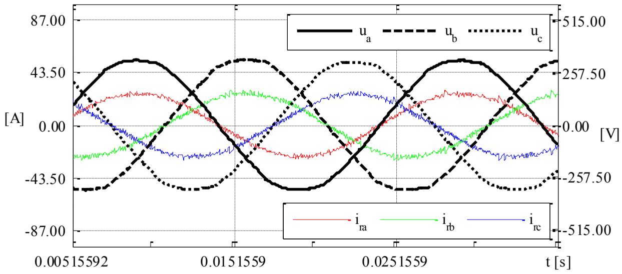

Fig. 12. Grid voltage and current waveforms sampled with the dSpace DS1103 ADCs.

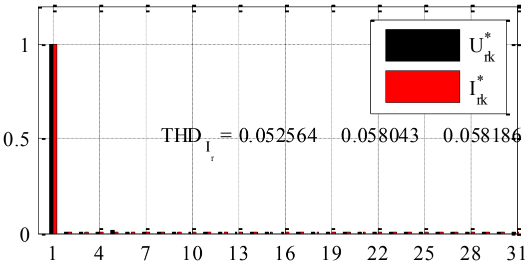

Fig. 13. Harmonic spectrum of phase voltage and grid current.

2) Active Filtering System under Indirect Current Control Based on the Computation of the Load Active Current

For this case, the grid voltage and compensated current are illustrated in Fig. 14 (sampled with the Tektronix TPS2024 digital oscilloscope) and in Fig. 15 (sampled with the dSpace board analog to digital converters and ploted in MATLAB, respectively).

Fig. 16 shows the harmonic spectrum of the grid current under total p–q compensation for the same load. The current THD for phase 'a' is 5.63%, and for phases 'b' and 'c' it is 4.92% and 5.2%, respectively.

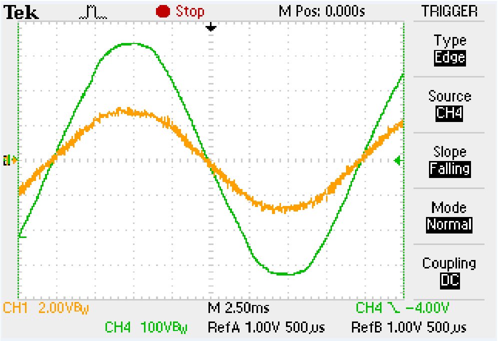

Fig. 14. Experimental voltage (green) and current (orange) waveforms at the grid, for phase 'a', acquired with a Tektronix TPS2024

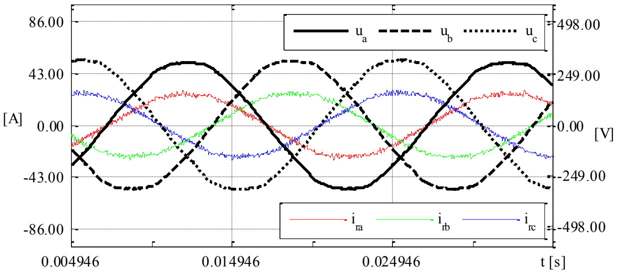

Fig. 15. Grid voltage and current waveforms

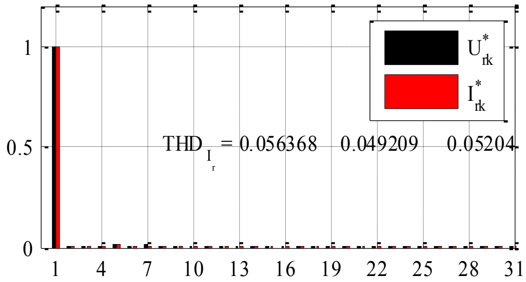

Fig. 16. Harmonic spectrum of phase voltage and grid current.

B. *Active Filtering System in the Case of Direct Power Control*

The Tektronix TPS2024 oscilloscope screen in Fig. 17 shows the grid voltage and current waveforms for phase 'a'. Fig. 18 shows the phase voltages and currents at the grid side after total compensation for a 20 A load current, sampled by the dSpace board. Fig. 19 presents the harmonic spectrum of phase 'a' grid current and phase voltage. The phase current THD values are: phase 'a' – 5.82%, phase 'b' – 5.79%, and phase 'c' – 5.56%.

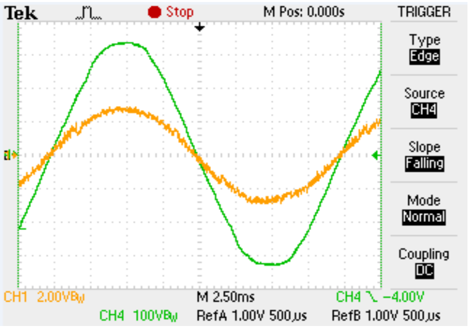

Fig. 17. Experimental voltage (green) and current (orange) waveforms at the grid, for phase 'a', acquired with a Tektronix TPS2024

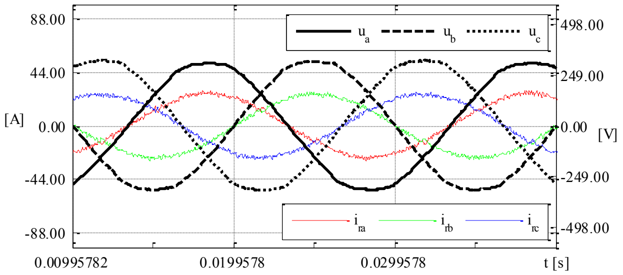

Fig. 18. Grid voltage and current waveforms.

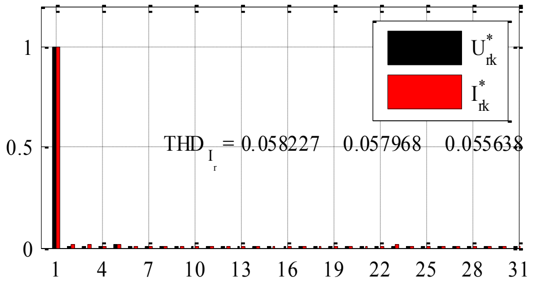

Fig. 19. Harmonic spectrum of phase voltage and grid current.

Table II summarizes the performance of three control methods applied to the active power filter under total compensation conditions: the classical indirect current control (Yvc), the indirect current control based on the active component of the load current (Iac), and the direct power control (DPC).

TABLE II. PERFORMANCE COMPARISON FOR A LOAD CURRENT OF 20 A

Control Method	**Compensation Strategy**	**EF$_{avr}$**	**η [%]**	**PF**
Yvc	Total Compensation	7,51	95,98	0,997
Iac		**7,9**	**97,17**	0,997
DPC		7,32	96,94	**0,998**

The classical indirect current control (Yvc), in which the reference grid current amplitude is generated exclusively by the compensating capacitor voltage controller, achieves an average filtering efficiency (EFavr of 7.51, an overall efficiency of 95.98%, and a power factor of 0.997. Although this strategy ensures stable operation and near-unity power factor, its filtering performance and efficiency are slightly inferior compared to the other investigated methods.

The indirect current control strategy based on the active component of the load current (Iac), where the reference grid current amplitude is obtained by combining the active component of the load current with the output of the compensating capacitor voltage controller, exhibits the best overall performance. This method achieves the highest average filtering efficiency (EFavr = 7.9) and the highest system efficiency (97.17%), while maintaining a power factor of 0.997. These results indicate an improved harmonic compensation capability and reduced power losses.

The direct power control (DPC) method provides the highest power factor (0.998), demonstrating superior control of active and reactive power exchange with the grid. However, its average filtering efficiency (EFavr = 7.32) is slightly lower than that obtained with the indirect current control strategies, although the overall efficiency remains high (96.94%).

Overall, all three control methods ensure effective total compensation, with power factor values close to unity and efficiencies exceeding 95%. Among them, the Iac-based indirect current control offers the best compromise between filtering performance, efficiency, and power factor, making it a suitable candidate for high-performance active power filter applications.

V. CONCLUSIONS

The performance obtained by the classical indirect current control, in which the reference grid current amplitude is generated exclusively by the compensating capacitor voltage controller is the lowest of the three investigated methods given the high effect of the voltage controller output rippler in the reference current. The indirect current control strategy based on the active component of the load current, exhibits the best overall performance, achieving the highest average filtering efficiency and the highest system efficiency. The direct power control method provides the highest power factor, demonstrating superior control of active and reactive power exchange with the grid.

Overall, all three control methods ensure effective total compensation, with power factor values close to unity and efficiencies exceeding 95%.

ACKNOWLEDGMENT

The authors would like to acknowledge the support provided by INCESA, within Laboratory 103 – Active Filtering and High-Performance Static Converters, where the experimental measurements and determinations were carried out. The work was conducted within the same research group, and the authors appreciate the technical assistance and collaborative environment provided by the laboratory staff. This work was supported by the Research

Program of the Electrical Engineering Department, financed by the University of Craiova.

Contribution of authors:
First author – 30%
Second author – 25%
Third author – 15%
Fourth author – 15%
Fifth author – 15%

Received on September 27, 2025
Editorial Approval on December 10, 2025

REFERENCES

[1] H. Sasaki, T. Machida, “A new method to eliminate AC harmonic currents by magnetic flux compensation-Considerations on basic design,” *IEEE Trans. Power Appar. Syst*., vol. PAS-90, no. 5, pp. 2009-2019, Sept. 1971, doi: 10.1109/TPAS.1971.292996.

[2] L. Gyugyi, E. Strycula, “Active AC Power Filters,” Proc. IEEE/IAS Annual Meeting, 1976.

[3] H. Akagi, Y. Kanazawa, A. Nabae, “Instantaneous reactive power compensators comprising switching devices without energy storage components,” *IEEE Trans. Ind. Appl*., vol. IA-20, no. 3, pp. 625-630, May 1984, doi: 10.1109/TIA.1984.4504460.

[4] J. L. Afonso, M. Tanta, J. G. O. Pinto, L. F. C. Monteiro, L. Machado, T. J. C. Sousa, V. Monteiro, “A review on power electronics technologies for power quality improvement,” *Energies*, vol. 14, no. 8585, 2021, doi: 10.3390/en14248585.

[5] S. R. Das, P. K. Ray, A. K. Sahoo, S. Ramasubbareddy, T. S. Babu, N. M. Kumar, R. M. Elavarasan, L. Mihet-Popa, “A comprehensive survey on different control strategies and applications of active power filters for power quality improvement,” *Energies*, 14(15) : 4589, 2021, doi: 10.3390/en14154589.

[6] D. Buła, M. Zygmanowski, “Control strategies applied to active power filters,” *Energies*, 15(7), 2408, 2022, doi: 10.3390/en15072408.

[7] H. Akagi, E. H. Watanabe and M. Aredes, *Instantaneous Power Theory and Applications to Power Conditioning*, Hoboken: Wiley-IEEE Press, NJ, 2007.

[8] R. S. Herrera, P. Salmeron, H. Kim, “Instantaneous reactive power theory applied to active power filter compensation: different approaches, assessment, and experimental results,” *IEEE Trans. Ind. Electron*., vol. 55, no. 1, pp. 184-196, Jan. 2008, doi: 10.1109/TIE.2007.905959.

[9] P. Dey, S. Mekhilef, “Synchronous reference frame based control technique for shunt hybrid active power filter under non-ideal voltage,” IEEE ISGT Asia, Kuala Lumpur, Malaysia, 2014, pp. 481-486, doi: 10.1109/ISGT-Asia.2014.6873839.

[10] S. Sahadev and B. Manju, “Performance analysis of SRF based SAPF with PI and Fuzzy controllers,” 2015 International Conference on Control Communication & Computing India (ICCC), 2015, pp. 260-264, doi: 10.1109/ICCC.2015.7432902.

[11] P. Tenti, “Conservative Power Theory - A theoretical background to understand energy issues of electrical networks under non-sinusoidal conditions and to approach measurement, accountability and control problems in smart grids,” UNICAMP – UNESP Sorocaba, Aug. 2012.

[12] M. D. Constantinescu, M. Popescu, C. V. Suru, “Implementation of Conservative Power Theory in the control of active power filters,” *Annals of Faculty Engineering Hunedoara – International Journal of Engineering*, Tome XX, Fascicule 3, 2022, pp. 49-54.

[13] C. V. Suru, A. Bitoleanu, *Sisteme DSP-dSPACE aplicate în electronica de putere* (in Romanian), Bucharest: Matrix Rom, 2021.

[14] DS1103 PPC Controller Board – Hardware Installation and Configuration, Release 5.2 – December 2006.

[15] DS1103 PPC Controller Board, RTI Reference, Release 5.2 – December 2006.

[16] M. D. Constantinescu, M. Popescu, and C. V. Suru, “Comparative analysis of two methods of calculating the prescribed current in a shunt active filtering system,” *Annals of the University of Craiova, Electrical Engineering Series*, no. 45, issue 1, 2021, pp. 46-51, doi: 10.52846/AUCEE.2021.1.07.

[17] M. D. Constantinescu, M. Popescu, G.-E. Subțirelu, and I.-C. Toma, “Modelling, simulation and implementation on dSpace 1103 of the Direct Power Control in a three-phase shunt active power filter system,” *Annals of the University of Craiova, Electrical Engineering Series*, no. 47, issue 1, 2023, doi: 10.52846/AUCEE.2023.11.

[18] P. Tenti and P. Mattavelli, “A time-domain approach to power term definitions under non-sinusoidal conditions,” Proc. 6th Int. Workshop on Power Definitions and Measurements under Non-Sinusoidal Conditions, Milano, Oct. 13–15, 2003.

[19] P. Tenti, P. Mattavelli, and E. Tedeschi, “Compensation techniques based on reactive power conservation,” *Electrical Power Quality and Utilisation, Journal*, vol. XIII, no. 1, 2007.

[20] A. Pătrașcu, M. Popescu, and V. Suru, “The Conservative Power Theory and the active filtering,” *Bulletin AGIR*, no. 4, pp. 179–182, 2012.

[21] C. V. Suru, A. Pătrașcu, M. Popescu, and A. Bitoleanu, “Conservative Power Theory application in shunt active power filtering under asymmetric voltage,” Proc. 14th Int. Conf. on Optimization of Electrical and Electronic Equipment (OPTIM), pp. 647–654, 2014, doi: 10.1109/OPTIM.2014.6850998.

[22] A. Preda, M. Popescu, and M. Linca, “Conservative Power Theory (CPT) method applied in the indirect current control for active D.C. traction substations,” ATINER’s Conference Paper Series, no. TRA2015-1561, Athens, Greece, pp. 1–17, Aug. 2015.

[23] H. K. Morales Paredes, A. Costabeber, and P. Tenti, “Application of conservative power theory to cooperative control of distributed compensators in smart grids,” *Przegląd Elektrotechniczny* (Electrical Review), vol. 87, no. 1, 2011.

[24] A. Bitoleanu, M. Popescu, and V. C. Suru, *Filtre active de putere – Fundamente și aplicații* (in Romanian) București: Matrix, Romania, 2021.

Annals of the University of Craiova, Electrical Engineering series, No. 49, Issue 1, 2025; ISSN 1842-4805 eISSN 2971-9852

DOI: 10.52846/AUCEE.2025.08

Study on the Energy and Economic Efficiency of a Hot Air Heating System in an Industrial Hall

Radu-Cristian Dinu*, Felicia-Elena Stan-Ivan*, Adelaida-Mihaela Duinea*, Gabriel-Cosmin Buzatu*
* University of Craiova / Faculty of Electrical Engineering, Craiova, Romania, e-mail: rcdinu@elth.ucv.ro, ORCID: 0009-0001-9234-9933
* University of Craiova / Faculty of Electrical Engineering, Craiova, Romania, e-mail: fivan@elth.ucv.ro, ORCID: 0009-0009-1101-2369
* University of Craiova / Faculty of Electrical Engineering, Craiova, Romania, e-mail: aduinea@elth.ucv.ro, ORCID: 0009-0008-6309-547X
* University of Craiova / Faculty of Electrical Engineering, Craiova, Romania, e-mail: cbuzatu@elth.ucv.ro, ORCID: 0009-0008-2099-4336

Abstract – **When heating an industrial hall-type building, the following types of heat demand must be considered: for heating, for domestic hot water preparation, for ventilation, for technological purposes, and for losses related to transport and distribution. This paper analyzes aspects related to the heat demand for heating an industrial hall, starting from the existing situation (heating with static radiators, with hot water as the heat transfer medium taken from the urban heating network at a price of approximately 718 lei/Gcal) and rethinking the decentralized hot air heating system with wall-mounted air heaters. Generally, heat requirements are based on a simplified estimate, the accuracy of which depends on the designer's experience in the field. In this paper, the energy performance of the industrial hall analyzed was assessed taking into account the methodologies specified in the regulations. The particularities related to the building's purpose (industrial building), the climatic zone in which the building is located, and the specific features of the type of heating system used (static bodies or wall-mounted air heaters) were taken into account. All these particularities are explicitly specified in the chapter dedicated to the case study, which makes the issues discussed easier to understand.**

Cuvinte cheie: *hală industrială, energie termică, încălzire, aer cald, sistem*

Keywords: *industrial hall, thermal energy, heating, hot air, system*

I. INTRODUCTION

As a rule, the concept of energy is linked to the type of buildings and the installations inside them, so there are increasingly frequent concerns aimed at solving some problems related to the energy efficiency of buildings.

Among these concerns, the most common are:

- reducing energy consumption in old buildings through technical and economic measures (this is also the case for the industrial building that is the subject of the case study in this paper);
- adopting measures, for new buildings, that will result in both quantifiable energy savings and increased comfort inside them.

In order to quantitatively assess heat transfer phenomena through building elements, it is necessary to know the thermodynamic properties of homogeneous materials, through:

- choosing energy-efficient and thermodynamically efficient building materials;
- checking the thermal and hygrothermal properties of an existing building or one that's being designed.

The method for selecting the appropriate construction elements is determined during the design phase, taking into account the thermal characteristics of the materials used for the purpose of [1]:

- achieving the minimum resistance necessary for heat transfer, which has the effect of reducing heat flow on the one hand and preventing condensation on the inner surface of the building element on the other;
- achieving the thermal stability necessary to avoid air temperature fluctuations inside the space in question and on the inner surface of the building element;
- resistance to vapor permeability that limits the risk of vapor condensation inside the building element;
- resistance to outside air infiltration that ensures the thermal insulation capacity of the interior space in question.

In order to reduce specific heat consumption and, in general, heat consumption for heating, measures are needed to rehabilitate and modernize the thermal protection of buildings and heating installations in residential, administrative, production, and social and cultural buildings [2].

II. HOT AIR HEATING OF BUILDING

In Romania, after the introduction of central heating in residential buildings, systems based on static elements, such as radiators, convectors, and convector radiators, have been used over time [1].

As installation technology has evolved and thermal comfort requirements in buildings have increased, in addition to traditional central heating systems, other types of heating systems have begun to be analyzed, adaptable to both residential and industrial buildings, such as: hot air heating systems and low, medium, and high temperature radiation heating systems [3].

Hot air generators are used to heat industrial spaces, warehouses, and workshops, often being a more cost-effective solution compared to traditional systems that use hot water as a heat transfer medium. In addition to the direct benefits, the fact that they do not require a centralized heating system makes these generators particularly recommended for rooms that are heated occasionally or for limited periods.

The strengths of hot air generators are: compactness, lack of thermal energy, and fast and pleasant heating [3].

The operation of these modern heating systems is based on the following mechanism: a fan ensures air circulation through the heat exchanger, which is heated by the gases burned in the burner. The heat exchanger, made of welded stainless steel, transfers heat to the circulating air. The burners can be of the "atmospheric" or "air-blown" type. The gas is ignited by a high-voltage electric arc, and the flame is controlled by ionization [4].

The equipment is equipped with a combined gas valve that includes a pressure reducer, an electromagnetic valve, a differential pressure switch that shuts off the burner in case of exhaust fan failure, as well as thermostats for limiting and regulating the temperature. The heated air is directed into the room through louvered air diffusers that also direct the airflow. In general, hot air generators are an efficient heating system, suitable for halls and rooms where the technological flow, compartmentalization of spaces, low interior height, or the need for a constant supply of fresh air (such as bathrooms, changing rooms, etc.) make the use of radiation heating impractical [4].

The main hot air heating systems currently in use are: infrared dark heater systems in the vacuum version (fig. 1) and in the overpressure version (fig. 2); tube-generator hot air heating systems; Turbo radiant heating systems; industrial convector heating systems; systems with recovery of energy lost by food refrigeration systems [5].

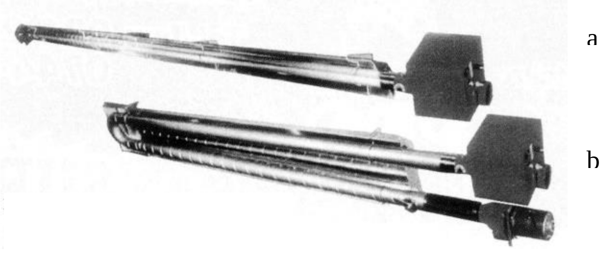

Fig. 1 Dark wave heating system with overpressure operating mode: a) with straight radiant tube; b) with U-shaped radiant tube [3]

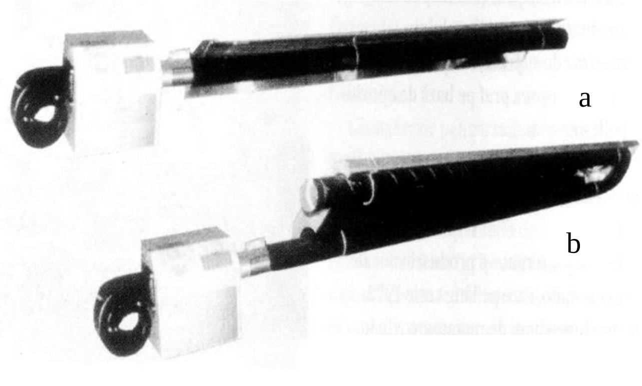

Fig. 2. Dark wave heating system with negative pressure operation and single flue gas exhaust: a) with straight radiant tube; b) with U-shaped radiant tube [6]

For heating halls, it is recommended to combine two types of radiant tubes: dark wave and infrared. To this end, consideration should be given to areas frequently used by staff, the position of machinery (e.g., lathes), electrically operated mobile doors, large glass surfaces, and others. When a comfortable temperature is desired for occupants in a specific area of the room, so-called "warm islands" or zone heating is created, for which infrared radiant tubes are mainly used [7].

Infrared radiant tubes can also be used to reduce the effect of "cold" radiation from large glass surfaces or sliding doors. It is important to note that the intensity of the radiation is not evenly distributed throughout the space, being much stronger in the heated area. The intense circulation of cold air replacing the warm air in the radiated area can cause slight discomfort [8].

If the radiant heat flow comes from a single direction, occupants may experience uneven heat distribution (similar to the "campfire" effect), i.e., "hot in front, cold in back." For this reason, the need to even out the thermal effect must be taken into account when positioning the radiant tubes. The design and implementation of radiant tube heating systems can be flexible in terms of construction and usability, with the possibility of creating both very expensive but inefficient systems and reasonably priced solutions that take into account all relevant technical aspects [8].

III. CONSTRUCTIVE AND ENERGY ANALYSIS OF THE INDUSTRIAL HALL

The studied hall is part of a complex of industrial and administrative buildings located on the northern outskirts of a town in climate zone II. In terms of shelter, it is classified as a moderately sheltered building.

The hall building consists of (fig. 3): The actual hall building on two levels; the administrative building with its facade facing east, on three levels; the administrative building with its facade facing west, also on three levels.

Functionally, the main building (the hall) is intended for industrial activities involving light work with average heat emissions. The administrative buildings are spaces where materials and raw materials, as well as finished products, are stored and where design, research, and other activities are carried out.

The characteristic elements regarding the location of buildings in the built environment are as follows [9]:

- climate zone: II according to the climate zoning map of Romania in SR 1907-1;

- average outdoor design temperature: $t_e = -15^oC$;

- orientation relative to the cardinal points: the main body of the hall with the facades facing north and south;

- wind zone: IV (4.5 m/s), according to the map of localities in wind zones, from SR 1907-1;

- building category in terms of air permeability: permeable building with windows with a high degree of permeability;

- soil temperature value, θ_p, at a depth of 7 m from ground level, depending on the area where the building is located: θ_p=10°C.

Heat losses through the envelope elements of industrial buildings are determined taking into account the dimensions of the building, the design wind speed, the average

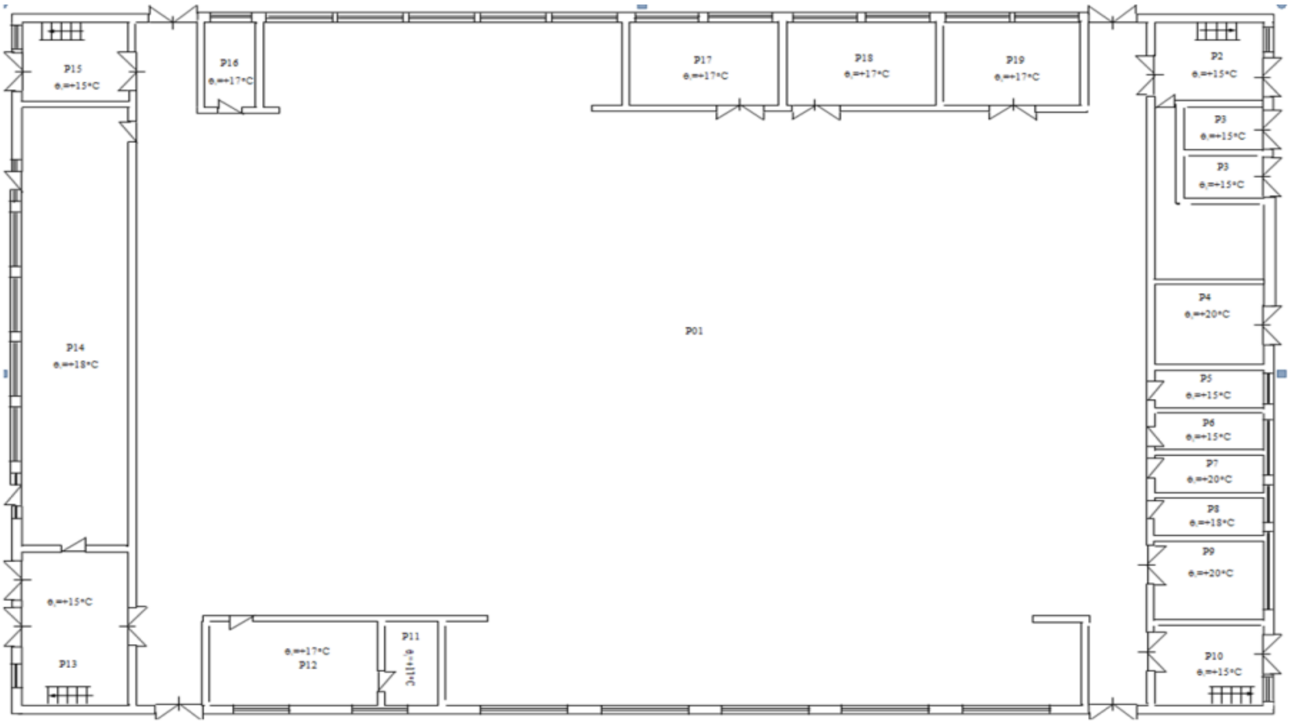

Fig. 3. The section of the industrial hall building

design indoor temperatures specific to each room, depending on its purpose (Table 1), as well as the conventional average outdoor design temperature for a location in climate zone II, $t_e = -15$ºC.

TABLE I.
THE INDOOR DESIGN TEMPERATURES SPECIFIC TO EACH TYPE OF ROOM, DEPENDING ON THEIR INTENDED USE

Nr. crt.	Room destination	Conventional indoor design temperature, [°C]
1.	Plastic injection hall – medium-effort work category	17
2.	Entrance hall, toilets, interior corridors, stairwell	15
3.	Storage rooms, Repair workshop 2, Metrological inspections, Sprinkler room, Assembly lines	18
4.	Bathrooms, Repair workshop 1, Partners' office, Fire safety office, Plastic section manager's office 1, Plastic section manager's office 2, Labels office	20
5.	Changing rooms	22

The heat losses resulting from transmission through the building elements are determined in accordance with the methodology presented in SR 1907/1-1, 2, 3, taking into account at all times the corrected thermal resistance of the opaque and glazed surfaces.

The total area of the studied hall is 2,854.80 m², the total area of the exterior walls is 4,062.60 m², and the total area of glazed elements is 1,344.946 m², representing a glazing percentage of 33.10%, distributed as follows:

-exterior windows on metal frames, double-glazed with two glass panes spaced 2–4 cm apart: 532.190 m², representing a glazing percentage of 13.10%;

-Nevada glass 0.2 × 0.2 m, 7 cm thick: 73.20 m², representing a glazing percentage of 1.80%;

-skylights with frosted glass on metal frames, single-glass pane: 704.14 m², representing a glazing percentage of 17.33% [10].

The construction characteristics of the opaque and glazed elements are as follows [10]:

-Total usable height of the hall: 9.90 m;

-Exterior walls with an interior-measured height of 9.90 m and a total thickness of 30 cm, made of aerated concrete (BCA) type GBN-50, in three layers: two plaster layers, one interior made of lime mortar with $\delta_{,i} = 2$ cm and a thermal conductivity coefficient $\lambda_i = 0.70$ W/(m·K), and one exterior made of cement plaster with $\delta_{,e} = 3$ cm and a thermal conductivity coefficient $\lambda_e = 0.93$ W/(m·K), between which is the BCA layer with $\delta_{BCA} = 12.5$ cm and a thermal conductivity coefficient $\lambda_{BCA} = 0.27$ W/(m·K).

- Interior walls with an interior-measured height of 9.90 m and a total thickness of 20 cm, made of aerated concrete (BCA), in three layers: two plaster layers of lime mortar on the interior and exterior with $\delta_i = 2$ cm and a thermal conductivity coefficient $\lambda_i = 0.70$W/(m·K), between which is the BCA layer with $\delta_{BCA} = 16$ cm and a thermal conductivity coefficient $\lambda_{BCA} = 0.27$ W/(m·K).

Exterior windows type 1 is on metal frames and sashes, with double-glass panes spaced 2–4 cm apart, inward-opening, without special sealing;

- exterior windows type 2, made of frosted Nevada glass, in strips 0.60 m high at the level of the second floor, with a total length of 122.00 m, having a minimum corrected thermal resistance of 0.479 (m²·K)/W;

- exterior doors are metal (aluminum) with a total thickness δ_{UE} =4 cm, constructed from two aluminum sheets 3 mm thick, with a thermal conductivity coefficient λ_{Al} = 220 W/(m·K), between which is a PVC foam layer 3.4 cm thick, with a thermal conductivity coefficient λ_{Pol} = 0.05 W/(m·K).

- interior doors type 1 are metal doors made of aluminum with a total thickness δ_{UE} = 3 cm, constructed from two aluminum sheets 2 mm thick, with a thermal conductivity coefficient λ_{Al} = 220 W/(m·K), between which is a PVC foam layer 2.6 cm thick, with a thermal conductivity coefficient λ_{Pol} = 0.05 W/(m·K);

- interior doors type 2 are glued plywood doors with a total thickness δ_{UI} = 3.5 cm, with a thermal conductivity coefficient λ_{Pl} = 0.17 W/(m·K).

- interior doors type 3 are metal doors made of aluminum with a total thickness δ_{UE} = 3 cm, with glass covering 40% of the total door area, the glass having a thickness δ_{glass} = 6 mm and a thermal conductivity coefficient λ_{glass} = 0.75 W/(m·K).

The metal part, 60% of the total door area, is constructed from two aluminum sheets 2 mm thick with a thermal conductivity coefficient λ_{Al} = 220 W/(m·K), between which is a PVC foam layer 2.6 cm thick with a thermal conductivity coefficient λ_{Pol} = 0.05 W/(m·K);

- the floor has the following structure: reinforced concrete slab with a density of 2500 kg/m³ and a thickness δ_{RC} = 20 cm, with a thermal conductivity coefficient λ_{RC} = 1.74 W/(m·K), and plain aggregate concrete with a density of 1800 kg/m³ and a thickness δ_{AG} = 4 cm, with a thermal conductivity coefficient λ_{AG} = 0.81 W/(m·K).

- the ceiling at the upper part is a terrace type with glazed surface. The constructed part consists of: an interior plaster layer of lime mortar with δ_i = 2 cm and a thermal conductivity coefficient λ_i = 0.70 W/(m·K), a reinforced concrete slab with a density of 2500 kg/m³ and a thickness δ_{RC} = 20 cm, with a thermal conductivity coefficient λ_{RC} = 1.74 W/(m·K), and a bituminous waterproofing layer with a thickness δ_{hydro} = 0.8 mm and a thermal conductivity coefficient λ_{hydro} = 0.17 W/(m·K).

The glazed part of the terrace consists of fixed transparent glass panes, a single glass sheet, on a metal frame made of OL, with a minimum corrected thermal resistance of 0.17 (m²·K)/W.

The determination of heat losses through the building envelope elements, on the basis of which the thermal energy consumption is also calculated, is carried out taking into account the current standards, with the results presented in Tables II and III.

Considering that activities generating heat take place inside the hall, and knowing that the heat losses through the envelopes (machine casings) are approximately 2.5 kW, that the heat contribution from people working inside the hall (50 persons, at 0.174 kW/person) is approximately 8.7 kW, and that the solar gains are about 70 kW, the total heat gain for the studied hall amounts to 81.2 kW.

This means that the heat demand to be covered by the heating system is: (341.466 + 35.159) – (2.5 + 8.7 + 70) = 295.425 kW.

TABLE II.
HEAT LOSS THROUGH THE ANVELOPE OF THE INDUSTRIAL HALL BUILDING

Nr. crt.	Building element	A, [m²]	R`, [(m²·K)/W]	Δt, [°C]	Q_T, [kW]	Q_c, [kW]
1.	Exterior walls made of aerated concrete (BCA)	420,70	0,825	32	16,890	19,372
		65,52		33	2,713	3,013
2.	Exterior window	472,64	0,318	32	61,352	70,369
		59,55		33	7,415	8,233
3.	Nevada glass 0.2 × 0.2 m, 7 cm thick	73,20	0,479	32	5,868	6,731
4.	Exterior metal door	35,89	0,167	32	11,853	13,596
5.	Floor	2545,80	0,668	7	28,492	32,680
		309,00		8	3,700	4,109
6.	Interior wall	626,58	0,938	2	1,350	1,549
6.	Interior wall	228,12	0,938	1	0,255	0,284
		318,24		-1	-0,352	-0,404
		97,23		-3	-0,334	-0,383
7.	Interior metal doors	15,12	0,251	2	0,289	0,332
		11,97		1	0,057	0,064
		21,51		-1	-0,266	-0,305
		4,41		-3	-0,063	-0,073
8.	Interior glued plywood doors	3,36	0,485	2	0,033	0,038
9.	Interior metal doors with glass	3,78	0,255	1	0,018	0,020
				-1	-0,018	-0,020
10.	Terrace above the top floor	2150,66	0,781	32	88,19	101,073
11.	Frosted glass panels on metal frame	704,14	0,382	32	70,783	81,188
TOTAL Hall		-	-	-	298,177	341,466

TABLE III.
HEAT LOSSES DUE TO INFILTRATION THROUGH THE JOINTS OF EXTERIOR DOORS AND WINDOWS

Nr. crt.	Window type	Closure element composition	i, $\left[\frac{W\cdot s^{4/3}}{m^{5/3}\cdot{}^{\circ}C}\right]$	L, [m]	E	Q_u, [kW]	Q_i, [kW]
1.	Exterior window	Double-glazed with two glass panes spaced apart of 2..4 cm	0,0944	1209,60	1,12	6,064	35,159
		Total hall	-	1209,60	-	6,064	35,159

IV. RESULTS

The total heat demand to be considered in calculating the annual total heating load will take into account, for glazed elements, both the heat required to heat the infiltrated air and the heat losses through transmission.

Considering that activities in the industrial hall release pollutants in varying amounts, the air change rate results as $n_{ao} = 1$ m³/(h·m³) [11].

As a result, the heating load required for the hall is 552.56 kW.

During the study, the option of installing air heaters with a nominal power of 60 kW is analyzed, the number of air heaters required being:

$$N_{aerot} = \frac{Q_s}{Q_{n,aerot}} = \frac{552{,}56\ \text{kW}}{60\ \text{kW}} = 9\ \text{air heaters} \tag{1}$$

The implementation of such a decentralized heating system for an industrial consumer takes into account:

1. Certain technical specifications;
2. A financial analysis regarding investment and operation.

1. Technical installation specifications:

-nine 60 kW air heaters and one additional 15 kW air heater are selected, so that the total installed power of 555 kW provides a safety margin of 2 kW above the calculated demand, being ideal for peak conditions;

-installation height: 6.5–7.5 m (for H = 9.90 m);

-distance between air heaters: ≈ 20 m in both directions;

-inclination angle: 15–20° relative to horizontal;

-coverage area with warm air per heater / hall area: ≈ 330 m²

The distribution of these air heaters along the length of the hall is carried out according to Figure 4, providing a series of practical operational advantages, the most important of which are: uniform heat distribution throughout the hall; redundancy – if one air heater fails, the heating system remains functional; flexible control – the possibility of thermal zoning; energy efficiency – adequate power for the air volume

2. Investment and operating cost analysis:

- initial investment: approx. 660,000 lei (132,000 EUR)

- equipment: 9 electric air heaters of 60 kW: ≈ 540,000 lei, at an estimated price of ≈ 60,000 lei/unit (based on market price extrapolation), and 1 electric air heater of 15 kW ≈ 15,000 lei, resulting in a total equipment cost of 555,000 lei;

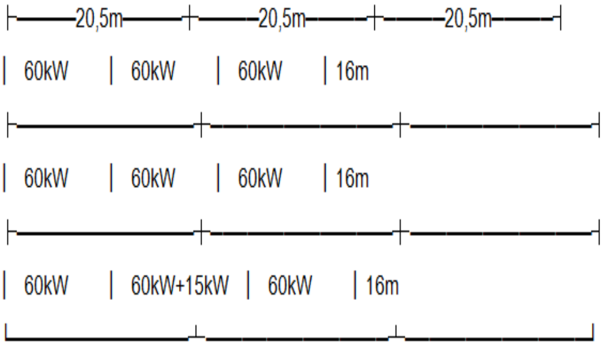

Fig. 4. Layout diagram of the 60 kW air heaters for the analyzed hall

- installation and accessories: installation, three-phase electrical wiring: ≈ 80,000 lei; control systems and thermostats: ≈ 15,000 lei; auxiliary works: ≈ 10,000 lei, resulting in a total installation and assembly cost of 105,000 lei;

- considering a useful service life of 15–20 years, this results in an annual depreciation of approximately 33,000–44,000 lei/year, i.e., a monthly depreciation of about 2,750–3,667 lei/month;

- hourly electricity consumption at maximum installed power is 555 kWh, leading to the following estimates of electricity costs for the equipment: at minimum price (1.03 lei/kWh): 571.65 lei/hour; at average price (1.25 lei/kWh): 693.75 lei/hour; at maximum price (1.55 lei/kWh): 860.25 lei/hour;

- considering a heating season duration of approximately 5 months (November–March), with an average hourly hot air distribution schedule for heating of 10 h/day, and low outside temperatures for 22 working days per month, the following seasonal cost values result for the three scenarios:

- Optimistic scenario: ≈ 628,815 lei/season;
- Realistic scenario: ≈ 763,125 lei/season;
- Pessimistic scenario: ≈ 946,275 lei/season.

V. CONCLUSIONS

In the conclusions section of the case study conducted in this work, certain aspects are analyzed on the one hand regarding the optimization of the investment and operation of the new heating system proposed for the industrial hall, and on the other hand, the technical and economic risks.

The optimization recommendations include:

-Energy contract: In this case, it is recommended to renegotiate the special industrial contract with the electricity supplier with whom the industrial consumer has an agreement, or to negotiate with another supplier, aiming for lower electricity prices;

-Intelligent control: Installation of hot air heating systems with thermostats programmed by hour;

-Additional insulation: Involving extra investment costs in thermal curtains to reduce losses (additional thermal insulation measures for the hall's envelope elements to minimize heat losses);

- Renewable energy: Evaluating the possibility of installing photovoltaic panels to reduce the cost of electricity purchased from the supplier;

-Investment profitability: Depending on energy prices and the procurement strategy.

Regarding risks, technical and economic risks were identified, for which corrective or preventive technical measures are proposed:

a) Technical risks:

-Electrical network overload: Medium probability (~30%), major impact – system shutdown; preventive measures: preliminary energy audit, upgrading the electrical network, if necessary, automatic load management system.

-Uneven heat distribution: High probability in the first month (~60%), minor impact – local discomfort; preventive measures: fine adjustment of deflectors, power adjustment by zones, installation of auxiliary fans.

-Failure of some air heaters: Low probability (5% per year), moderate impact – reduced performance; preventive measures: spare stock (1 air heater), service contract with response time <24h, continuous monitoring system.

b) Economic risks:

These relate to electricity price fluctuations, with two scenarios identified:

-Optimistic scenario: Electricity price decreases to 0.95 lei/kWh, resulting in approximately 17% reduction in electricity costs.

-Pessimistic scenario: Electricity price increases to 1.45 lei/kWh, resulting in approximately 26% increase in electricity costs.

Considering the above economic risks, an impact analysis over a 5-year period was performed, resulting in two possible scenarios:

-Optimistic: Financial savings of 612,000 lei;

-Pessimistic: Additional cost of 936,000 lei.

To mitigate the financial impact on the operational efficiency of the air heater system, the following hedging measures are considered:

1. Signing a fixed electricity supply contract with a supplier for a period of 3 to 5 years;
2. Making an additional investment in photovoltaic panels (350 kWp) to provide some energy independence for the industrial hall under analysis;
3. Implementing a thermal storage system for peak hours

ACKNOWLEDGMENT

Source of research funding in this article: Research program of the Electrical Engineering Department financed by the University of Craiova.

Contribution of authors:
First author – 50%
First coauthor – 30%
Second coauthor – 10%
Third coauthor – 10%

Received on September 24, 2025
Editorial Approval on December 5, 2025

REFERENCES

[1] M. Ilina, et al., *Enciclopedia tehnică de instalaţii. Manualul de Instalaţii – Încălzire* (in Romanian), 2nd ed, Association of Installation Engineers, Bucharest: Artecno, 2010.

[2] I. Mircea and R. C. Dinu, *Producerea energiei electrice şi termice,* (in Romanian), part II, Craiova: Universitaria, 2006.

[3] R.C. Dinu and C. Bratu, *Decentralized Energy Production Systems* (in Romanian), course, Craiova, 2025, https://classroom.google.com/w/NzE5OTMyMDgwNjAz/t/all

[4] R. C. Dinu, *Installations for Constructions* (in Romanian), course, Craiova,2025, https://classroom.google.com/w/NzQ4NjYwMDY4NDE1/t/all.

[5] J. Smith, *Modern Heating Systems and Efficiency*, Springer, 2019.

[6] I. Căldare, *Instalaţii de încălzire cu tuburi radiante de joasă temperatură a incintelor cu volum mare. Bazele fizice şi experimentale* (in Romanian), Bucharest: MatrixRom, 2009.

[7] R.. C., Dinu, Operation of heat supply systems in discontinuous mode (Funcționarea sistemelor de alimentare cu căldură în regim discontinue), Doctoral dissertation No. 2, Technical University of Construction, Faculty of Installations, Bucharest, 2003.

[8] M. Popescu, *Modern Heating Technologies* (*Tehnologii moderne de încălzire)*, Bucharest: Tehnica, 2020.

[9] ******* SR 1907-1 "Instalaţii de încălzire. Necesarul de căldură de calcul. Prescripţii de calcul" (in Romanian), ICS 91-140.20, Romanian Institute for Standardization, Bucharest, 1997.

[10] *** Heating Balance Electroargeş, 2011.

[11] R.C. Dinu and C. Bratu, *Aplicaţii în Energetică* (in Romanian), Bucharest: AGIR, 2023.